Arctic Tropospheric Aerosols Observed by Lidar during Winter Seasons at Eureka, Canada: Optical Properties and Source Regions of Aerosol layers

Arctic Tropospheric Aerosols Observed by Lidar during Winter Seasons at Eureka, Canada: Optical Properties and Source Regions of Aerosol layers

冬季カナダユーレカでライダーによって観測された北極対流圏エアロゾル：エアロゾル層の光学的特性と起源観点から

Division of Particles and Astrophysical Science
Graduate School of Science, Nagoya University

名古屋大学大学院 理学研究科 素粒子宇宙物理学専攻

Shoken Ishii

石井昌憲

報告番号	甲第 4859 号

論　文　目　録

報告番号	※　　第　　号	氏名	石井昌憲

主　論　文

題　目

Arctic Tropospheric Aerosols Observed by Lidar during Winter Seasons at Eureka, Canada: Optical Properties and Source Regions of Aerosol layers
(冬季カナダユーレカでライダーによって観測された北極対流圏エアロゾル：エアロゾル層の光学的特性と起源域の観点から)

副　論　文

題　目　　2冊

1. Arctic haze and clouds observed by lidar during four winter seasons of 1993 -1997, at Eureka, Canada.
(1993 年から 1997 年の冬季にカナダ・ユーレカにおいてライダーによって観測された北極ヘイズと雲)
S. Ishii, T. Shibata, T. Nagai, K. Mizutani, T. Itabe, M. Hirota, T. Fujimoto and O. Uchino
Atmos. Eviron., 33, 2459-2470 (1999)
2. The source, size and chemical composition of the winter arctic tropospheric aerosol layer observed by lidar at Eureka, Canada.
(カナダ・ユーレカにおいてライダーによって観測された冬季北極対流圏エアロゾル層のソースと粒径と化学成分に関して)
S. Ishii, T. Shibata, T. Sakai, M. Kido, K. Hara, K. Osada, Y. Iwasaka, T. Nagai, T. Fujimoto, T. Itabe, K. Mizutani and Uchino
J. Meteor. Soc. Japan., in press, (2001)

参考論文

題　目　　2冊

1. OBSERVATIONS OF PINATUBO VOLCANIC CLOUD BY CRL LIDARS AT WAKKANAI AND KOGANEI
(稚内と小金井における CRL ライダーによるピナツボ火山雲の観測)
T. Itabe, T. Shibata, S. Ishii, and K. Asai
J. Communi. Res. Laboratory, 39, 455 – 464 (1992).

2. Optical fiber coupled multi telescope lidar system: Application for a Rayleigh lidar
(光ファイバーによるマルチ望遠鏡ライダーシステム：レイリーライダーへの応用)
S. Ishii, T. Shibata, K. Mizutani and T. Itabe
Rev. Sci. Inst., 7, 3270–3273 (1996).

①

Arctic Tropospheric Aerosols Observed by Lidar during Winter Seasons at Eureka, Canada: Optical Properties and Source Regions of Aerosol layers

冬季カナダユーレカでライダーによって観測された北極対流圏エアロゾル
:エアロゾル層の光学的特性と起源域の観点から

Division of Particles and Astrophysical Science
Graduate School of Science, Nagoya University

名古屋大学大学院理学研究科素粒子宇宙物理学専攻

Shoken Ishii

石井　昌憲

Abstract

A Mie-scattering-polarization lidar system was installed at Eureka (80.0° N, 86.4° W), in the Canadian high arctic in the winter of 1992-93. We have made lidar observations of the arctic troposphere by using a Mie-scattering-polarized lidar system the winter seasons from 1993-94 to 1998-99. Since lidar observations were performed during polar night, it was difficult to confirm scattering objects with the naked eye and to quickly distinguish between arctic aerosol layers and clouds composed mainly of ice crystals or ice crystals blown up near the observatory. Therefore, it is necessary to have some other way of determining whether scattering objects we observed are arctic aerosol layers or clouds. Although it is difficult to classify arctic aerosol layers and clouds into two groups under the following conditions: (1) when arctic aerosol layers could co-exist with many clouds, and (2) when arctic aerosol layers could be present above thick clouds, statistically discriminations between arctic aerosol layers and clouds could be made using two methods. First the vertical profiles of arctic aerosol layers and clouds were compared with meteorological data obtained by a radiosonde, and the relations between the scattering and depolarization ratios and the meteorological data were investigated. Arctic aerosol layers existed in the dry atmosphere with less than approximately 60% humidity over ice (five-winter average: 43 ± 19%), while clouds existed in the humid atmosphere with greater than approximately 80% humidity over ice (five-winter average: 90 ± 15%). Then, the time dependency of the correlation coefficient between the different vertical profiles for arctic aerosol layers and clouds was investigated. The correlation between different vertical profiles of arctic aerosols was close: the correlation coefficients ranged from 0.8 to 1.0. On the other hand, the correlation between different vertical profiles of clouds was extremely changeable overt time: the correlation coefficients ranged from 0.0 to1.0.

We investigated the vertical distribution of and optical information about the arctic aerosol layers classified with using two methods. The arctic aerosol layers were observed at altitudes less than 3 km frequently and were observed occasionally at altitudes of 3 to 5 km. The five-winter average Mie backscattering coefficient and aerosol depolarization ratios of arctic aerosol layers observed by lidar were 5.3×10^{-7} m $^{-1}$ sr $^{-1}$ and 5.2%, respectively. The value of the Ångström exponent of arctic aerosol layers calculated from two-wavelength lidar observations ranged from 0.8 to 1.2.

We calculated isentropic backward trajectories in order to investigate the long-range transport and source regions of arctic aerosol layers we observed. Isentropic backward trajectories of arctic aerosols observed over Eureka at different altitudes suggested that the source regions of arctic aerosols were Eurasia, the northern Pacific and Atlantic

Oceans, the Arctic Ocean, and regions near the coast of the Arctic Ocean. To estimate the size of arctic aerosols we observed, we also calculated the lidar parameters (the backscattering coefficient, the aerosol depolarization ratio, and the Ångström exponent) by using the Mie theory, the calculated refractive indexes and the modeled particle size distribution. Those values calculated by using the Mie theory and the modeled particle size distribution suggested that, although the Mie backscattering coefficient was determined largely by the number concentration and the geometric mean diameter of the accumulation mode particles of diameter 0.2 μm to 0.3 μm, the aerosol depolarization ratio and Ångström exponent of the aerosols were influenced strongly by the number concentration and the geometric mean diameter of the coarse particles. The results of the isentropic backward trajectory calculations and the estimation of the size of arctic aerosols suggested that the possible chemical composition of the aerosols we observed was sulfate aerosol or sea salt.

To discuss the possible chemical compositions of arctic aerosols we assumed, daily sampling of aerosol particles was carried out in the late winter of 1998-99. We compared the variations in the chemical composition of aerosol particles collected at observatory with the vertical profile of aerosol particles observed by lidar. The high concentrations of Na^+ and Cl^- were obtained when clouds were observed by lidar and when fallen ice crystals and rime were found on the ground. The results of lidar observations and short-term aerosol sampling suggest that cloud was one of sources of arctic aerosols. The high concentrations of non-sea-salt SO_4^{2-}, NH_4^+, and H^+, or Na^+ and Cl^- were obtained when the stable aerosol layer was observed by lidar. The results supported the assumption that the aerosol layers observed over Eureka were composed of sulfate aerosol or sea salt.

Contents

1. Introduction

1.1 Polar region

The polar regions exhibit obvious symptoms of global climate change because of the convergent region of global circulation. Sea ice, snow cover, glaciers, tundra, permafrost, boreal forests, and northern peat-lands are all sensitive indicators of global climate change, and are susceptible to subtle variations in sunlight, surface temperature, ocean heat-transport, atmosphere-ocean interactions, and air pollution. As a result of global circulation, the symptoms of global climate change are engraved in those indicators. Aerosols play an important role in the global circulation (Logan et al., 1981; Prospero et al., 1983; Kley, 1997). The aerosols derive from sea spray, wind blown dust, marine biogenic activity and human activity. Because of the topography and geographical configuration of oceans and continents in the polar regions as show in Figure 1.1, the seasonal variations and concentrations of aerosols in the Arctic are considered to be different from those in the Antarctic.

Topographically, the Arctic except for Greenland is flatter than the Antarctic. Figure 1.1 shows that the Antarctic is covered by the Antarctic ice sheet at latitudes of 65° S to 90° S. The Antarctic is entirely surrounded by the Indian, Pacific and Atlantic Oceans and is remote from human activity. Figure 1.1 shows that the Arctic is covered by the Arctic Ocean and that the Arctic is surrounded by the Pacific and Atlantic Oceans and the populated and industrialized continents. Hence, it is considered that the Arctic is more affected by various aerosols than the Antarctic.

Anthropogenic air pollutant (e.g., non-sea-salt (nss-) SO_4^{2-}, heavy metal, acid gasses, NO_x) and natural aerosols (e.g., sea salts, soil dust, MSA) are transported to the Arctic over several thousands km in the troposphere. Because of very stable thermal stratification in the winter lower arctic troposphere (arctic inversion layer) and less than 10 mm H_2O per month of precipitation in the cold half of year from October to May, the residence time are much longer in winter than in summer. Furthermore, there is a strong seasonal variation in the poleward transport of aerosols. For the meteorological reasons, arctic aerosols (this paper will use arctic aerosol as a general term for arctic tropospheric aerosol) have strong variations generally characterized by a summer minimum and a winter maximum.

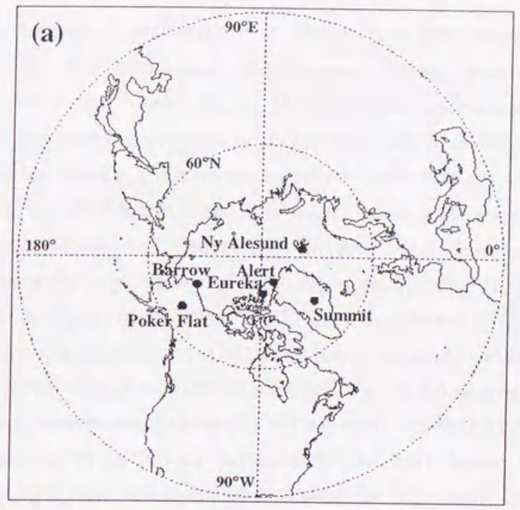

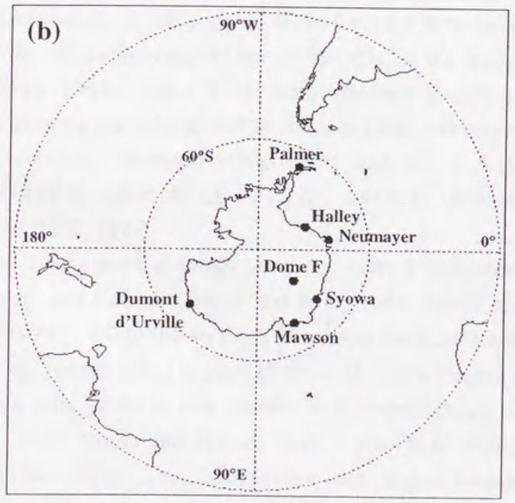

Figure 1.1 Polar Regions and locations of research stations. Observation site at Eureka shown in panel (a) was used for the lidar measurements described here (see, Figure 2.1)

1.2 Arctic aerosols

Anthropogenic aerosols is well known as Arctic Haze since the 1950s (Mitchell, 1956). Based on the qualitative observations during 'Partmigam' weather reconnaissance flights in the Alaska Arctic, Michel (1956) made several observations: (1) Arctic Haze is composed of particles no larger than 2μm diameter; (2) Arctic Haze is not composed of ice crystals; (3) it occurs in patches some 800 km – 1300 km across; (4) it has been observed at all levels in the atmosphere below 9 km above sea level (asl); and (5) it is seldom found over Greenland. In the 1960s, these observations lay dormant, until expectedly high values of total atmospheric turbidity, measured in the Alaskan Arctic during spring of 1971 and 1972 (Shaw and Wendler, 1972), prompted a renewed interest in the nature and origin of Arctic Haze. A study of the vertical profile of turbidity found layers of high turbidity at altitudes of a few kilometers asl (Holmgren, 1974). An airborne measurement campaign during April and May 1976 indicated that although particulate matter in the air between distinct haze layers was due to air pollution, the haze layer were composed of dust aerosols, originating presumably form Asian deserts (Rahn et al., 1977). This study was misinterpreted to mean that Arctic Haze was composed mainly of wind-blown dusts until the first routine ground-level measurements of the chemical composition of aerosols in the winter of 1976-1977 (Rahn and McCaffrey, 1980). Since 1981, many scientific groups have investigated the characteristics of arctic aerosols related to anthropogenic and natural aerosols, such as their seasonal variation, chemical composition, and size distribution (see, e.g. AGASP, 1984; AGASP II, 1989; ABLE 3A, 1992; DGASP, 1993; PSE 1992, 1994; IAOE-91, 1996; ARCTOC, 1997).

The characteristics of natural aerosols have also been investigated. Wind blown dusts peaks in spring and autumn (Barrie and Hoff, 1985; Barrie and Barrie, 1990; Sirois and Barrie, 1999). Wind blown dusts is transported from local source regions during high winds and remote desert sources (Rahn et al., 1977, Pacyna and Ottar, 1989; Welch, 1991). Sea salts peaks in late autumn and winter (Barrie and Hoff, 1985; Barrie and Barrie, 1990; Sirois and Barrie, 1999). The peak results in the longer residence time in the winter arctic atmosphere and higher frequency of storms generating sea salt in the northern oceans during winter (Erikson et al., 1986). Sea salts play a key role in the heterogeneous formation of nitrates as a sink of reactive nitrogen oxide in the winter arctic atmosphere (Hara et al., 1999). The halogens deriving mainly from marine sources play an important role in the lower tropospheric ozone depletion at polar sunrise (PSE 1992, 1994; ARCTOC, 1997).

In the winter Arctic, because photochemistry is absent and reactions that require

activation energy slow down and the residence time are much longer, the abundance of photochemically-reactive compounds and aerosol is loaded in the arctic troposphere (0 - ~ 8 km asl) polar sunrise. The Arctic plays an important role in the reactive field of arctic chemical cycles. Aerosols also play an important role in the radiation budget in the atmosphere through their spatial distributions and optical properties and the cloud-aerosols interactions. Many scientists have made observations to get more information about them. However, our knowledge of the vertical, horizontal and temporal distributions and optical properties of aerosols in the arctic troposphere is not enough to discuss the radiation budget. Therefore, as shown in Figure 1.2, the presence of various gaseous and particulate aerosols results in changes in the radiation budget the radiation budget, the arctic chemical cycles, the arctic ecosystem and the global climate change.

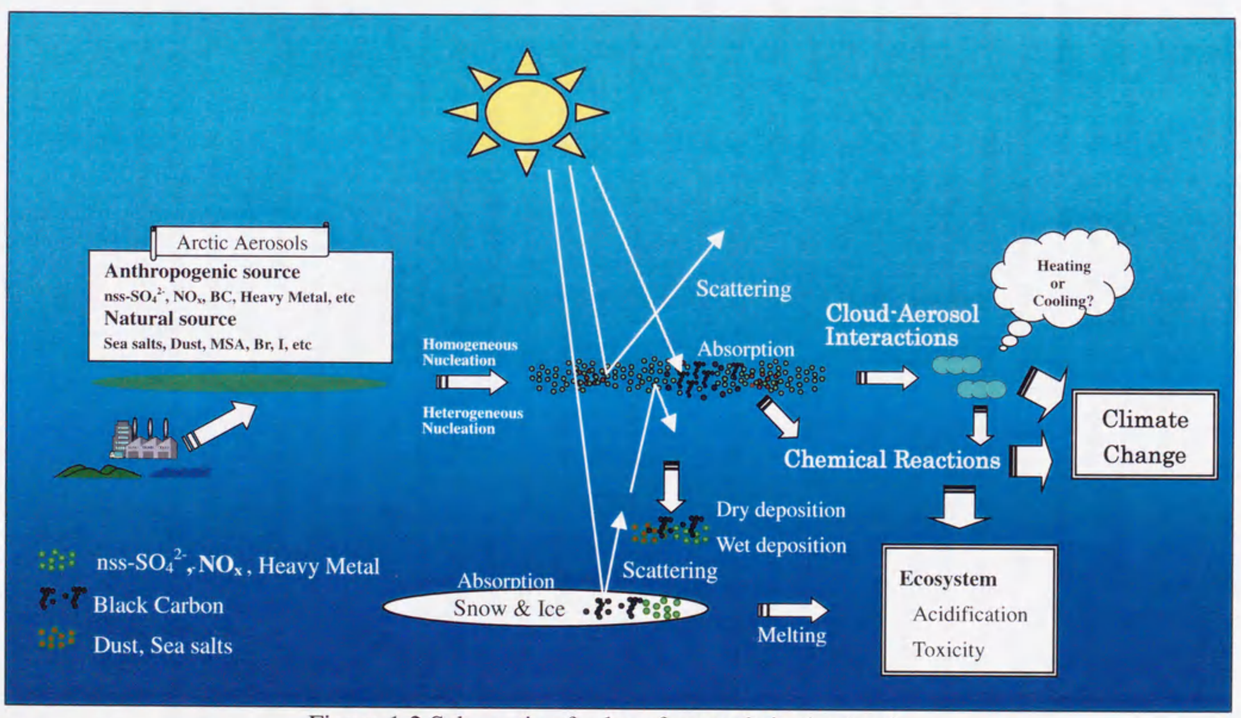

Figure 1.2 Schematic of roles of aerosols in the Arctic.

1.3 Objectives

In order to understand the processes by which arctic aerosols are incorporated into the arctic radiation budget, the arctic chemical cycle and the arctic climate processes, it is very important to know the spatial distributions, the optical properties, the size and the chemical composition of arctic aerosols. Although there were several airborne measurements and short-term lidar observations (e.g. Wendling et al., 1985; Hoff, 1987; Leaith et al., 1989; Radke et al., 1989; Khattaov et al., 1997), the characteristics of arctic aerosols have been investigated largely by making ground-level measurements. In 1992-93 winter season, we installed a Mie-scattering polarization lidar system with relatively high vertical and temporal resolution at Eureka (80.0° N, 86.4° W) in the Canadian high arctic. We used the Mie-scattering polarization lidar system and made long-term tropospheric observations at Eureka during the six winter seasons from 1993-94 to 1998-99.

The purpose of this study is to investigate the vertical distribution and the physical and chemical characteristics of arctic aerosols on the basis of lidar measurements in the arctic troposphere over Eureka. Firstly, in this study, we discuss a statistically significant discrimination between arctic aerosols and other scattering objects. We classify scattering objects into two groups. The vertical distribution of and optical information about the arctic aerosols are investigated statistically. Then, we calculate isentropic backward trajectories to discuss the long-range transport and source regions of the arctic aerosols observed by our lidar. To estimate the size of the arctic aerosols, we calculated the Mie backscattering coefficient, the aerosol depolarization ratio, and the Ångström exponent by using the Mie theory and the modeled particle size distribution. We infer the possible chemical compositions of the aerosols observed by lidar from the results of the isentropic backward trajectories and the estimated size of arctic aerosols. And then, to discuss the possible chemical compositions of the aerosols we inferred, we compared the variations in the chemical composition of aerosol particles collected at observatory with the vertical profile of aerosol particles observed by lidar. The aerosol characteristics discussed in this study will provide information useful in modeling the radiation budget, the atmosphere-surface interactions, and the cycle of aerosol chemistry in the arctic.

2. Observations and Measurements

2.1 Observation Site

A Mie-scattering-polarization lidar system we used is at the Arctic Stratospheric Ozone observatory (AStrO) 15 km northwest of the Canadian Weather Station Eureka (80.0° N, 86.4° W) in 1993. The lidar system has been used to obtain the vertical distribution of and optical information about arctic aerosols during the winter seasons. Figure 2.1 shows the location map for Eureka. Eureka is located near the tip of the Fohsheim Peninsula of Ellesmere Island. Eureka is covered by snow and is surrounded by the frozen sea during the winter seasons. AStrO is on the top of a hill whose elevation is about 600 m above sea level (asl). Although there are no mountains that block the airflow near AStrO, Eureka is surrounded by many mountains whose elevations are greater than 2000 m asl: those in the British Empire range northeast of Eureka (① in Figure 2.1), the Agassiz Ice Cap east of Eureka (② in Figure 2.1), and the mountains in the Princess Margaret range west of Eureka (③ in Figure 2.1).

The troposphere is roughly divided into two layers, the boundary layer and the free troposphere. During the winter season, the arctic boundary layer corresponds to an intense temperature inversion layer (Figure 2.2(a)). The top of the arctic inversion layer ranges from 1200 to 1500 m asl (Bradley et al., 1992; Sherreze et al., 1992; Hopper and Hart, 1994), but as shown in Figure 2.2(a) the top of the arctic inversion layer extends up to 2000 m (Raatz, 1991). AStrO, at 600 m asl, is always located in the arctic inversion layer during the winter season. Figure 2.2(b) shows that changes in the potential temperature raised are seen, suggesting that there are vertical movements through the exchanges of an air mass or storm activities in the winter arctic troposphere.

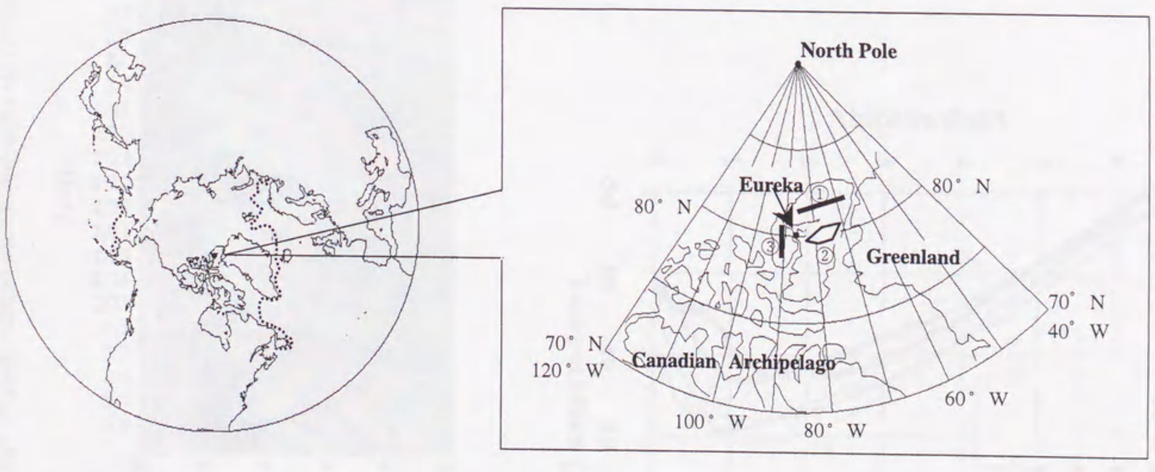

Figure 2.1 Location map for the vicinity of Eureka and Ellesmere Island (dashed line shows the boundary of the open water in March (Parkinson, 1991)

(a)

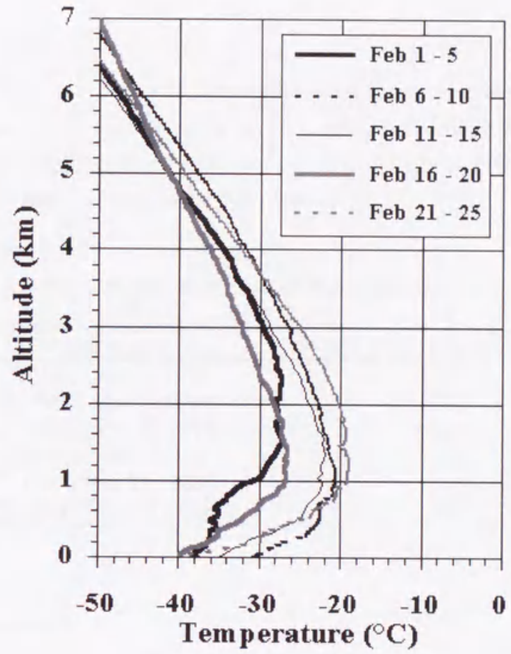

(b)

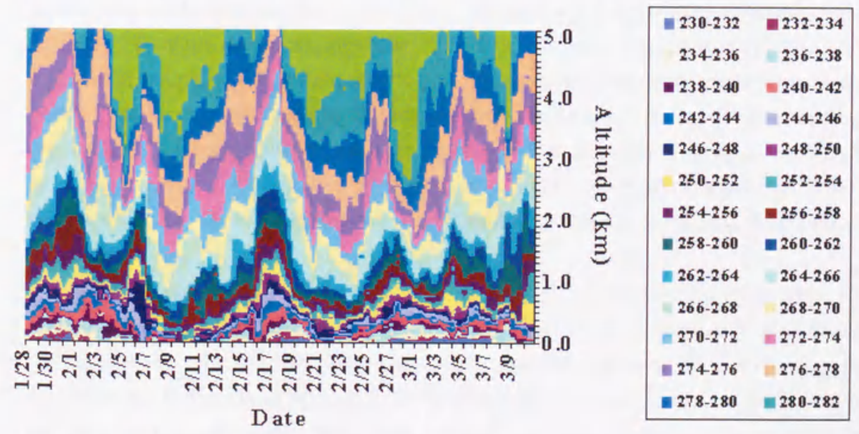

Figure2.2 (a) Five-day-average temperature profiles observed by a radiosonde launched at the Eureka weather station every 12 hour during February 1999 and (b) temporal variation of potential temperature during January 28, 1999 - March 10, 1999.

2.2 Observation Term

The observation term and total observation time for each winter are listed in Table 2.1. Observations were made as long as the weather conditions were permitted. The total observation time was about 440 hours in 1993-94, about 1190 hours in 1997-98, and was 600-800 hours in each of the other winters.

Table 2.1 Observation term and the total of observation time for 6 winter seasons

Observation term	The total of observation time (hours)
Dec 5, 1993- Mar 1, 1994	441
Dec 12, 1994- Mar 19, 1995	700
Dec 2, 1995- Feb 15 , 1996	618
Nov 29, 1996- Feb 27, 1997	703
Dec 7, 1997- Mar 31 , 1998	1186
Dec 23, 1998- Mar 11 , 1999	853

2.3 Lidar measurement

The laser radar called *lidar* (standing for LIght Detection And Ranging) has developed as one of light-remote sensing techniques to study atmospheric compositions, atmospheric molecules, aerosols and so on. The history of light-remote sensing began in 1951. To study the upper atmospheric density or transitivity, Elterman (1951) used a powerful searchlight as a light source and discussed the seasonal variations with the vertical profile of temperature at altitudes of 0-60 km drawn from light-remote sensing observations. There, however, were some problems in the case of using a searchlight as a light source. A laser has been used as a light source since Mainman (1961) developed Ruby Laser (standing for Light Amplification by Simulated Emission of Radiation).

Lasers are either *continuous wave* (CW) or *pulsed*. Pulsed laser can be ideal for lidar techniques if that radiant output forms a well-collimated beam that is to being monochromatic and of very short duration. The development of Q-switching by McClung and Hellwarth (1962) made possible the generation of a single, short-duration and high-energy pulse. The laser with using Q-switching method has contributed to the development of lidar techniques. The various lidar techniques, such as Raman lidar, coherent and incoherent Doppler lidar, differential absorption lidar (DIAL), have been invented by the development of Electro devices or computing techniques as well

as laser devices since then.

In addition to new techniques, for over about 30 years, lidar observations with using polarization measurement have been performed to study the structure and shapes of clouds, haze, and aerosols (*e.g.* Pal and Carswell, 1973; Iwasaka, 1981, 1986a, 1986b; Kobayashi, 1985, 1987; Sassen et al., 1990; Sassen, 1997; Shibata et al., 1997). If the 100 % linearly polarized laser beam is scattered by a spherical particle or a collection of spherical particles, scattering by those particles does not decrease the degree of polarization of the scattered light. If, on the other hand, the laser beam is scattered by a nonspherical particle or a collection of nonspherical particles, the degree of polarization of the scattered light is less than 100 %. Scattering by those particles results in *depolarization* of the laser scattered beam (Bohren and Huffman, 1983). In lidar observations with using polarization measurement, the depolarization ratio instead of the degree of polarization of the scattered light is often introduced to discuss the structure and the shapes of the scattering objects and provides information regarding the difference in shape from spherical particles. If the laser beam is completely linearly polarized, the depolarization ratio of the light scattered by spherical particles will be 0 %.

A schematic diagram of a Nd:YAG laser based Mie-scattering-polarization lidar system installed at AStrO is shown in Figure 2.3. The specifications of this lidar system are listed in Table 2.2. This lidar system uses the 2nd harmonics wavelength (0.532 μm) of the pulsed laser beam. The repetition rate of the laser is 10 pulses per second and its output energy is 400mJ/pulse (Continuum: PL8000). The divergence of laser beam collimated by a beam expander is less than 0.2 mrad.

The laser beam is transmitted vertically. The light backscattered by Rayleigh and Mie scattering particles is focused by a Schmidt-Cassegrain telescope (CELESTRON: CM11) whose the clear aperture is 11 inches. Five different neutral-density filters ND are set to adjust the intensity of the backscattered light at the focus point of the telescope. The backscattered light is collimated by a lens and passes through an interference filter with a 1 nm full width at half-maximum and a cubic polarization beam splitter PBS to measure the signal components parallel and perpendicular to the polarization plane of the laser beam. The parallel and perpendicular components of the backscattered light are focused onto two photomultiplier tubes PMT (Hamamatsu Photonics K.K.: H957) by a lens and converted to electrical analog signals by photoelectric effect.

The analog signals from each PMT are accumulated 500 times in a digital oscilloscope OSC (LeCroy: 9400) and converted to a digital format with using 8-bit

A/D converters installed in the oscilloscope. The converted data are then transferred to the host computer PC (NEC: 9801NS) via GPIB (General Purpose Interface Bus: IEEE-488 bus). Finally the data for each 15m height are stored in the host computer.

Table 2.2 Specifications of Lidar system

Transmitter	
Laser	Nd:YAG
Wavelength	0.532 μm
Pulse energy	400 mJ
Pulse repetition	10 Hz
Beam divergence	0.2 mrad
Receiver	
Telescope diameter	11 inch (254 mm)
Telescope type	Schmidt-Cassegrain type
Field of view	2 mrad
IF-Filter:	
FWHM	1nm
Transmission	50%
Detector	H957-01(Hamatsu)×2 (for polarization measurement)
Data Processing	
Signal Processing	A/D
Digitization:	
Digital Oscilloscope	LeCroy 9400
Sample interval	100nsec
Resolution	8bit
Data Recording	PC

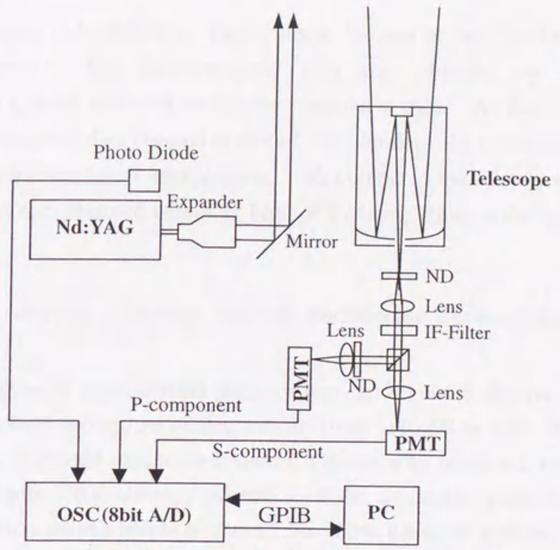

Figure2.3 Schematic diagram of lidar sysrem

2.4 Meteorological Data

A radiosonde is launched by Environment Canada at the Eureka weather station every 12 hour. The meteorological data was obtained by the radiosonde. Environment Canada provided us the meteorological data. As the vertical resolution of the meteorological data is equal to that of the lidar data, the meteorological data were calculated with using linear interpolation. We compared the calculated meteorological data with lidar data obtained within ±1 hour of the launch time of the radiosonde.

2.5 Aerosol sampling: Scanning Electron Microscopic examinations and Chemical Analysis

Daily sampling of arctic aerosol particles was carried out to observe the shape of the particles at AStrO during two winter seasons from 1997-98 to 1998-99. The aerosol particles were collected on carbon-coated Cu-plates with using a 2-stage low volume impactor. Figure 2.4(a) shows a schematic of the air intake system for the impactor. The impactor was set at a height of about 1.5m above the snow-surface. Air was taken in by an air pump placed outside AStrO. Aerodynamic 50% cut-off diameters of the impactor were 0.2 μm and 2.3 μm at an air flow-rated of 1.4 L min^{-1} for 10min. After aerosol sampling, those Cu-plates were kept in the polyethylene vials with an airtight cap in order to prevent contamination until Scanning Electron Microscopic (SEM) examinations. Sample vials were packed in a polyethylene bag. Those were transported to the Solar-Terrestrial Environment Laboratory (STEL), Nagoya University.

To investigate the chemical compositions of the aerosols, daily sampling of aerosol particles was carried out at AStrO during 1 February 1999 to 9 March 9 1999. Air was taken in about 1 m above the snow surface at a flow rate of 14 *l* min^{-1} at standard temperature (0 °C) and pressure (1013 hPa) (STP) for 23 hours. Aerosol particles were collected on a teflon membrane filter with a pore size of 1.0 μm (Advantech Toyo Co: J100A047A). After aerosol sampling, the filter was replaced with a new filter and stored in a pre-cleaned 15-m*l* polypropylene vial (Iwaki) with an airtight cap. The sample vials were packed in polyethylene bags and transported to STEL, Nagoya University. They were kept in a freezer until they were analyzed. To estimate contamination levels of ionic species until chemical analysis, the procedural blank samples were carried out with the same procedure for actual sampling without the passage of air. For extraction of water-soluble constituents in the aerosol particles, 14 m*l* of ultra pure water (18MΩ, Milli-Q water) was added to each vial in order to

dissolve the water-soluble constituents of the aerosols. Concentrations of water-soluble constituents of the arctic aerosol were measured by an ion chromatograph (Dionex: DX-300) equipped with AS11A analytical and AG11 guard columns for anion separation, CS23 analytical and CG12 guard columns for cation separation. An automated sample injector was used for simultaneous analysis of anions and cations in the sample water. Using a 500 μl injection loop for each analytical flow system, procedural blank concentration level of the polycarbonate and teflon filters used in the field were below or comparable to detection limits for some of ionic species under the present analytical conditions: 0.1 to 0.2 nmol m^{-3} for anions and cations. The concentrations of F^-, CH_3COO^-, $HCOO^-$, Cl^-, NO_2^-, NO_3^-, SO_4^{2-}, Ca^{2+}, Mg^{2+}, Na^+, and NH_4^+ were measured by the ion chromatograph. The concentration of H^+ was calculated from pH measurements (Beckman: ϕ34pH meter). The ionic concentrations were calculated by subtracting the maximum blank contamination levels. The major ions were Na^+, Cl^-, H^+, NH_4^+, and SO_4^{2-}.

(a)

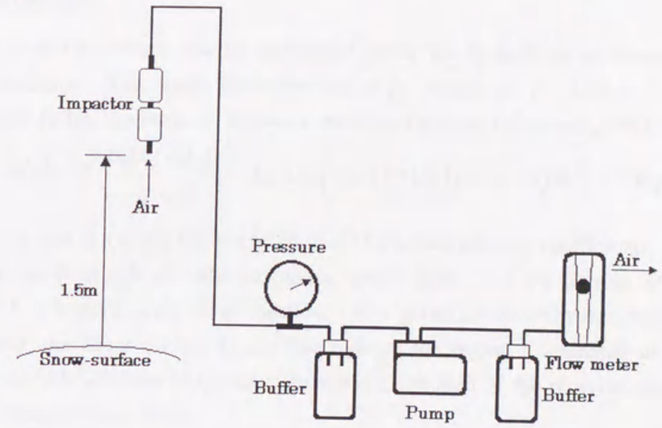

(b)

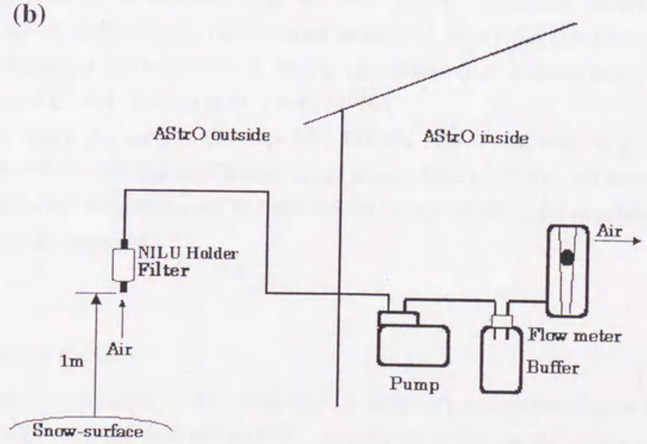

Figure 2.4 Schematic of the air intake system for (a) the 2-stage impactor and (b) the teflon filter.

3. Data Analysis

3.1 Lidar Equation

Lidar observations are usually performed under the hypothesis of monochromatic single scattering. The signal N(z) detected at an altitude of z - Δz/2 to z + Δz/2 is given by the following formula, known as the lidar equation (Measures, 1992):

$$N(z) = K \cdot \frac{\beta_R(z) + \beta_M(z)}{(z - z_0)^2} \cdot \Delta z \cdot \exp\left(-2 \cdot \int_{z_0}^{z_{wp}} (\sigma_R(z) + \sigma_M(z)) dz\right), \qquad \text{Equation 3-1}$$

where $\beta_R(z)$ and $\beta_M(z)$ are the Rayleigh and Mie backscattering coefficients, $\sigma_R(z)$ and $\sigma_M(z)$ are the Rayleigh and Mie extinction coefficients, z_0 is the altitude of the lidar system. K is known as the lidar constant. K is given by several parameters, such as laser output, the beam-overlap factor (the ratio of the region illuminated by the laser beam to the field of view of the receiver optics), the area of the receiver, the detector quantum efficiency and so on.

There are two unknown values $\beta_M(z)$ and $\sigma_M(z)$ for only one equation. To solve the lidar equation, it is assumed that the ratio of the extinction coefficient to the backscattering coefficient is constant with an altitude, $\sigma_M(z) / \beta_M(z)$ = Constant. Under the assumption, it can be solved by several procedures (*e.g.*, Russell et al., 1979; Klett, 1981; Fernald, 1984; Shibata et al., 1980, 1996a).

In this study, the method developed by Fernald (1984) was used to solve Equation 3-1. The backscattering coefficients in the troposphere (1-12 km asl) were calculated. The coefficients were then used to calculate the scattering ratio, the depolarization ratio, and Ångström exponent.

3.2 Scattering Ratio

To discuss an amount of Mie particles, it is necessary to separate signals scattered by Mie particles from the detected signals. In lidar observations, the scattering ratio R is often introduced for the purpose. The scattering ratio is defined as

$$R = 1 + \frac{\beta_M}{\beta_R} = 1 + \frac{\beta_{M,//} + \beta_{M,\perp}}{\beta_{R,//} + \beta_{R,\perp}}, \qquad \text{Equation 3-2}$$

where β_R and β_M are the Rayleigh and Mie backscattering coefficients and where $\beta_{i,//}$ and $\beta_{i,\perp}$ (i= R, M) are their components parallel and perpendicular to the polarization plane of the laser beam. The scattering ratio physically means the mixing ratio of the Mie particles to atmospheric molecules.

The scattering ratio was calculated as the following procedures. First the scattering ratio R_{Strat} from the stratospheric lidar observations (10-30 km asl) was calculated in order to acquire the minimum scattering ratio $R_{Tro,\ min}$ at a given altitude in the upper troposphere. Then the scattering ratio R_{Tro} from the tropospheric lidar observations (1.6-12 km asl) was calculated with using $R_{Trop,\ min}$.

The stratospheric lidar observations were made with using lidar system with a wavelength of 1.064 μm (λ_1) and 0.532 μm (λ_2) installed at AStrO to observe polar stratospheric clouds and aerosols. We first calculated $R_{Strat,\ \lambda 2}$ and $\beta_{Strat,\ \lambda 2}$ for the stratosphere (10-30 km) by assuming that there are no aerosols at altitudes of 30 to 35 km (Nagai et al., 1997) and using the normalizing method (*e.g.*, Russell et al., 1979; Shibata et al., 1980, 1996a). In the case of the observations of the troposphere with a lidar, it is difficult to assume an altitude where tropospheric aerosols are not present because of the existence of background tropospheric aerosols (Rosen, 1997). For the normalization of the tropospheric lidar, the averaged scattering ratio observed by the stratospheric lidar in the upper troposphere was given as the minimum scattering ratio $R_{Trop,\ min}$. $R_{Trop,\ min}$ was in the range of 1.05 to 1.10 at 0.532 μm obtained by the stratospheric lidar at an altitude of near 10 km asl. Using $R_{Trop,min}$ and the methods developed by Fernald (1984), we calculated the backscattering coefficients for all altitudes. These coefficients were then used to calculate the scattering ratio R_{Trop}. The scattering ratio profiles were calculated for altitudes greater than about 1.6 km asl, where the beam-overlap factor (the ratio of the region illuminated by the laser beam to the field of view of the receiver optics) is 1.0.

3.3 Depolarization Ratio

It is difficult to interpret the physical meanings directly from the depolarization ratio, since spherical and nonspherical particles with very different number concentrations co-exist in mixed phased or inhomogeneous scattering objects and the depolarization ratio is given as a ratio of optical quantities scattered by spherical and nonspherical particles. The depolarization ratio, however, is widely used in lidar observations (e.g., Iwasaka and Hayashida, 1981; Iwasaka 1986a; Sassen et al, 1990, Sassen 1997).

After correction of the system depolarization ratio with the procedure described by Adachi et al. (1998), the depolarization ratio can be defined in two different ways, depending on whether the Rayleigh scattering particles is included or not. The total (aerosol + Rayleigh scattering particles) depolarization ration δ is defined as

$$\delta = \frac{N_{\perp}(z)}{N_{//}(z) + N_{\perp}(z)} \times 100 = \frac{\beta_{R,\perp}(z) + \beta_{M,\perp}(z)}{\beta_{R,//}(z) + \beta_{M,//}(z) + \beta_{R,\perp}(z) + \beta_{M,\perp}(z)} \times 100\ [\%]\ ,\ \text{Equation 3-3}$$

In other experiments (e.g. Sassen 1991, Del Gausta et al., 1998), the total depolarization ratio is simply defined as the ratio of the components: $\delta = N_{\perp}(z) / N_{//}(z) = (\beta_{R,\perp}+\beta_{M,\perp}) /(\beta_{R,//}+\beta_{M,//})$. If nonspherical aerosols are not present, the Rayleigh scattering causes the depolarization. The depolarization ratio δ_m is assumed to be constant at 0.5%. This value was estimated by taking into account the full width at half maximum of the interference filter that was used (Young et al., 1980; Adachi, 1996). If the depolarization ratio calculated from the obtained data is larger than 0.5%, then nonspherical or solid particles are assumed to be present.

Since the aerosol depolarization ratio does not take into account the Rayleigh component, it is preferable to use the ratio when comparing with theoretical models based on the Mie scattering theory or discussing the lidar observations under the low scattering ratio (Iwasaka, 1986b). The aerosol depolarization ratio δ_a is defined as

$$\delta_a = \frac{\beta_{M,\perp}(z)}{\beta_{M,//}(z) + \beta_{M,\perp}(z)} \times 100 = \frac{\delta(z) \cdot R(z) - \delta_m}{R(z) - 1}\ [\%]\ ,\quad \text{Equation 3-4}$$

where δ_m is the Rayleigh depolarization ratio at the wavelength of the laser beam and the bandwidth of lidar system (δ_m = 0.5 % for the interference filter of FWHM =1nm used in this study). The δ_a for spherical particles is 0% for spherical particles and for nonspherical particles deviates from 0%. If the aerosol depolarization ratio is larger than 0%, then nonspherical or solid particles are assumed to be present.

The profile of total depolarization ratio was calculated for altitudes greater than about 1.0 km above sea level. This lowest altitude for the depolarization ratio is lower than that for the scattering ratio, because the beam-overlap factor is canceled in Equation 3-3. The altitude was determined by the dynamic range of a photomultiplier tube. The intensity of the signals received from altitudes of lower than about 1km asl was out of the dynamic range. The lowest altitude for the aerosol depolarization ratio is an altitude of about 1.6 km above sea level because of the function of the scattering ratio.

3.4 Ångström exponent

The Ångström exponent α is an index of the size distribution of Mie scattering particles. The backscattering coefficient of particles is proportional to $\lambda^{-\alpha}$ (Ångström, 1964). In general, larger values of α suggest that the number of smaller-sized aerosols

is large and vice versa. We calculated α from two-wavelength lidar observations by using the formula as

$$\alpha = -\frac{\log_{10}(\beta_{M,\lambda 1}/\beta_{M,\lambda 2})}{\log_{10}(\lambda_1/\lambda_2)}, \qquad \text{Equation 3-5}$$

where $\beta_{M,\lambda 1}$ and $\beta_{M,\lambda 2}$ are the Mie backscattering coefficients at the wavelengths of λ_1 and λ_2, respectively. $\beta_{M,\lambda 1}$ for the troposphere and stratosphere (1 - 25 km) was calculated by using $\beta_{Strat,\lambda 1}$ given in Section 3.2 assuming that the value of α for arctic background aerosols in the upper troposphere and lower stratosphere is about 1.4 (Shibata et al., 1997). Finally α were calculated by substituting $\beta_{M,\lambda 1}$ and $\beta_{Trop,\lambda 2}$ into Equation 3-5.

3.5 Relative humidity over ice

The relative humidity over ice $RH_{over\ ice}$ is calculated from a radiosonde data using the following equations given by the Goff-Gratch (1946) formulation:

$$\log_{10} e_{S,water}(T) = 10.79586 \cdot \left(1 - \frac{T_1}{T}\right) - 5.028001 \cdot \log_{10}\left(1 - \frac{T_1}{T}\right) + 1.50475 \times 10^{-4} \times \left\{1 - 10^{-8.2969 \times \left(\frac{T}{T_1} - 1\right)}\right\} + 0.42873 \times 10^{-3} \times \left\{10^{4.76955 \times \left(1 - \frac{T_1}{T}\right)} - 1\right\} + 0.7861, \qquad \text{Equation 3-6}$$

$$\log_{10} e_{S,ice}(T) = -9.09685 \cdot \left(\frac{T_1}{T} - 1\right) - 3.566541 \cdot \log_{10}\left(\frac{T_1}{T}\right) + 0.876793 \times \left\{1 - \frac{T_1}{T}\right\} + \cdot \log_{10}(6.1071)) \qquad \text{Equation 3-7}$$

$$R.H._{over\ ice} = \frac{e_{S,water}}{e_{S,ice}} \times RH, \qquad \text{Equation 3-8}$$

where $e_{S,\ water}$ (hPa)and $e_{S,\ ice}$ (hPa) are the saturation vapor pressure over plane surfaces of pure water and pure ice, T is temperature at an altitude of z km above sea level, R.H. is the relative humidity over water observed by radiosonde at an altitude of z km above sea level, and T_1 is the ice-point temperature (273.16K).

3.6 Atmospheric trajectory

Various atmospheric trajectories have been applied as a useful tool for atmospheric

transport problems. The trajectories, however, differ depending on whether there is vertical wind information. If the vertical wind velocity is known, then numerical integration of the Lagrangian displacement equation is straightforward. The lack of information about vertical velocities in meteorological data is a persistent problem which can be circumvented by making use of conservation laws. If the vertical wind velocity is unknown, information about vertical motion may be inferred from the conservation of potential temperature.

If the time scale of flow into or out of the system is slow compared to the dynamical time scales of interests, the potential temperature is a conserved quantity. Since potential temperature is a direct measure of the entropy, trajectory that conserves potential temperature is known as isentropic trajectory. Although an advantage of isobaric trajectory is that the wind field is defined by grid data at mandatory pressure surfaces provided by meteorological data, the assumption of isobaric air mass motion is unrealistic for long-range transport. Under typical atmospheric conditions, the vertical profiles of temperature and pressure give rise to a monotonic increase of potential temperature with altitude, the potential temperature can be viewed as an independent vertical coordinate. Isentropic trajectory is constrained to move on a constant potential temperature surface and the vertical motion of an air mass is due to entirely to the time-dependent topography of this surface. The conservation of potential temperature can be simply implemented in a numerical scheme by interpolating the grid wind field onto an isentropic surface computed from input temperature and pressure field. As described by Danielsen (1961), isentropic trajectory represents the actual airmass motion more realistically than isobaric trajectory.

To investigate the long-range transport and source region of arctic aerosols observed over Eureka in the troposphere, ten-day isentropic backward trajectories of them were calculated by using isentropic trajectory model developed by Sakai, STEL, Nagoya University (2000). The lower limit of the calculation (2000 m asl) was chosen in consideration of the elevation of surrounding mountains and the top of the Arctic inversion layer. Isentropic backward trajectories were calculated using the date, time, and altitudes of arctic aerosols observed by the lidar and the objective analysis data of the Japan Meteorological Agency. The isentropic backward trajectory calculation was stopped under the following conditions: when the altitude corresponding to the potential temperature is lower than that of the land- or sea-surface, or when an airmass is under the unstable stratification.

Although isentropic backward trajectory calculations are useful in investigating the long-range transport of an air mass, there is an uncertainty because the meteorological

data is limited. The horizontal uncertainty of isentropic trajectories cannot be calculated accurately, but Kahl et al. (1989) compared a limited set of arctic trajectories calculated using three different models. They estimated the uncertainty of an isentropic trajectory after five days to be in the range of 800 km to 1000 km. Five-day back trajectories, however, are not long enough to discuss possible distant source regions of arctic aerosols (Harris and Kahl, 1994). In this study we calculated ten-day isentropic back trajectories. Considering the trajectory uncertainty due to the limited meteorological data, we calculated twenty-five trajectories with independently changing the initial coordinate of the calculation by 0.5° (latitude direction) × 2.5° (longitude direction) grid interval surrounding AStrO as Kahl (1993) had suggested. Kahl et al. (1989) suggested that the outer boundaries defined by the ensemble calculation should serve to identify the range of possible source regions as well as to determine whether the trajectories encounter deformation areas where widely divergent solutions are possible. We confirmed whether the trajectories encounter deformation areas where widely divergent solutions are possible by following their suggestions.

4. Results and Discussions

4.1 The discrimination between arctic aerosols and clouds

4.1.1 The vertical profile of scattering objects observed by lidar

Lidar observations are usually performed at night when scattering objects are not easily visible to the human eye. Therefore, it needs a judging method to classify scattering objects, aerosol or clouds composed mainly of ice crystals or ice crystals blown up near the observatory (in this study, clouds will be used as a general term for both clouds and ice crystals). In this section, we will discuss the quantitative features corresponding to the qualitative features of Type H and Type C objects shown by Shibata et al. (1996b) and discriminate between Type H and Type C.

Shibata et al. (1996b) reported results of the lidar observations in the late winter of 1993-94 at Eureka. They discussed the relation between the relative humidity over ice and the vertical profiles of scattering objects. They indicated that the scattering objects in the atmosphere could be classified into two groups, 'arctic aerosol layer' differentiated as Type H objects and 'other scattering objects' as Type C objects. The vertical profiles of Type C objects show fluctuating structures lasting from about an hour to about a day. On the other hand, the vertical profiles of Type H objects show very stable layers lasting for more than several hours. Figure 4.1 and Figure 4.2 illustrate the typical examples of the temporal variations of the scattering ratio and the depolarization ratio for Type C and Type H object profiles. The interval between successive profiles is two minutes. Figure 4.1 shows that the vertical profiles of Type C objects change dramatically within a few minutes. On the other hand, Figure 4.2 shows that the vertical profiles of Type H objects did not change no significantly over a period of hours and that the objects were usually arranged in layers.

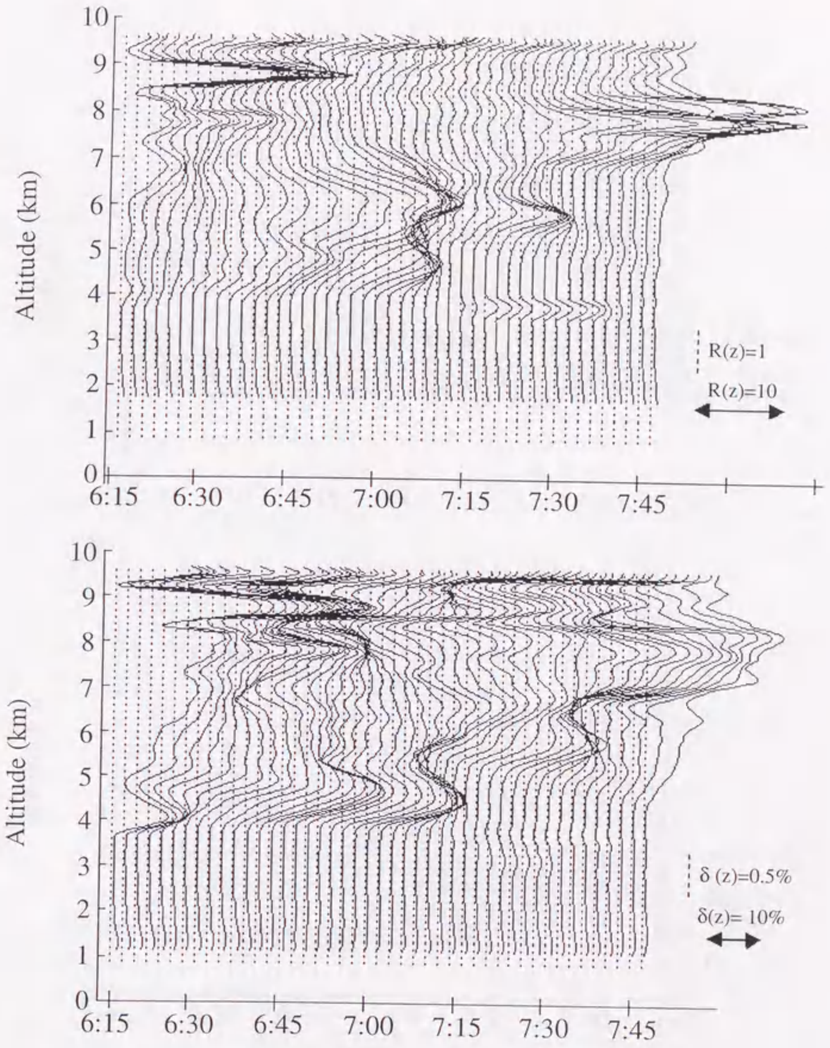

Figure 4.1 (upper panel) Time variation of vertical profiles of the scattering ratio of Type C objects observed from 0615 to 0745 LST on January 28, 1997. Each dashed line (left side of each file) is a standard line showing 'R(z)=1' for the adjacent profile. (lower panel) Time variation of vertical profiles of the depolarization ratio of Type C objects objects observed from 0615 to 0745 LST on January 28, 1997. Each dashed line (left side of each file) is a standard line showing 'δ(z)=0.5%' for the adjacent profile.

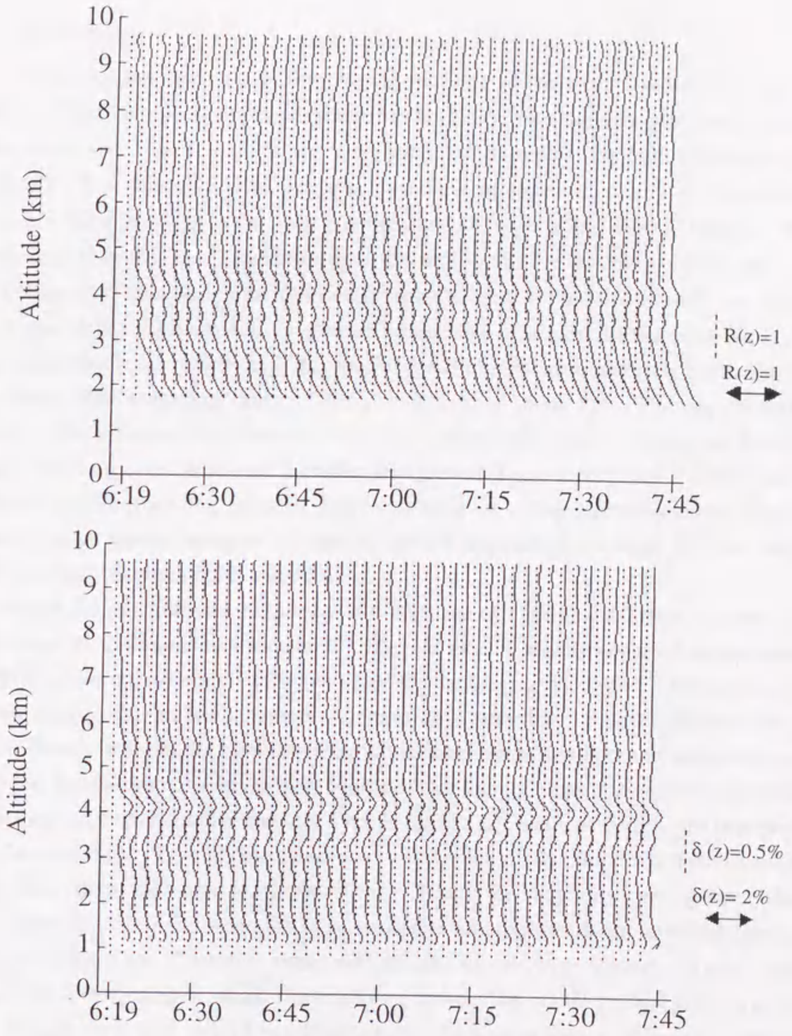

Figure 4.3 (upper panel) Time variation of vertical profiles of the scattering ratio of Type H objects observed from 0619 to 0750 LST on January 31, 1997. Each dashed line (left side of each file) is a standard line showing 'R(z)=1' for the adjacent profile. (lower panel) Time variation of vertical profiles of the depolarization ratio of Type H objects observed from 0619 to 0750 LST on January 31, 1997. Each dashed line (left side of each file) is a standard line showing 'δ(z)=0.5%' for the adjacent profile.

4.1.2 Discussion

In this section, we discuss the judging methods of scattering objects observed by lidar. Type H objects appeared when the humidity over ice was too low for cloud formation and Type C objects appeared when the humidity was high (Shibata et al., 1996b). The humidity over ice was examined in detail in search of quantitative features corresponding to the qualitative features of Type H and Type C objects. The relations between the humidity over ice and both the scattering ratio and the depolarization ratio during the four winter seasons from 1993-94 to 1996-97 are shown in Figure 4.3 and Figure 4.4. Figures illustrate that in almost all the cases the layers with less than roughly 60% humidity were Type H objects with extremely stable vertical profiles. The scattering ratios of these layers were about 1.3. The depolarization ratios of these layers ranged from 1% to 2%. Most of the Type C objects, on the other hand, were observed when the humidity was greater than roughly 80%. These layers had vertical profiles that changed every few minutes. The scattering ratios of these layers varied widely between 1.3 and 40 and the depolarization ratios of these layers varied widely between 0.5% and 40%.

Figure 4.5 illustrates the frequency of occurrence of Type H and Type C objects over the range of the humidities measured. Type H objects mostly occurred in the region with less than approximately 60% humidity. On the other hand, Type C objects occurred in the region with greater than approximately 80% humidity. Statistical evaluation of the relations between the humidity over ice measurements and both the scattering ratio and the depolarization ratio strongly indicates that Type C objects are clouds occurring in regions of high humidity and that Type H objects are arctic aerosol layers in regions of low humidity. Type H objects were very stable for a long period when the humidity was less than the approximately 60%. When the humidity was greater than approximately 80% and when the large scattering and depolarization ratios are large, it suggests that Type C objects composed mainly of ice were present. There were, however, a few cases in which the scattering objects had stable vertical profiles when the humidity was high as well as a few cases in which the scattering objects had vertical profiles fluctuating when the humidity was low.

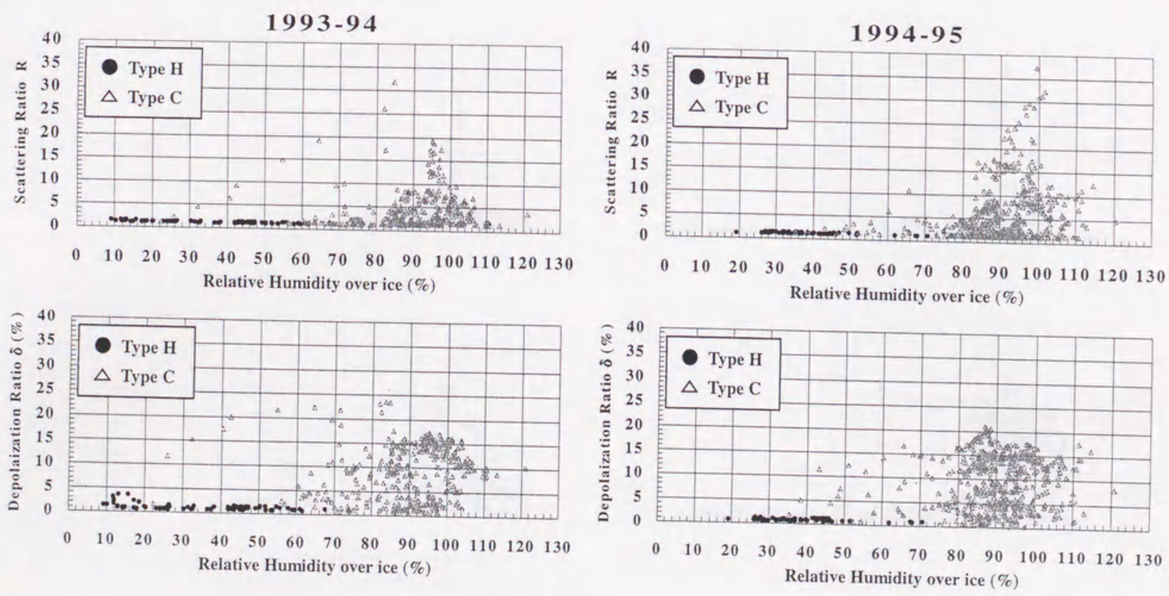

Figure 4.3 Scatter diagram showing the relation between the humidity over the ice and the scattering ratio (upper panel) and the total depolarization ratio (lower panel) of Type C(△) and Type H(●) observed during the winter seasons from 1993-94 to 1994-95.

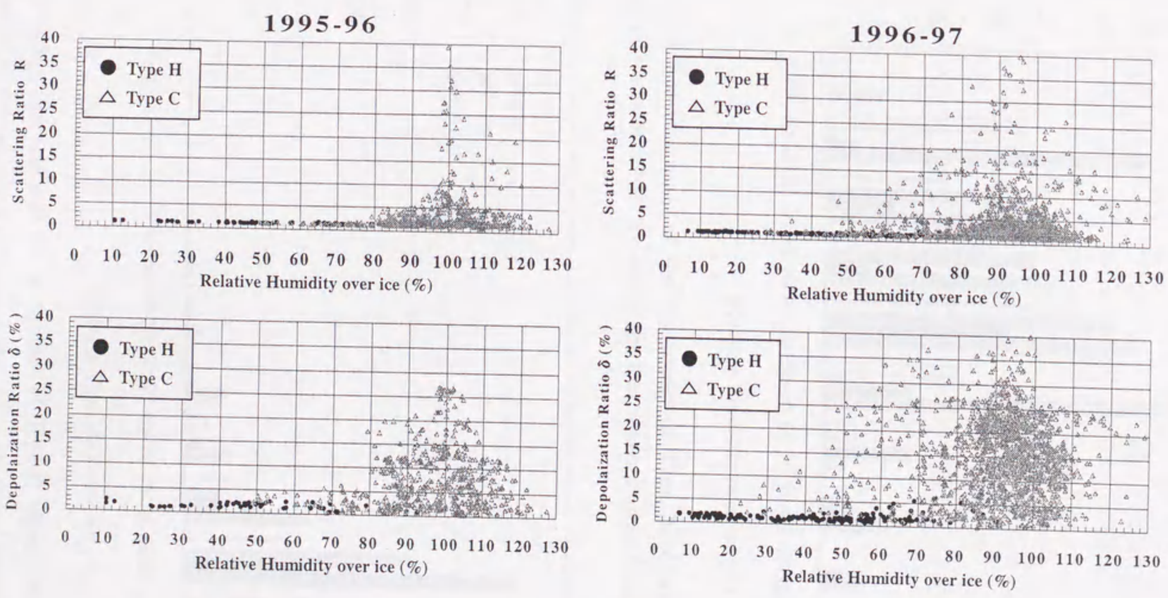

Figure 4.4 Same as Figure 4.3 but for the winter seasons from 1995-96 to 1996-97.

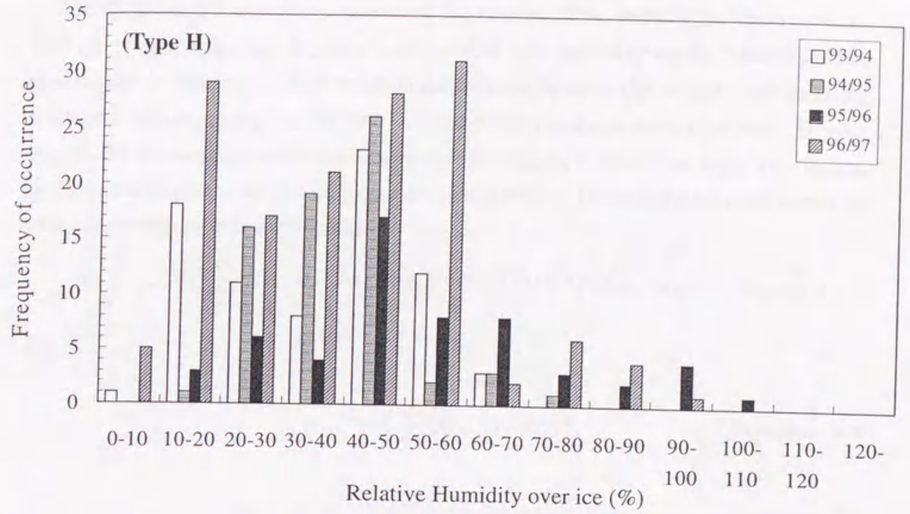

Figure 4.5(a) Frequency of the occurrence of Type H objects over the range of humidities measured over ice during the four winter seasons from 1993-94 to 1996-97.

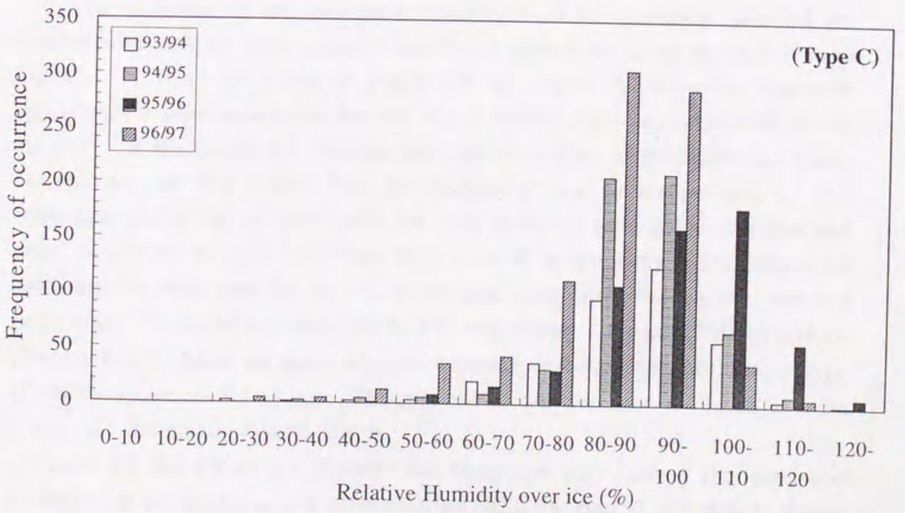

Figure 4.5(b) Frequency of the occurrence of Type C objects over the range of the relative humidity measured over ice during the four winter seasons from 1993-94 to 1996-97.

The correlation coefficients, indicating the change of the vertical profiles over time, were investigated in order to provide quantitative data regarding the fluctuation of Type H and Type C objects. The correlation coefficients between the vertical profiles of the scattering ratio observed by lidar at a reference time t and at a delay time t+Δt (Δt = 10, 20, 40, 60, 80 minutes) were calculated with the standard deviations $\sigma_{R(z,t)}$ and $\sigma_{R(z,t+\Delta t)}$ of the scattering ratio R(z,t) and R(z,t+Δt) (Ott, 1995). The correlation coefficients ρ_R of the scattering ratio is obtained as

$$\rho_{R(t)R(t+\Delta t)} = \frac{1}{n}\sum_{i=1}^{n}\left(R(z_i,t)-\overline{R}(t)\right)\left(R(z_i,t+\Delta t)-\overline{R}(t+\Delta t)\right)\Big/\sigma_{R(t)}\sigma_{R(t+\Delta t)}, \quad \text{Equation 4-1}$$

where

$$\sigma_{R(t)}{}^2 = \frac{1}{n}\sum_{i=1}^{n}\left(R(z_i,t)-\overline{R}(t)\right)^2, \quad \text{Equation 4-2}$$

$$\sigma_{R(t+\Delta t)}{}^2 = \frac{1}{n}\sum_{i=1}^{n}\left(R(z_i,t+\Delta t)-\overline{R}(t+\Delta t)\right)^2, \quad \text{Equation 4-3}$$

The correlation coefficients for the depolarization ratio profiles are calculated in the same manner as those for the scattering ratio.

Typical examples of the correlation relationship of the scattering ratio and the depolarization ratio for Type H objects and Type C objects are shown in Figure 4.6 and Figure 4.7. The lines shown in Figure 4.6 and Figure 4.7 show the first-order approximate expansion equation between R(z,t) and R(z,t+Δt) and between δ(z,t) and δ(z,t+Δt). If the correlation between the vertical profiles of the scattering objects observed at t and t+Δt is very close, the gradient of these lines approaches 1. The correlation coefficients of those ratios for Type H objects were stable over time and range from 0.96 to 1.00, and from 0.92 to 0.98, respectively. The correlation coefficients of those ratios for Type C, on the other hand, change widely over time and range from 0.00 to 0.90 and from 0.28 to 0.93 respectively. Figure 4.7 shows that the plots for Type C objects are scattered more and much more variable than those for Type H objects shown in Figure 4.6. The gradient of line for Type C objects is more changeable than that for Type H objects.

Figure 4.8 and Figure 4.9 illustrate the fluctuation over time of the correlation coefficient of the scattering and depolarizarion ratios for Type H and Type C objects obtained during the four winter seasons from 1993-94 to 1996-97. The correlation coefficients of the scattering and depolarization ratios for stable vertical profiles with low humidity (Type H) are relatively stable over time, changing from about 0.8 to 1.0.

On the other hand, the correlation coefficients of those ratios for fluctuating vertical profiles with high humidity (Type C) changed widely over time, from about 0.0 to 1.0. There are two distinctive differences between Type H suggesting arctic aerosol layers and Type C objects suggesting clouds. Even if lidar observations are performed during the polar night, it is possible to classify the scattering objects into two groups. It is, however, difficult to detect the arctic aerosol layer under the following conditions: (1) when the arctic aerosol layer could co-exist with many clouds, and (2) when the arctic aerosol layer could be present above thick clouds. Under the former condition, the signals from the arctic aerosol layer would be masked by the signals from clouds, and under the later condition, the arctic aerosol layer could not be detected because of the attenuation of the signals scattered by the arctic aerosol layer and the laser pulse by the lower cloud.

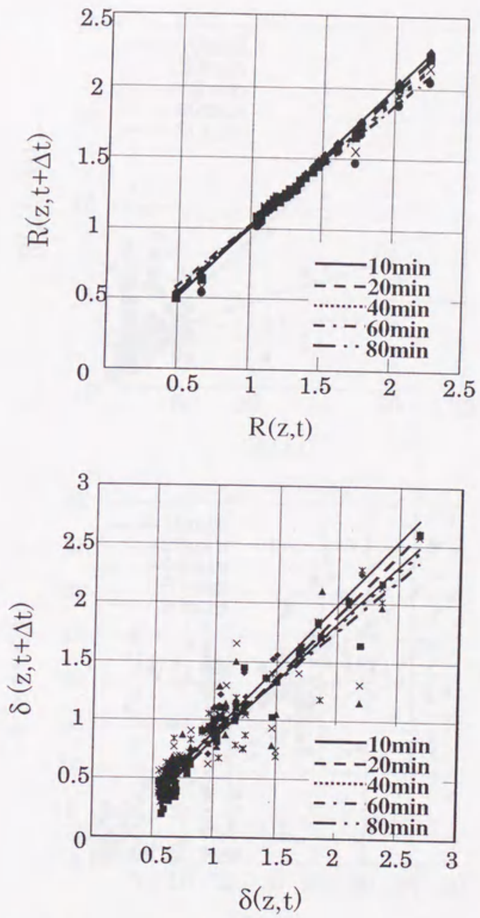

Figure 4.6 Scacter plots (upper panel) betweenn R(z,t) and R(z,t+Δt) and (lower panel) between δ(z,t) and δ(z,t+Δt) for Type H objects (♦: Δt=10mins; ■: Δt=20mins; ×: Δt=40mins; •: Δt=60mins; -: Δt=80mins).

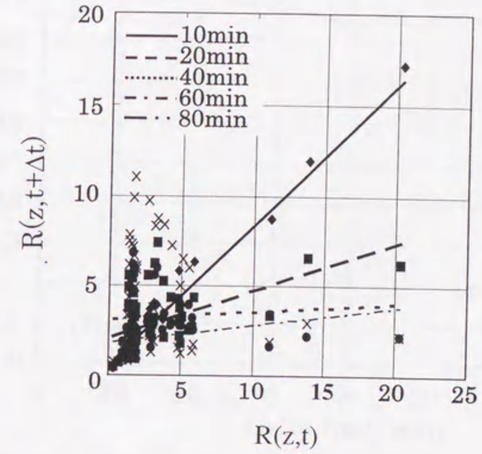

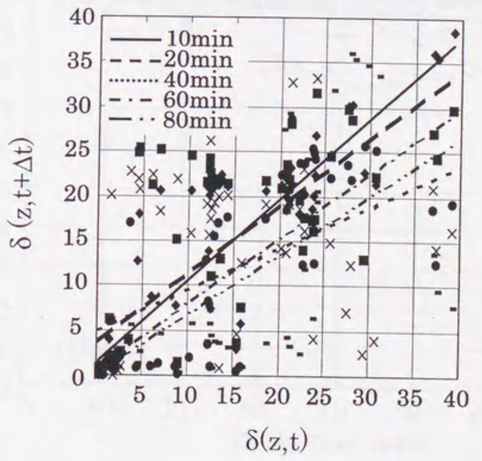

Figure 4.7 Scacter plots (upper panel) betweenn R(z,t) and R(z,t+Δt) and (lower panel) between δ(z,t) and δ(z,t+Δt) for Type C objects (♦: Δt=10mins; ■: Δt=20mins; ×: Δt=40mins; •: Δt=60mins; -: Δt=80mins).

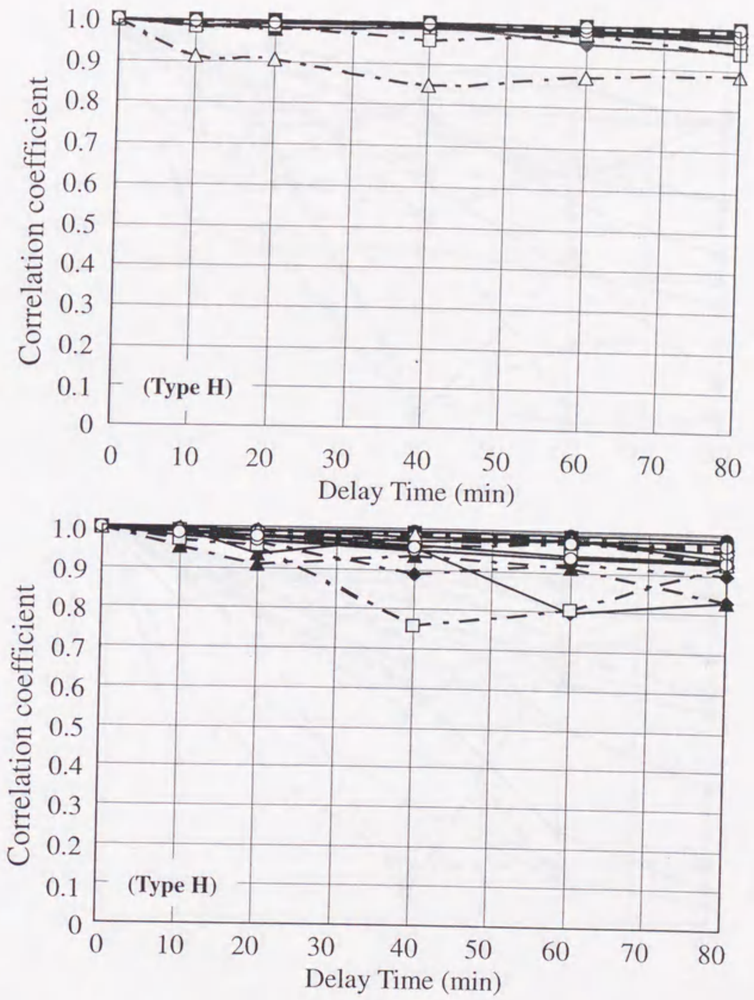

Figure 4.8 (upper panel) The fluctuation over time of the correlation coefficient of the scattering ratio for Type H objects obtained during the four winter seasons from 1993-94 to 1996-97. (lower panel) The fluctuation over time of the correlation coefficient of the depolarization ratio for Type H objects obtained during the four winter seasons from 1993-94 to 1996-97.

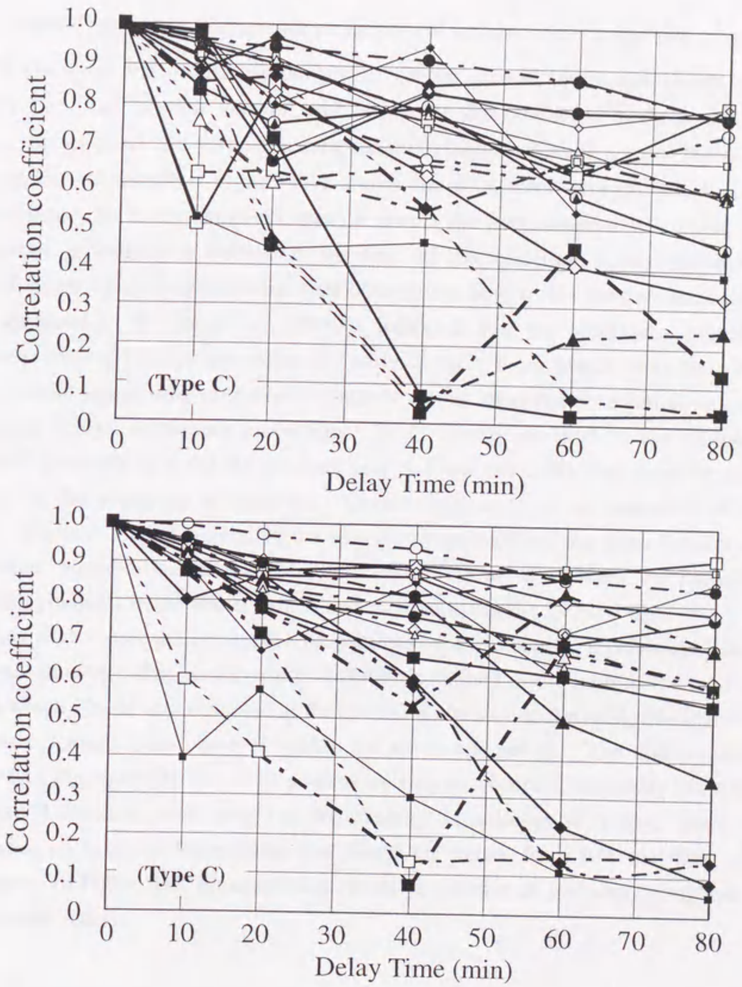

Figure 4.9 (upper panel)The fluctuation over time of the correlation coefficient of the scattering ratio for Type C objects obtained during the four winter seasons from 1993-94 to 1996-97. (lower panel) The fluctuation over time of the correlation coefficient of the scattering ratio for Type C objects obtained during the four winter seasons from 1993-94 to 1996-97.

4.2 Temporal and vertical occurrence probability of arctic aerosols and clouds.

We discussed the discrimination between arctic aerosol layers and clouds in the previous section. In this section, with using the discrimination methods described above, the temporal and vertical occurrence probabilities of arctic aerosol layers were investigated statistically. Figure 4.10 shows the occurrence probabilities for arctic aerosol layers for every two-week interval during the five observation seasons. The occurrence probability is defined as the ratio of the total time during which arctic aerosol layers were observed to the total observation time within the two-week period. Data gathered in the winter of 1994-95 indicated that the occurrence probability increased gradually in the late winter and early spring. From March 16 to 19 in 1995, arctic aerosol layers were observed throughout almost all of the observation time, thus producing a high occurrence probability. In the winter of 1995-96 the probability increased gradually as it did the previous year and was especially high from the end of January to the beginning of February. Observations early in the winter of 1996-97 winter indicated a similar trend in the occurrence probability, but from February the occurrence probability decreased rapidly. In the winter of 1997-98 the probability increased gradually in the winter season and early spring as the 1994-95 did.

Figure 4.11 shows the occurrence probabilites of arctic aerosol layers and clouds at different altitudes. The occurrence probability is defined as the ratio of the total time during which clouds was observed at the specified altitudes to the total time that arctic aerosols or clouds were observed within the two-week period. The upper panel of Figure 4.11 illustrates that the arctic aerosol layers were observed frequently at altitudes less than 3 km and were observed occasionally at altitudes of 3 to 5 km. The occurrence probabilities for altitudes less than 5 km ranged from 80% to 100%. The lower panel of Figure 4.11 illustrates that clouds occurred at all altitudes throughout the entire winter season.

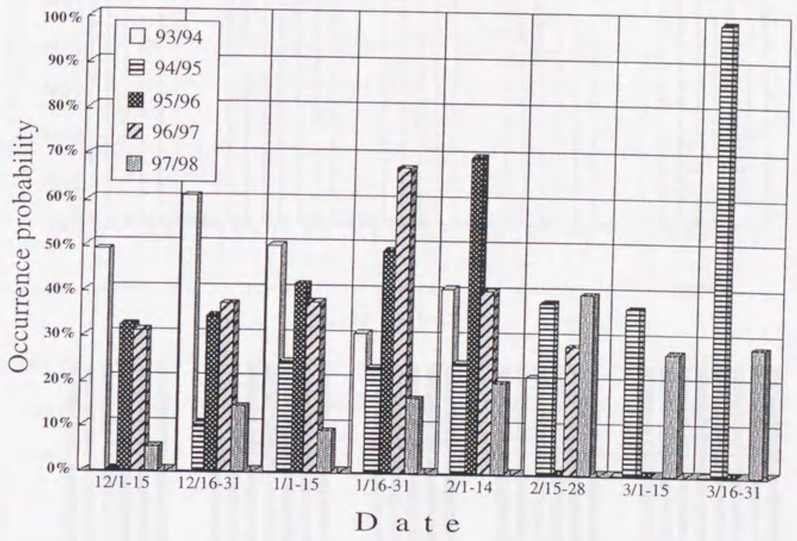

Figure 4.10 Arctic aerosol layers occurrence probabilities for every two-week interval during the five observations seasons.

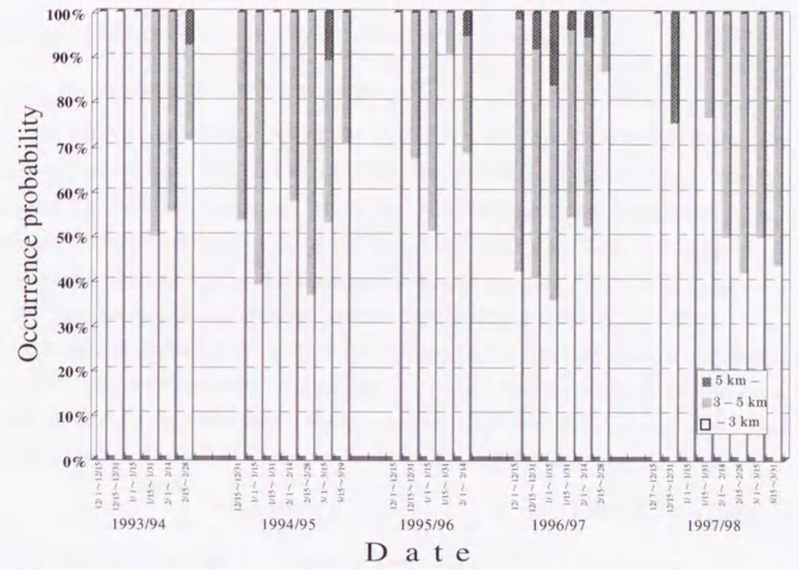

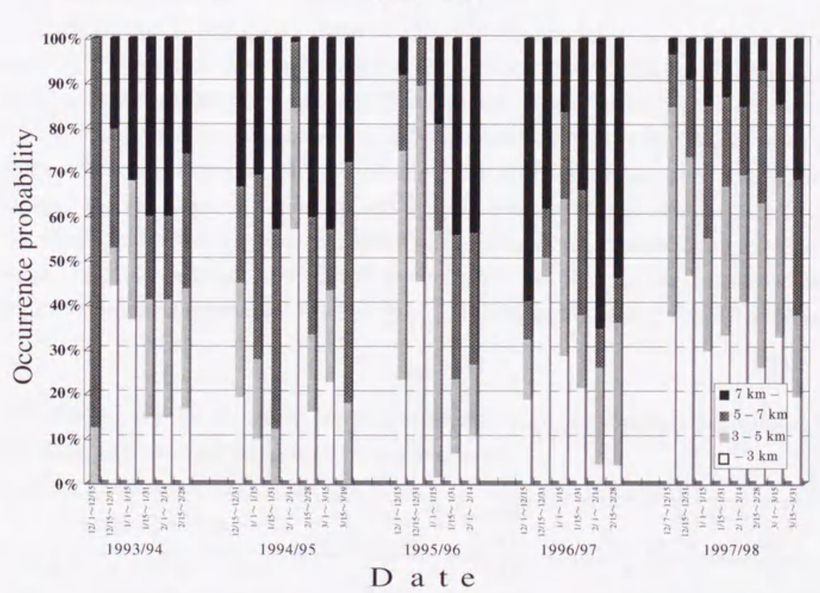

Figure 4.11 (upper panel) Arctic aerosol layers and (lower panel) clouds occurrences probabilities at different altitudes observed during the winter seasons from 1993-94 to 1997-98.

4.3 Characteristics and long-range transport of arctic aerosol layer

4.3.1 Optical property of arctic aerosol layer

The optical information about the arctic aerosol layers observed during the five winter seasons from 1993-94 to 1997-98 was investigated statistically. The averages of and the standard deviations (σ) of the Mie backscattering coefficient β_M and the aerosol depolarization ratio δ_a of arctic aerosol layers are listed in Table 4.1. The five-winter average Mie backscattering coefficient $\beta_{M,\,0.532\mu m}$ is 5.3±3.4 ($\bar{x}\pm\sigma$) $\times 10^{-7}$ m $^{-1}$ sr $^{-1}$, and the five-winter average aerosol depolarization ratio δ_a is 5.2±3%.

The optical depth τ_{AL} of arctic aerosol layer can be calculated under the assumption that the Mie backscattering coefficient $\beta_{M,\,0.532\mu m}$ and the ratio S of the extinction coefficient $\sigma_{M,\,0.532\mu m}$ to the Mie backscattering coefficient $\beta_{M,\,0.532\mu m}$ are constant in the aerosol layer. The values of τ_{AL} can be calculated by the following equation,

$$\tau_{AL} = \int_{\text{Bottom of layer}}^{\text{Top of layer}} \sigma(z)dz = \int_{\varpi=4\pi} \int_{\text{Bottom of layer}}^{\text{Top of layer}} S \cdot \beta_M(z)dz\, d\varpi \,, \qquad \text{Equation 4-4}$$

The calculated optical depth is listed in Table 4.2. The actual ratio of $\sigma_{M,\,0.532\mu m}$ to $\beta_{M,\,0.532\mu m}$ of aerosols is unknown. Jäger et al. (1995) reported that the ratio ranges from about 20 to about 40. Although the value of τ_{AL} depends on the depth of the layer and the value of S, the value of τ_{AL} is assumed to be in the range of ~0.05-0.15.

87 arctic aerosol layers were observed by our lidar during the five winter seasons. Figure 4.12 shows examples of the vertical profiles of the scattering ratios $R_{1.064\mu m}$ and $R_{0.532\mu m}$, and the Ångström exponent values α of arctic aerosol layers. Although we could not calculate the Ångström exponent values α for all the cases because of the low quality of the observed backscattering coefficient $\beta_{M,\,1.064\mu m}$, we calculated the Ångström exponent α for about twenty cases. The Ångström exponent α of the layers

Table 4.1 The average Mie backscattering coefficient β_M and the aerosol depolarization ratio δ_a for arctic aerosol layers for five-winter seasons.

Observation term	β_M ($\times 10^{-7}$ /m/sr)		δ_a (%)	
	Average	1σ	Average	1σ
Dec 5, 1993- Mar 1, 1994	5.9	2.9	3.8	2.0
Dec 12, 1994- Mar 19, 1995	4.5	3.1	3.6	2.2
Dec 2, 1995- Feb 15 , 1996	6.0	2.9	6.4	3.9
Nov 29, 1996- Feb 27, 1997	6.1	3.8	5.4	3.0
Dec 7, 1997- Mar 31 , 1998	3.7	2.7	6.1	2.9
5 winter	5.3	3.4	5.2	3.0

ranged between 0.8 and 1.2. The Ångström exponent α is smaller for the aerosol layers than for the altitudes above or below that layer. This was true in all the cases investigated. The Ångström exponent α suggested that the larger particles increased in the layer.

Table 4.2 The optical depth calculated using Equation 4-4 and the five-winter average Mie backscattering coefficient β_M.

Depth of aerosol layer (m)	S			
	10	20	30	40
50	0.003	0.007	0.010	0.013
100	0.007	0.013	0.020	0.027
200	0.013	0.027	0.040	0.053
500	0.033	0.067	0.100	0.133
1000	0.067	0.133	0.200	0.266

4.3.2 Long-range transport of arctic aerosol layer

We calculate isentropic backward trajectories to discuss the long-range transport and source regions of arctic aerosol layers observed in the troposphere. After the calculation, ten-day isentropic trajectories of arctic aerosol observed over Eureka during winter seasons from 1993-94 to 1997-98 were divided into three altitudes groups for convenience. The trajectories for arctic aerosols observed at altitudes of 2 - 3 km asl, 3 - 4 km asl, and more than 4km asl are shown in the three parts of Figure 4.13. Most of trajectories shown in Figures 4.13(a) and 4.13 (b) are transported from across the Arctic Ocean and are consistent with the cases Raatz (1991) described. The vicinity of the Novosibirskije islands (76° N, 141° E), Russia, was the confluence of trajectories from two directions - those from northern and northwestern Russia having cyclonic flow, and those from eastern Siberia having anticyclonic flow. Figure 4.13 indicates that the frequency of the trajectories from eastern Siberia in the trajectories for the layers observed at altitudes of more than 3 km asl increased when compared with that for the layers observed at altitude of 2-3 km asl. The transport from eastern Siberia was related to the extension of a high-pressure system over Alaska.

Most tropospheric aerosols are released from the surface of the Earth into the boundary layer. They affect the chemical compositions of the boundary layer and transported to the upper troposphere, but we have little information about the spatial and temporal variations of the aerosol in the troposphere. If there were no aerosol sources

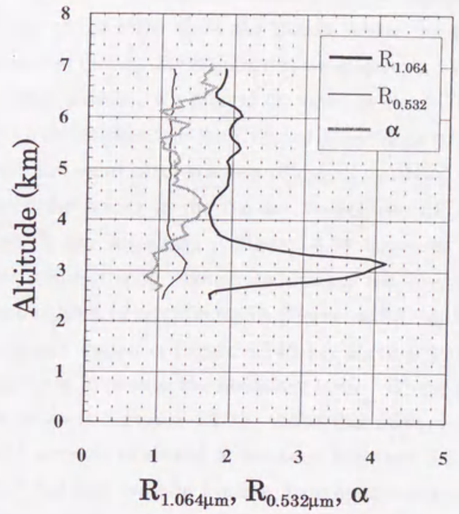

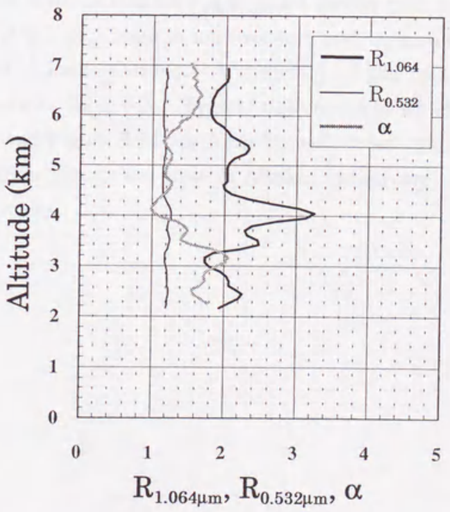

Figure 4.12 Vertical profiles of the scattering ratios ($R_{1.064\mu m}$, $R_{0.532\mu m}$) and Ångström exponent α of arctic aerosol layer observed at altitude of (upper) about 3.2 km asl on 3 January 1995 and (lower) 3.6 km asl, 4.1 km asl and 5.3 km asl on 31 January 1997.

in the free troposphere along the trajectories, the chemical composition of arctic aerosol layers we observed by lidar would be determined by the composition of the boundary layer. Figures 4.14(a) and 4.14(b) show the points where the track altitudes in the five-day trajectories and in the ten-day trajectories were lowest. When a trajectory had more than one minimum altitude, we plotted the point at the first minimum altitudes. Figure 4.14(a) shows that the points in the five-day trajectories of aerosols observed at altitudes higher than 3 km were small fraction of the all symbols, while Figure 4.14(b) shows that number of the points in the ten-day trajectories of aerosols observed at altitudes higher than 3 km increased. Figure 4.14 suggests that Five-day back trajectories, however, are not long enough to discuss the long-range transport and possible distant source regions of arctic aerosols (Harris and Kahl, 1994). The average track altitude of the points shown in Figure 4.14(b) is about 0.8 km asl (σ = 0.4 km). That is, most of them were in or near the boundary layer. These points were near the source regions of the aerosols. Figure 4.14(b) shows that most of the low points in the ten-day trajectories of aerosols observed at altitudes less than 3 km were at latitudes higher than 60° N and that they were in Eurasia, near open water and near the coast of or over the Arctic Ocean. Figure 4.14(c) shows that most of the low points in the ten-day trajectories of aerosols observed at altitudes greater than 3 km were at latitudes lower than 60° N and that they were in northwestern and western Canada or Eurasia or over the Pacific and Atlantic Oceans. A summary of the source regions of arctic aerosol layers is shown in Table 4.3. Typical trajectories to which attention should be paid in Figure 4.13 and Figure 4.14 are from Eurasia, from near or over open water, from the coast of eastern Siberia and western Alaska, and staying over the frozen Arctic Ocean and at low altitudes.

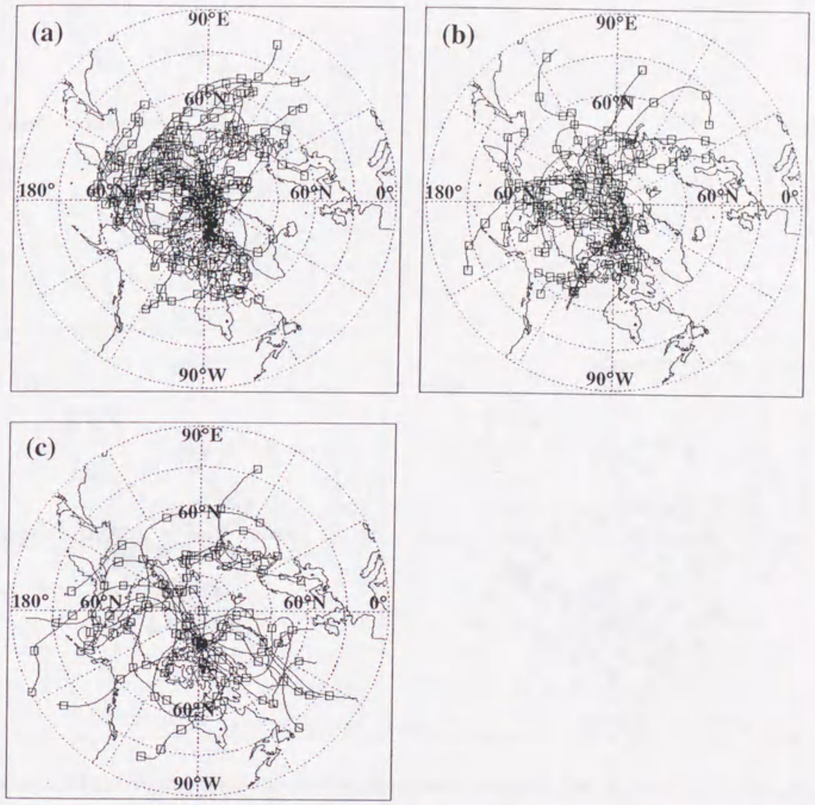

Figure 4.13 The isentropic backward trajectories for arctic aerosols observed at altitudes of (a) 2 - 3 km asl, (b) 3 - 4 km asl and (c) higher than 4 km asl during the winter seasons from 1993-94 to 1997–98.

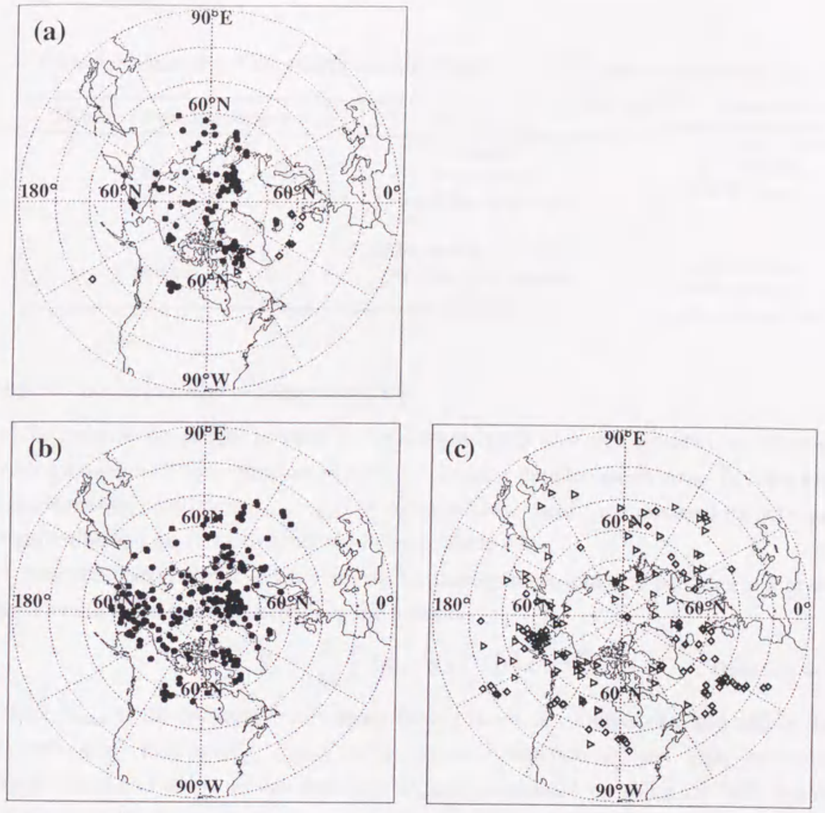

Figure 4.14 (a) Scatter diagram showing the points where the track altitudes in five-day backward trajectories of arctic aerosol layers observed by lidar over Eureka at various altitudes during the winter seasons from 1993-94 to 1997-98 were lowest: (●) 2-3 km asl, (Δ) 3-4 km asl, and (◊) ≥ 4 km asl. (b) Scatter diagram showing the points where the track altitudes in ten-day backward trajectories of arctic aerosol layers observed by lidar over Eureka at altitudes of 2-3 km asl were lowest. (c) The same as Figure 4.14(b) but for at altitudes of (Δ) 3-4 km asl, and (◊) ≥ 4 km asl.

Table 4.3 Summary of the source regions of arctic aerosol layers observed by lidar.

Altitude of arctic aerosol layer	Source Region	Latitude distribution
≤ 3km asl	Eurasia Arcic Ocean Coast of the Arctic Ocean	> 60° N (77%) < 60° N (23%)
> 3km asl	Atlantic and Pacific Oceans Northwerstern Canada Eurasia	> 60° N (40%) < 60° N (60%)

4.3.3 Model calculation of lidar parameters

To estimate the size of aerosols in the aerosol layers observed by lidar, we calculate lidar parameters (the Ångström exponentα, aerosol depolarization ratio δ_a, and Mie backscattering coefficient $\beta_{M,0.532\mu m}$) by using the Mie theory, the modeled particle size distribution and the refractive indexes listed in Table 4.4.

The Mie backscattering coefficient β_M for homogenous spherical particles at a given wavelength λ can be calculated using the formula

$$\beta_M = \frac{1}{4\pi}\int_0^\infty Q_{back}\cdot\pi r^2\cdot n(r)dr, \qquad \text{Equation 4-5}$$

where Q_{back} is the backscatter efficiency for a particle at a radius of r and n(r) is the particle size distribution. Q_{back} is a complex function of the size, chemical composition and shape of the particle. Q_{back} is calculated by using the Mie theory (Bohren and Huffman, 1983).

In this study, we assumed two cases for the chemical composition of the aerosols. In Case I the aerosol layers are composed of sulfate aerosol particles in the accumulation mode (diameter < 1 μm) and natural aerosol particles in the coarse mode (diameter > 1 μm). In Case I, we supposed arctic haze phenomena. The particle size distribution parameters and the refractive indexes of the particles used to calculate the Mie backscattering coefficient β_M were chosen by referring the literature (e.g. Brock et al., 1990; Staebler et al., 1999). In Case II, since the concentration of sea salt becomes high in late autumn and in winter, we assumed that the natural aerosols were composed of sea salt. The information about the particle size distribution of sea salt in the arctic troposphere is few (Watanabe et al., personal communication, 1999). But because short residence time of large particles would result in most of them being removed from the atmosphere during long-range transport, we assumed that the aerosol layers consist of a large number of small particles and a small number of large particles. We

Table 4.4(a) Bi-modal log-normal size distribution parameters and refractive indexes of materials used for the model calculation of lidar parameters

(a) Bi-modal log-normal size distribution parameters

Size distribution prameter	Accumulation mode	Coarse mode
Number concentration (/cm^3)	100, 200, 300	0.01, 0.05, 0.1, 0.15, 0.2, 0.5
Geometric mean diameter (μm)	0.2, 0.3, 0.4, 0.6	0.3-4
Geometric standard deviation	1.45, 1.50, 1.55	1.4, 1.5, 1.6

(b) Refractive indexes and aerosol depolarization ratios of materials

	Case I: Sulfate and natural aerosols		Case II: Sea salt	
	Accumulation mode (H_2SO_4)	Coarse mode (sea salt, soil dusts, etc)	Accumulation mode (sea salt)	Coarse mode (sea salt)
Refractive inedxes of material	1.412 [1] -0i*	1.52-0.01i [2]	1.544 [1]	1.544 [1]
Aerosol depolarization ratio	0%	25%	0%	20%

1 Tang (1996) 2 Brock et al. (1990)0i* ≡ $<10^{-5}$

calculated the Mie backscattering coefficient β_M by using the Mie theory, the modeled particle size distribution and the calculated refractive indexes listed in Table 4.4.

The Mie backscattering coefficients, $\beta_{M,\ 1.064\mu m}$ and $\beta_{M,\ 0.532\mu m}$, were calculated by using Equation 4-5 and the Ångström exponent α of the modeled aerosol layers were calculated by using Equation 3-5.

The aerosol depolarization ratio δ_a was calculated under the assumption that the accumulation mode particles may or may not be spherical and that the coarse mode particles are nonspherical. The aerosol depolarization ratio was defined as

$$\delta_a = \frac{\delta_{a,\,Accumu} \times \beta_{M,\,Accumu} + \delta_{a,\,Coarse} \times \beta_{M,\,Coarse}}{\beta_{M,\,Accumu} + \beta_{M,\,Coarse}} \times 100\ [\%], \quad \text{Equation 4-6}$$

where $\beta_{M,\ Accumu}$ and $\beta_{M,\ Coarse}$ are the Mie backscattering coefficients for the accumulation mode and coarse mode particles and where $\delta_{a,\ Accumu}$ and $\delta_{a,\ Coarse}$ are the aerosol depolarization ratios for the accumulation mode and coarse mode particles.

If particles are spherical, their aerosol depolarization ratio is 0%. Even if they are not spherical, their aerosol depolarization ratio will be close to 0% if their radius of the particles is smaller than the wavelength of the laser beam. Since the radii of the accumulation mode particles we defined are smaller than the wavelength of the laser beam, the aerosol depolarization ratio of the accumulation mode particles is assumed to be 0%. The aerosol depolarization ratio of a particle of diameter less than about 0.6 μm given by some numerical calculations shows that the ratio ranges from 0% to about 2% (e.g., Mishchenko and Sassen, 1998; Murayama et al., 1999). Although assuming the aerosol depolarization ratio of these particles to be 0% leads to a difference of at most 0.5 μm when the geometric mean diameter of the coarse mode particles is determined, this assumption does not affect the essentials of the following discussions. The actual aerosol depolarization ratio of the coarse mode particles is also unknown. Some studies report that the aerosol depolarization ratios of sea salt and dust particles are about 20% (Murayama et al., 1999; Sakai et al., 2000) and 25% (Sakai et al., 2000), respectively. Mishchenko and Sassen (1998) calculated the aerosol depolarization ratio of the nonspherical particles theoretically. They reported that at a wavelength of 0.532 μm the aerosol depolarization ratio of the nonspherical particles would be roughly 30%. In this study we assumed that when the aerosols are composed of various particles (e.g., sea salt and dust particles) the aerosol depolarization ratio of the coarse mode particles was 25%.

Figures 4.14(a) through 4.14(r) show examples of the relations between the geometric mean diameter D_2 of the coarse mode particles and the Ångström exponent α, the aerosol depolarization ratio δ_a, and the Mie backscattering coefficient $\beta_{M,\ 0.532\mu m}$ for

the sulfate and natural aerosols (Case I). Figures 4.14(a), 4.14(d), 4.14(g) and 14(j) indicate that $\beta_{M,\,0.532\mu m}$ depends on the geometric mean diameter D_1 of accumulation mode particles. Figures 4.14(a) through 14(c) also indicate that $\beta_{M,\,0.532\mu m}$ depends on the number concentration N_1 of accumulation mode particles. When the geometric mean diameter D_1 of the accumulation mode particles with the number concentration N_1 of 200 cm^{-3} is 0.3 μm and the number concentration N_2 of the coarse mode particles is 0.10 cm^{-3}, $\beta_{M,\,0.532\mu m}$ is about 5×10^{-7} m^{-1} sr^{-1} (Fig. 4.14(e)). Figure 4.14(m) shows that, when the number concentration of coarse mode particles is very low, the values ofα and δ_a are very different from those obtained from lidar observations. Figure 4.14(m) suggests that the existence of coarse mode particles is important to obtain the the values of α and δ_a similar to those obtained from lidar observations. When N_2 of the coarse mode particles is the range of 0.05-0.5 cm^{-3}, the calculations indicate the values of α, $\beta_{M,\,0.532\mu m}$, and δ_a similar to those obtained from lidar.

We also calculated $\beta_{M,\,0.532\mu m}$ for the case of the sea salt (Case II). We investigated the relations between D_2 and both α and δ_a. Figures 4.15(a) through 4.15(o) show examples of the relations between D_2 and α, δ_a, and $\beta_{M,\,0.532\mu m}$ for Case II. When the geometric mean diameter D_1 of the accumulation mode particles with the number concentration N_1 of 300 cm^{-3} is 0.2 μm and the number concentration N_2 of the coarse mode particles is the range of 0.1-0.15 cm^{-3}, the calculations indicate the values of α, $\beta_{M,\,0.532\mu m}$, and δ_a similar to those obtained from lidar.

The modeled calculation of lidar parameters suggests that the geometric mean diameter of accumulation mode particles is the range of 0.2-0.3 μm. Although Figures 4.14(m) through 4.14(r) and Figures 4.14(j) through 4.14(o) show that $\beta_{M,\,0.532\mu m}$ depended on N_2 and D_2, the calculations indicated that $\beta_{M,\,0.532\mu m}$ was determined mainly by N_1 and D_1. The calculations also indicated that both the increase of δ_a and the decrease of α depend on N_2 and D_2. Even if number of coarse mode particles in the aerosol is small, their existence is important in determining the values of α, and δ_a. A summary of the parameters giving α, $\beta_{M,\,0.532\mu m}$, and δ_a values similar to those obtained from lidar observations is listed in Table 4.5.

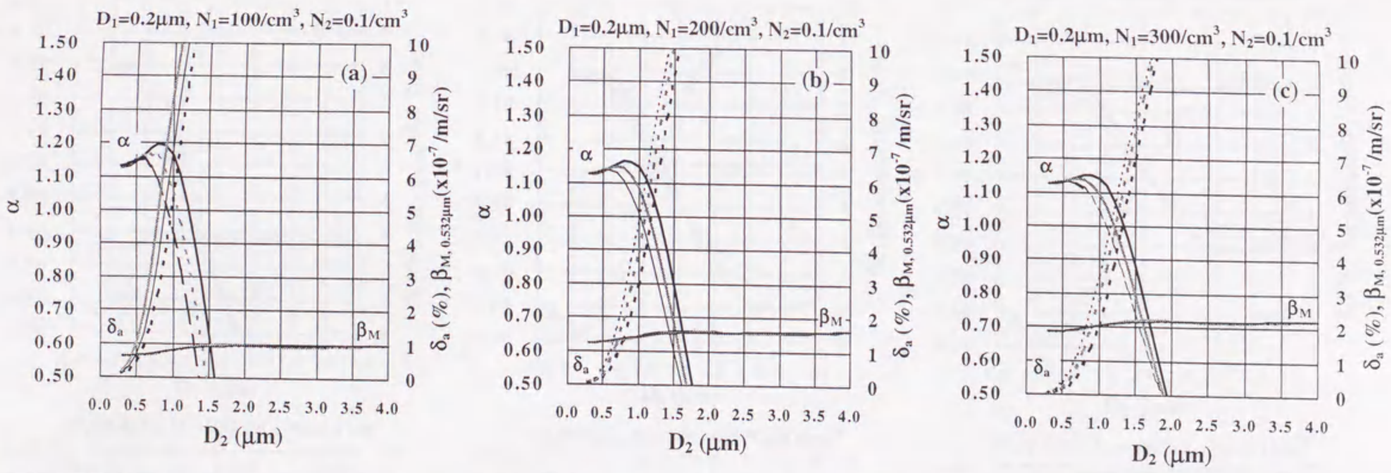

Figure 4.14 Relation between the geometric mean diameter of the coarse mode particles in aerosols and the Ångström exponents α (solid lines), aerosol depolarization ratios δ_a (dotted lines), and the backscattering coefficient β (horizontal lines) calculated for the sulfate and natural aerosols case. N_1 and D_1 are the number concentrations and the geometric mean diameter for the accumulation mode particles, respectively. N_2 and D_2 are those for the coarse mode particles, respectively. Each set of lines shows the values calculated for various geometric mean standard deviations σ_2 (= 1.4 (thick black line), 1.5 (thick gray line) and 1.6 (thin black line)). The refractive indexes for the accumulation mode and coarse mode particles are 1.412-0i and 1.52-0.01i, respectively.

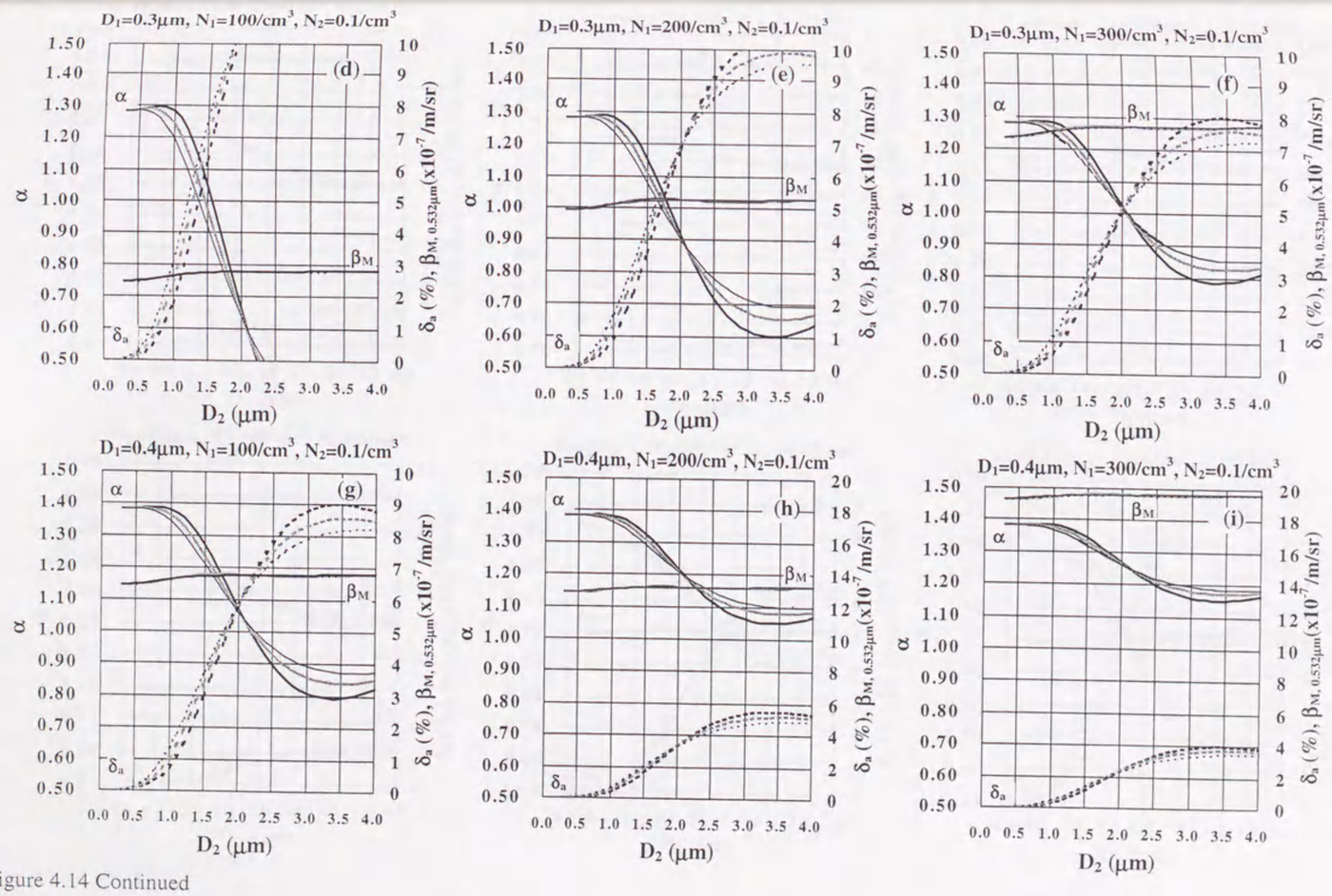

Figure 4.14 Continued

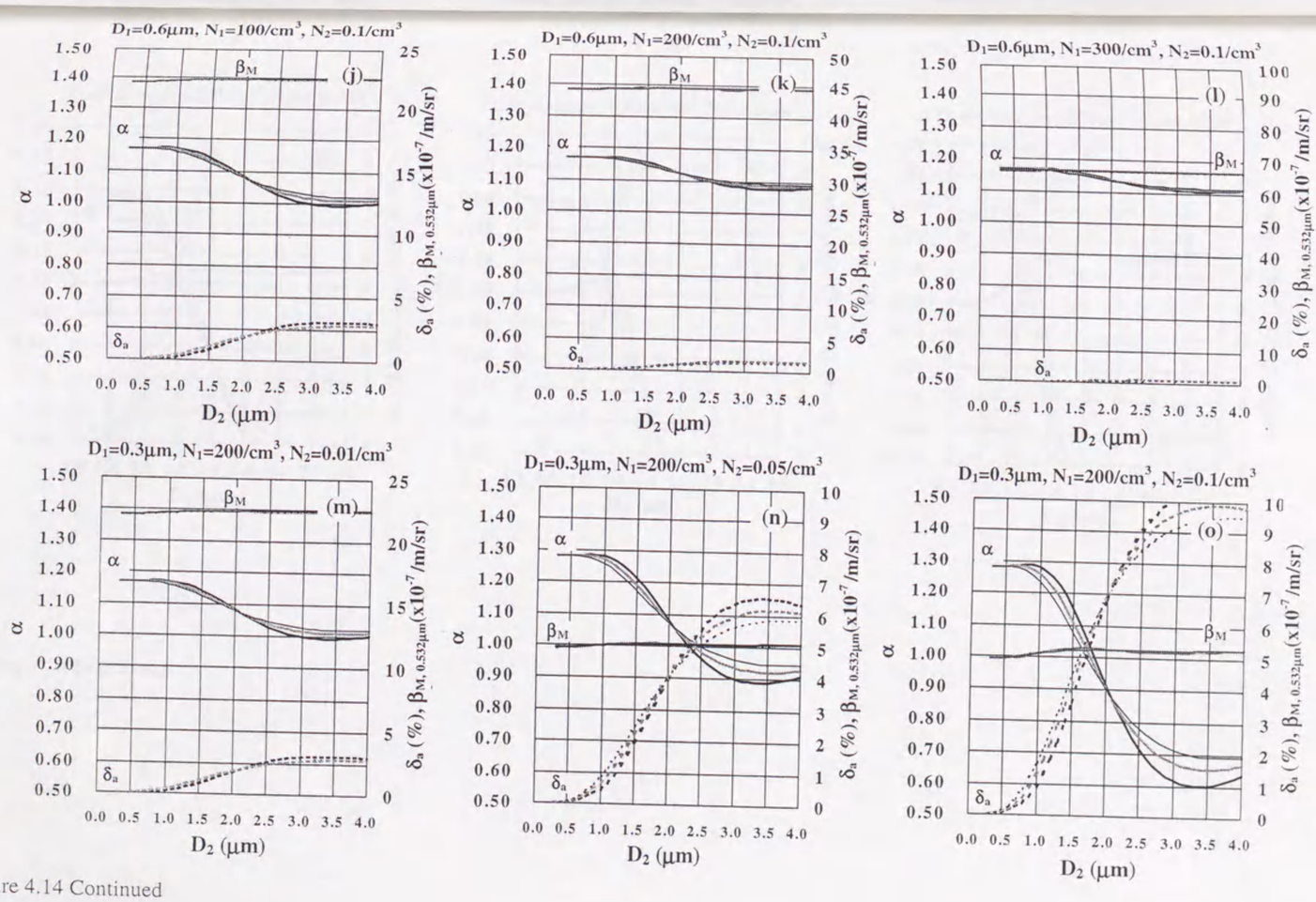

Figure 4.14 Continued

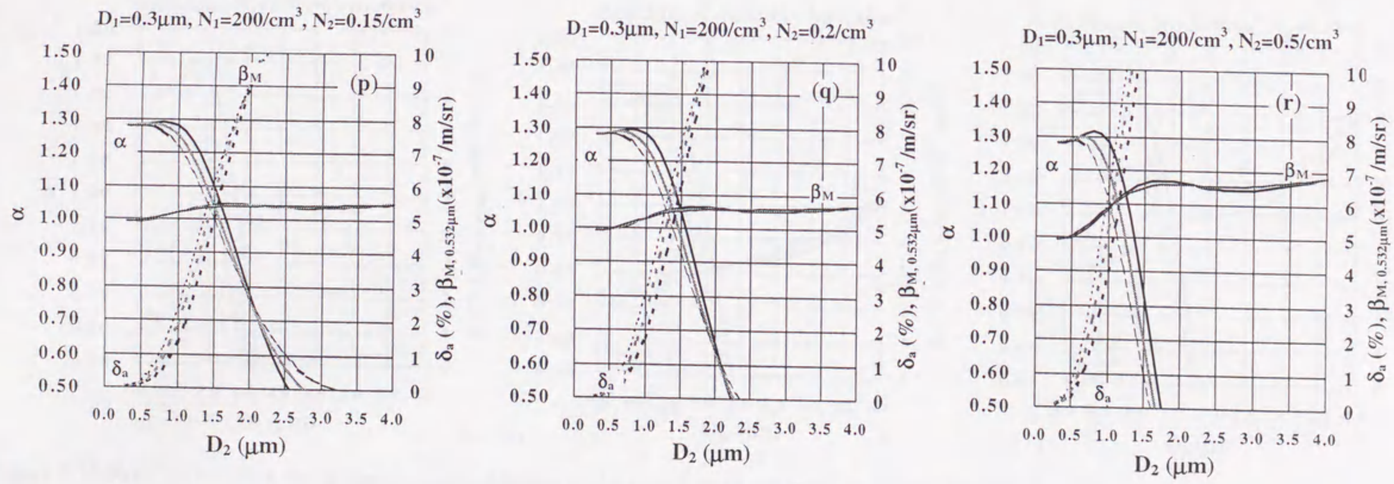

Figure 4.14 Continued

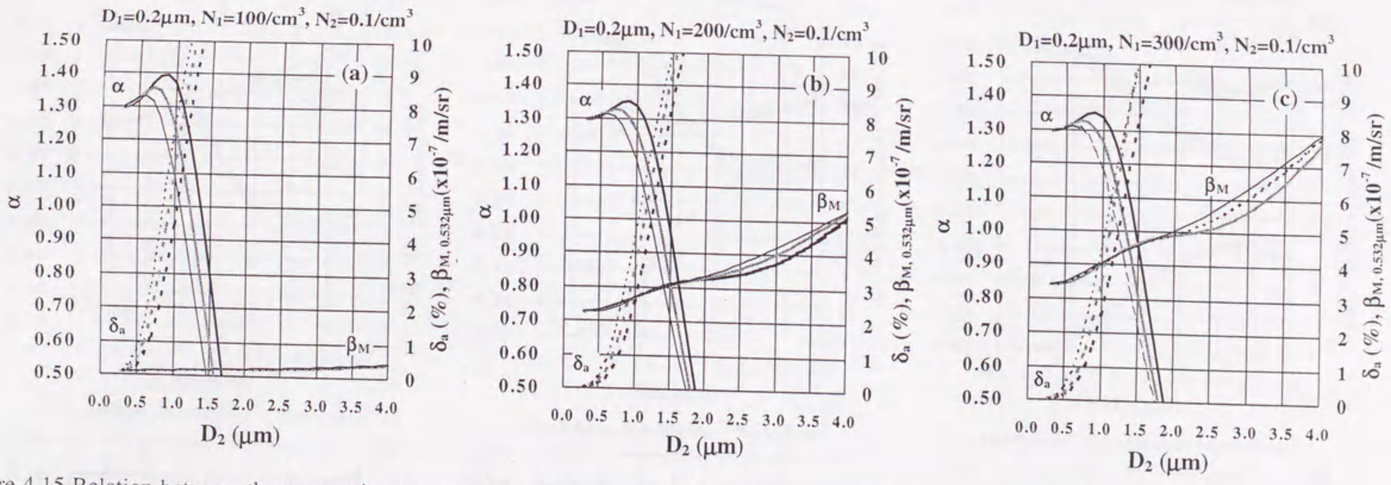

Figure 4.15 Relation between the geometric mean diameter of the coarse mode particles in aerosols and the Ångström exponents α (solid lines), aerosol depolarization ratios δ_a (dotted lines), and the backscattering coefficient β (horizontal lines) calculated for the sea salt case (Case II). N_1 and D_1 are the number concentrations and the geometric mean diameter for the accumulation mode particles, respectively. N_2 and D_2 are those for the coarse mode particles, respectively. Each set of lines shows the values calculated for various geometric mean standard deviations σ_2 (= 1.4 (thick black line), 1.5 (thick gray line) and 1.6 (thin black line)). The refractive indexes for the accumulation mode and coarse mode particles used to calculate the Mie backscattering coefficient β for the sea salt case (Case II) are 1.544-0i and 1.544-0i, respectively.

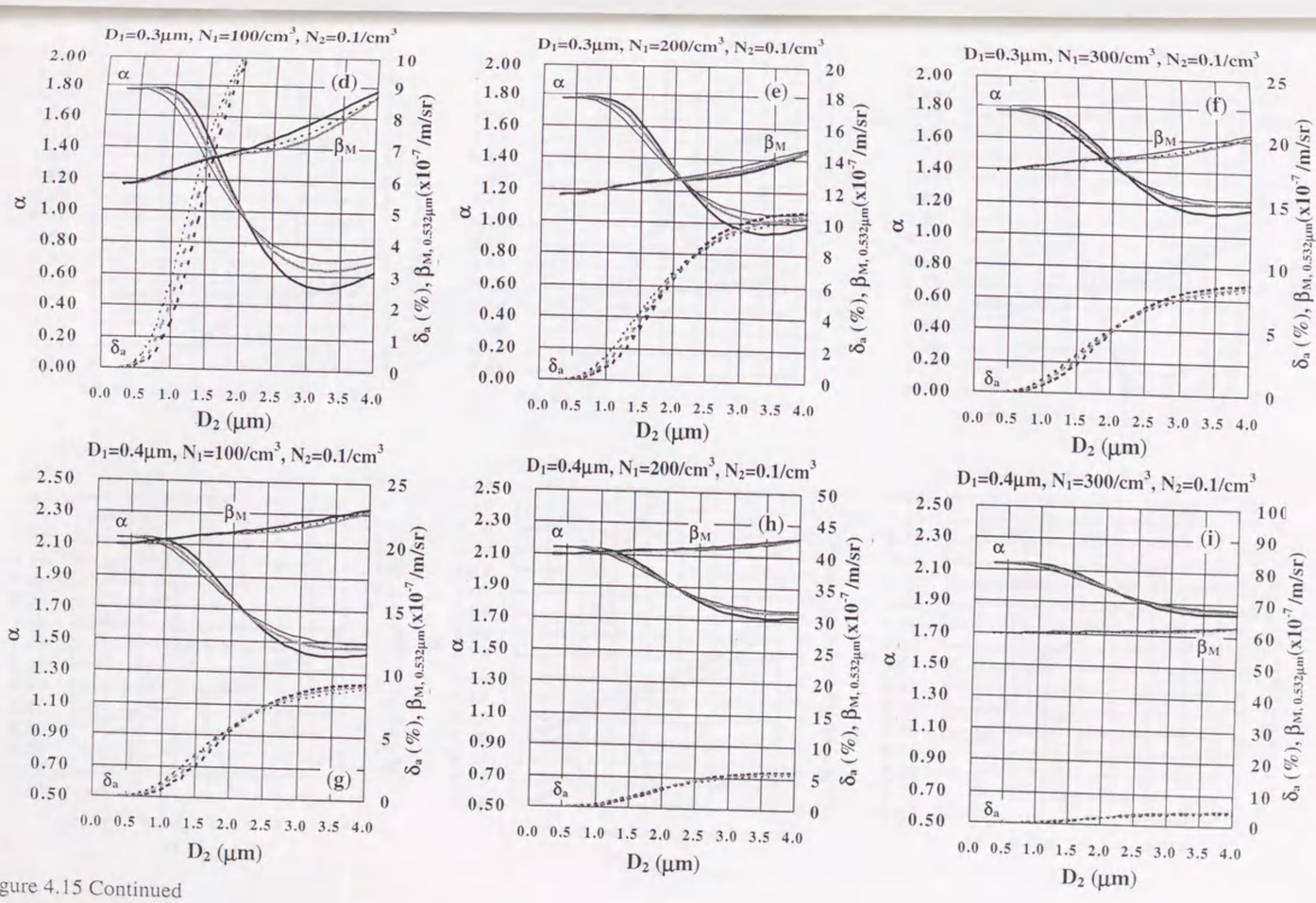

Figure 4.15 Continued

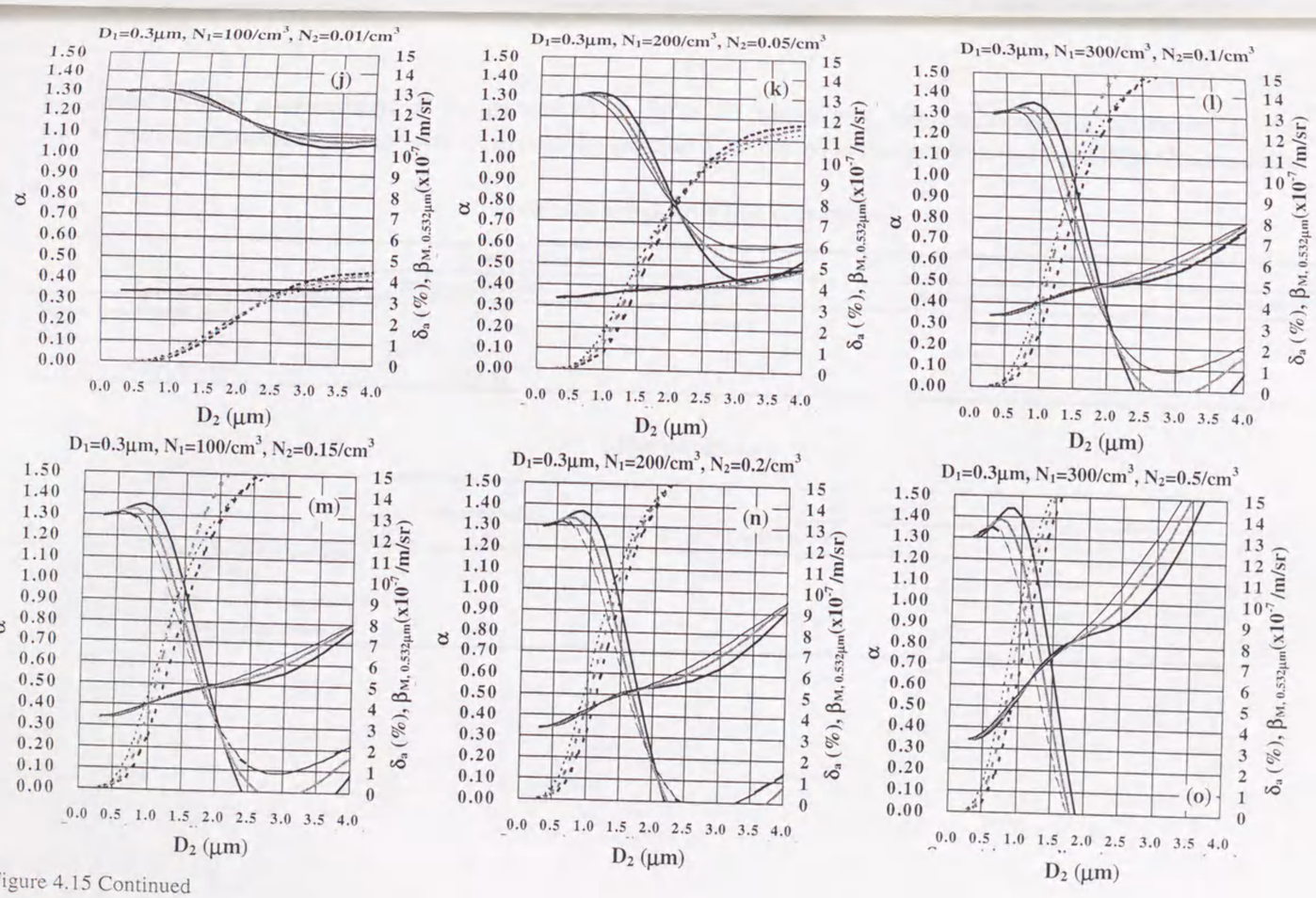

Figure 4.15 Continued

Table 4.5 The combinations of the parameters in Table 4.3 which give Mie backscattering coefficient β, the Ångström exponent α, and the aerosol depolarization ratio δ_a values within ranges obtained from lidar observations.

Assumed size distribution parameters

	Case I: Sulfate and natural aerosols		Case II: Sea salt	
	Accumulation mode	Coarse mode	Accumulation mode	Coarse mode
Number concentration (/cm^3)	200	0.05-0.5	300	0.10-0.15
Geometric mean diameter (μm)	0.3	1-2.5	0.2	1.1-1.3
Geometric standard deviation	1.45-1.55	1.4-1.6	1.45-1.5	1.5-1.6

Lidar parameters

	Observed values	Calculated values	
		Case I: Sulfate and natural aerosols	Case II: Sea salt
Mie backscattering coefficient β ($\times 10^{-7}$ /m/sr)	5.3	4.4-6.2	4.0-4.4
Aerosol depolarization ratio δ_a (%)	5.2	5.2-6.2	4.6-6.3
Ångström exponent values α	0.8-1.2	0.9-1.1	1.1-1.2

4.3.4 Discussion

Although the compositions of the particles are difficult to determine from our lidar observations and ten-day isentropic backward trajectories alone, we discuss some possible chemical compositions below.

As shown in Table 4.1, the five-winter average aerosol depolarization ratio of the arctic aerosols was about 5%. Although the average aerosol depolarization ratio was a little bit lower than 7% reported by Leaitch et al. (1989), the high aerosol depolarization ratios Leaitch et al. (1989) reported can be attributed to ice crystals. Since, however, the relative humidity (RH) of air masses where the arctic aerosol layers existed was less than 50% (five-winter average RH = 30%), the aerosols layers observed by our lidar were not composed of ice crystals.

Soil dust is claimed to be a possible chemical composition. The concentraion of soil dust in the Arctic reach peaks in spring and in autumn (Sirois and Barrie, 1999). The spring peak is associated with the long-range transport of Asian dusts raised by dust storms occurring in March, April, and May. Although we found trajectories from near the desert area as Bow and Shaw (1992) had suggested, these trajectories were only a very small fraction of all the trajectories. Therefore, soil dust is expected to be a minor possible chemical composition.

Xie et al. (1999) suggested that local area could be a source region of soil dust during storm conditions. If the dusts were transported from the local area, soil dust would be composed mainly of nonspherical coarse mode particles. We think that a large number of coarse mode particles may result in the lower Ångström exponent ($\alpha < 0.8$) and the higher aerosol depolarization ratio ($\delta_a \gg 5\%$). Soil dust is considered to be a minor possible chemical composition. Since, however, the Ångström exponent and the aerosol depolarization ratio of aerosol layer are determined by number of coarse mode particles, we cannot draw a conclusion from the calculated lidar parameters alone. To furthermore discuss their suggestion, we need to compare the results of lidar observations with the results of observations made using other techniques.

Sea salts are generally nonspherical particles with diameters of 0.02 μm to 60 μm (Fitzgerald, 1991). Most large sea-salt particles are removed from the atmosphere during long-range transport because of their short residence time (Gong et al., 1997a). Gong et al. (1997b) indicate that only sea-salts particles with diameters less than 1 μm could be transported long distances. Figures 4.13(b) and 4.13(c) indicate that air masses were transported from over or near the open water of the northern Pacific and Atlantic Ocean. Yamagata et al. (1999) observed a haze layer composed mainly of sea salts existing in the low relative humidity (RH < 20%) at an altitude of about 6 km asl

over Barrow, Alaska, during the Arctic Airborne Measurement Program 1998 (AAMP 98, National Institute of Polar Research) (Shiobara et al., 1999). The optical particle counter measurements made at that time suggested that the number of the accumulation and coarse mode particles increased at the altitude of about 6 km asl over Barrow, Alaska (Watanabe et al., personal communication, 1999). Their results suggest that sea salts is a possible chemical composition.

Trajectories shown in Figures 4.13(b) and 4.13(c) indicate that air masses were transported from over the open water in the Pacific Ocean as well as the Atlantic Ocean. Judging from the boundary of open water shown in Figure 2.1, we might think that air masses are also transported from over the Arctic Ocean or near the coast of the Arctic Ocean. A possible explanation is that a part of an oceanic air mass transported from the northern Pacific or Atlantic Oceans drifted over the Arctic Ocean. Another possible explanation is that sea salts from sea water passing through the cracks in the sea ice in the Arctic Ocean or sublimating from sea ice or snow containing sea salts was transported.

Okada et al. (1994) collected arctic aerosol particles with using an impactor at AStrO in the 1993 winter and investigated the constituent of the particles with an electron microscope equipped with an energy dispersive X-ray spectrometer. They reported that although Eureka is surrounded by frozen sea during the winter season there were many new and aged sea salts among the particles. With a scanning electron microscope, we also found particles seeming to be sea salts among the particles collected by a two-stage impactor (cut-off diameters 0.2 μm and 2.3 μm) at AStrO in February and March 1998. Figure 4.16 shows examples of SEM image of the particles seeming to be new and aged sea salts. Okada et al. (1994) suggested the cracks in the sea ice in the Arctic Ocean would be the source of sea salts and Osada et al. (1988) had earlier suggested the possibility of sea salt particles sublimating from sea ice or snow including sea salts. Our results suggest that the frozen Arctic Ocean was a possible source of sea salts and that sea salts sublimating from the ice crystals or the rime were present in the lower troposphere. Sea salts from near the coast of the Arctic Ocean or over the frozen Arctic Ocean would be transported at low altitudes in the stable winter arctic troposphere.

There are many industrialized and populated regions in northern and northwestern Russia, where power is produced by burning coal. This burning releases into the atmosphere many anthropogenic aerosols composed of nss-SO_4^{2-}, black carbon, non-soil dust and so on (Heidam, 1985; Pacyna, 1991; Cheng et al., 1993; Hopke et al., 1995; Polissar et al., 1999; Xie et al., 1999). Anthropogenic aerosols known as arctic haze

are transported from these regions to the arctic. Numerous ground-level measurements and airborne measurements have shown that the diameters of the particles in arctic haze have a bimodal distribution with peaks at 0.2-0.4 μm and 2-4 μm (Radke et al., 1984; Brock et al., 1990; Nagel et al., 1998). The arctic aerosols in the accumulation mode were reported to be composed mainly of nss-SO_4^{2-} (e.g., H_2SO_4 droplets, $(NH_4)_2SO_4$) (Sheridan, 1989; Brock et al., 1990; Parungo et al., 1990). Parungo et al. (1993) found that when an air mass was transported poleward from northern Russia the aerosols collected in the free troposphere were sulfate-covered particles of soil dust. Many of them were nonspherical submicron particles. Our result indicating that the arctic aerosols we observed were the accumulation mode particles is consistent with their results. Therefore, sulfate aerosol is also one of possible chemical compositions.

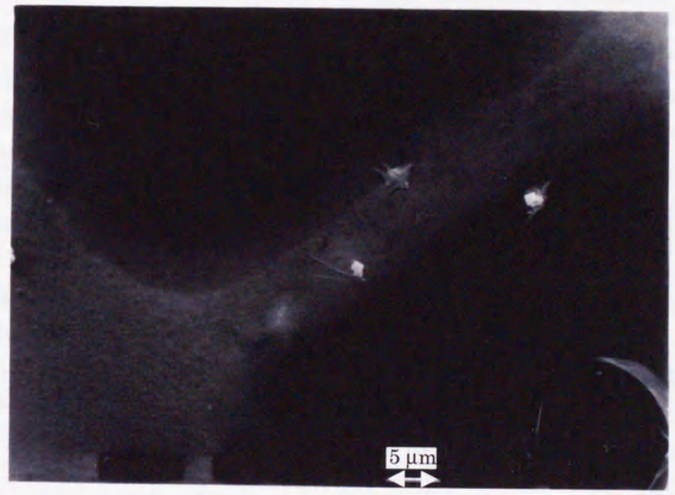

Figure 4.16 SEM image of arctic aerosols collected at AStrO.

4.4 Lidar observations and ground-level aerosol sampling in the late winter of 1998-99

4.4.1 Variation of chemical concentrations of arctic aerosols collected at Eureka

A lidar system is a useful tool for gathering information about the vertical distribution and optical properties of aerosols, but it is difficult to infer the detailed size, shape, and chemical compositions of aerosols from lidar observation. We investigated the source and size of the aerosols observed by our lidar in the previous section and discussed the some possible chemical compositions of the aerosols inferred from the source and size of the aerosols. Daily sampling of aerosol particles was carried out to investigate the chemical compositions of the aerosols at Eureka in the late winter of 1998-99. In this section, we compare the variations in the chemical composition of collected aerosol particles with the vertical profile of aerosol particles observed by lidar.

The chemical compositions of the aerosols were divided into three groups, the anthropogenic aerosol constituents (NH_4^+, H^+, and nss-SO_4^{2-}), sea salt constituents (Na^+, Cl^-, and Mg^{2+}, and soil dust constituents (Ca^{2+} and nss-Ca^{2+}). Ions of NH_4^+, H^+, and nss-SO_4^{2-} are derived form the anthropogenic activities. Ions of Na^+, Cl^-, and Mg^{2+} are derived mainly form sea salt (Seinfeld and Pandis, 1997). The variation of the concentration of Ca^{2+} or nss-Ca^{2+} is a measure of soil dust (Minoura et al., 1999: Mori et al., 1999). Figure 4.16 shows the variations of chemical constituent concentrations in the particles. High concentrations of NH_4^+, H^+ and nss-SO_4^{2-} were obtained on 19 February 1999. The concentrations of Na^+ and Cl^- were high in samples collected on 1, 2, 10, 11, 16, 17, 18, 19, and 27 February and on 1, and 9 March. High concentrations of Ca^{2+} or nss-Ca^{2+} were not obtained in the samples collected in the late winter of 1998-99.

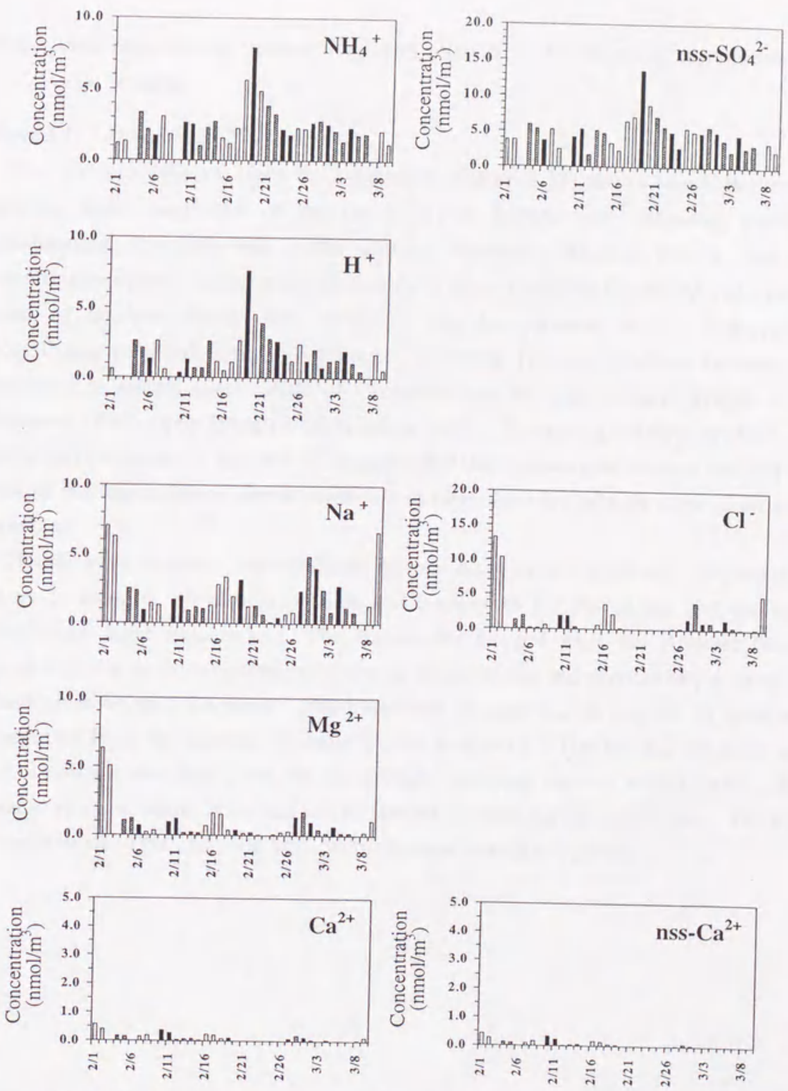

Figure 4.16 Variations of concentrations of aerosol constituents NH_4^+, H^+, Na^+, Mg^{2+}, and nss-SO_4^{2-}, Cl^- at AStrO collected at AStrO in the late winter of 1998-99. Ion of nss-SO_4^{2-} was calculated by subtracting sea salt SO_4^{2-} given by the SO_4^{2-}/Na^+ molar ratio (0.06) in the sea water × Na^+ concentrations for observed SO_4^{2-}. Ion of nss-Ca^{2+} was calculated by using the Ca^{2+}/Na^+ molar ratio (0.02) in the sea water for observed Ca^{2+} as the same as nss-SO_4^{2-}. White, black, and gray bars respectively indicate storm conditions, clear sky conditions, and no lidar observations.

4.4.2 Lidar observations, meteorology and relation to the chemical compositions of arctic aerosols

Period 1: 1 February to 2 February

The 700 hPa synoptic chart on 2 February (Figure 4.17) shows two high-pressure systems center southwest of the Great Britain Islands with extending over the Scandinavian Peninsula and center east of Severnaya Zemlya, Russia, and five low-pressure systems center north of, northwest of, and south of Greenland and over the coast of northern Russia and Alaska. The low-pressure system over Alaska intensifying persisted until 9 February. A strong pressure gradient between the low-pressure system center south of Greenland and the high-pressure system center southwest of the Great Britain Islands can be seen. The strong pressure gradient was formed on 29 January. Figure 4.17 suggests that the pressure gradient and the cyclonic flow of the low-pressure system northeast of Greenland brought an oceanic air mass poleward.

Clouds were observed intermittently by our lidar on 1-2 February. Figure 4.18 shows an example of vertical profiles and trajectories for the clouds and the track altitudes of those trajectories. The trajectories stopped over the Atlantic Ocean. Figure 4.19 shows the temporal variations of the scattering and depolarization ratios for clouds observed on 2 February. The trajectories suggest that an oceanic air mass was transported from the southern Atlantic Ocean to Eureka. The oceanic air mass was cooled down in the Arctic and the ice crystals including sea salt were formed. The oceanic air mass would bring sea salt to Eureka through stormy conditions. The high concentrations of Na^+, Cl^-, and Mg^{2+} were obtained during this period.

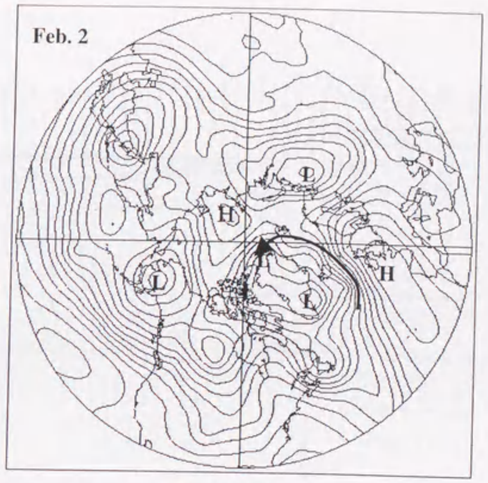

Figure 4.17 700 hPa synoptic maps for 0:00 UT on 2 February. H and L show the location of high- and low-pressure systems. An arrow shows the atmospheric flow.

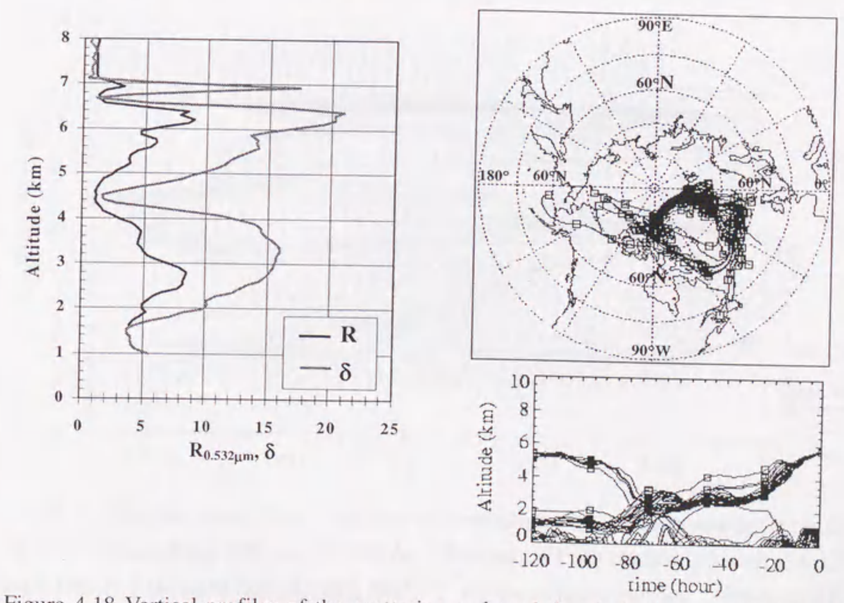

Figure 4.18 Vertical profiles of the scattering and total depolarization ratios of clouds observed by lidar on 2 February. Also shown are the ten-day back-trajectories calculated for those aerosol layers and the track altitudes of those trajectories. Open squares indicate 1-day intervals.

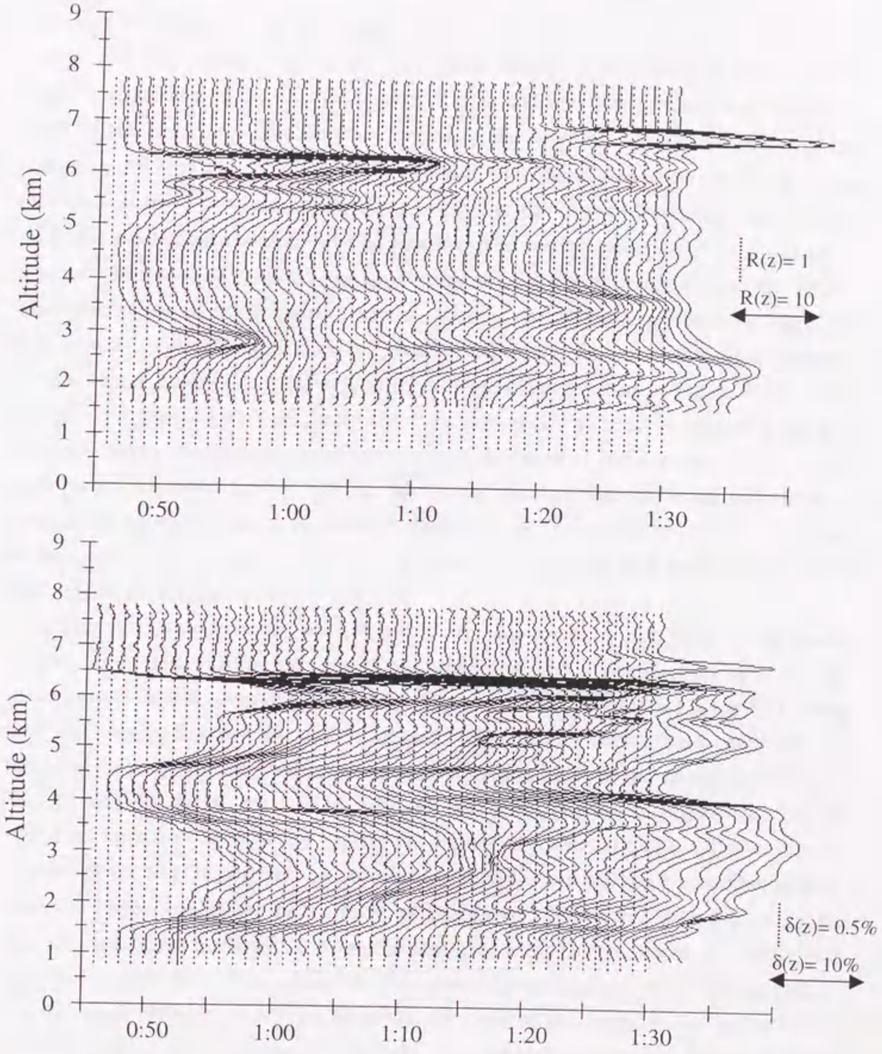

Figure 4.19 (upper panel) Time variation of vertical profiles of the scattering ratio of clouds observed from 0:50 to 1:30 UT on 2 February. Each dashed line (left side of each file) is a standard line showing 'R(z)=1' for the adjacent profile. (lower panel) Time variation of vertical profiles of the depolarization ratio of clouds observed from 0:50 to 1:30 UT on 2 February. Each dashed line (left side of each file) is a standard line showing 'δ(z)=0.5%' for the adjacent profile.

Period 2: 10 February to 11 February

The 700 hPa synoptic chart on 7 February (Figure 4.20) shows a high-pressure systems center east of Severnaya Zemlya, Russia and four low-pressure systems center north of the Scandinavian Peninsula, center of the coast of Alaska and center of the Canadian Archipelago. Figure 4.20 indicates that there were two poleward flows. One flow is from the northern Pacific Ocean over the Coast Mountains, Canada. The flow was created by a well-developed low-pressure system center south of the coast of Alaska. Figure 4.20 suggests that an oceanic air mass was transported to the Arctic. The other flow is from Eurasia to the Arctic. A pressure gradient between the high-pressure system center east of Severnaya Zemlya, Russia and the low-pressure system center southwest of Novaya Zemlya, Russia can be seen in Figure 4.20. This pressure gradient created the poleward flow during 5-9 February. Figure 4.20 also suggests that an air mass was transported form the coast of the northern Russia. The high-pressure system center east of Severnaya Zemlya, Russia, weakening moved toward the south and the low-pressure system center southwest of Novaya Zemlya, Russia moved toward the east on 10-11 February. The pressure gradient between the high- and low-pressure systems weakened.

During this period, stable aerosol layer were observed by our lidar in the lower troposphere. The vertical profiles of the scattering and depolarization ratios of the arctic aerosol layers observed by lidar on 11 February are shown in Figure 4.21 along with the trajectories and the track altitudes. Figure 4.22 shows an example of the temporal variations of the scattering and depolarization ratios of the arctic aerosol layer. We can see from the left panel of Figure 4.21 and the lower panel of Figure 4.22 that the total depolarization ratio of the layers was higher at lower altitudes. Those vertical profiles of the total depolarization ratio suggest that the aerosol layer was continuously from the upper atmosphere to the lower atmosphere. Although Figure 4.20 suggests that an oceanic air mass was transported from the northern Pacific to the Arctic, the trajectories show that an air mass was transported from the coast of the Arctic Ocean. As discussed in Section 4.3.3, we think that the coast of the Arctic Ocean or the frozen Arctic Ocean is a possible source of sea salt. An aerosol layer composed mainly of sea salt was transported from near the coast of the Arctic Ocean or over the frozen Arctic Ocean. As the result, the concentrations of Na^+, Cl^-, and Mg^{2+} would increase.

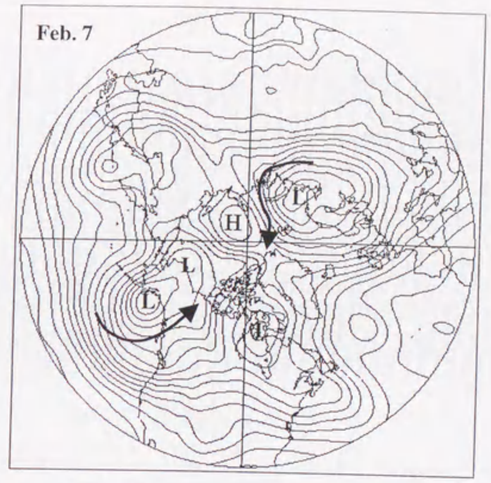

Figure 4.20 Same as Figure 4.17 but for 7 February.

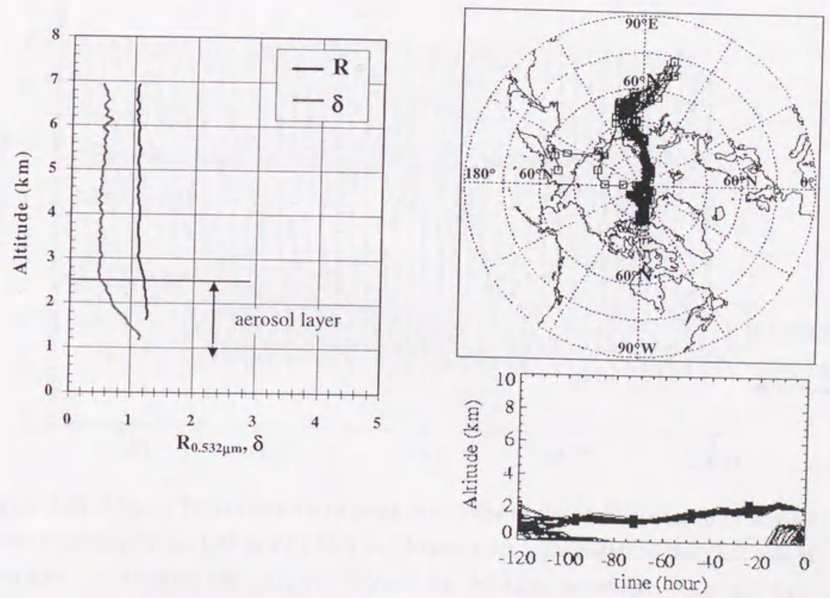

Figure 4.21 Same as Figure 4.18 but for the aerosol layer observed by lidar on 11 February.

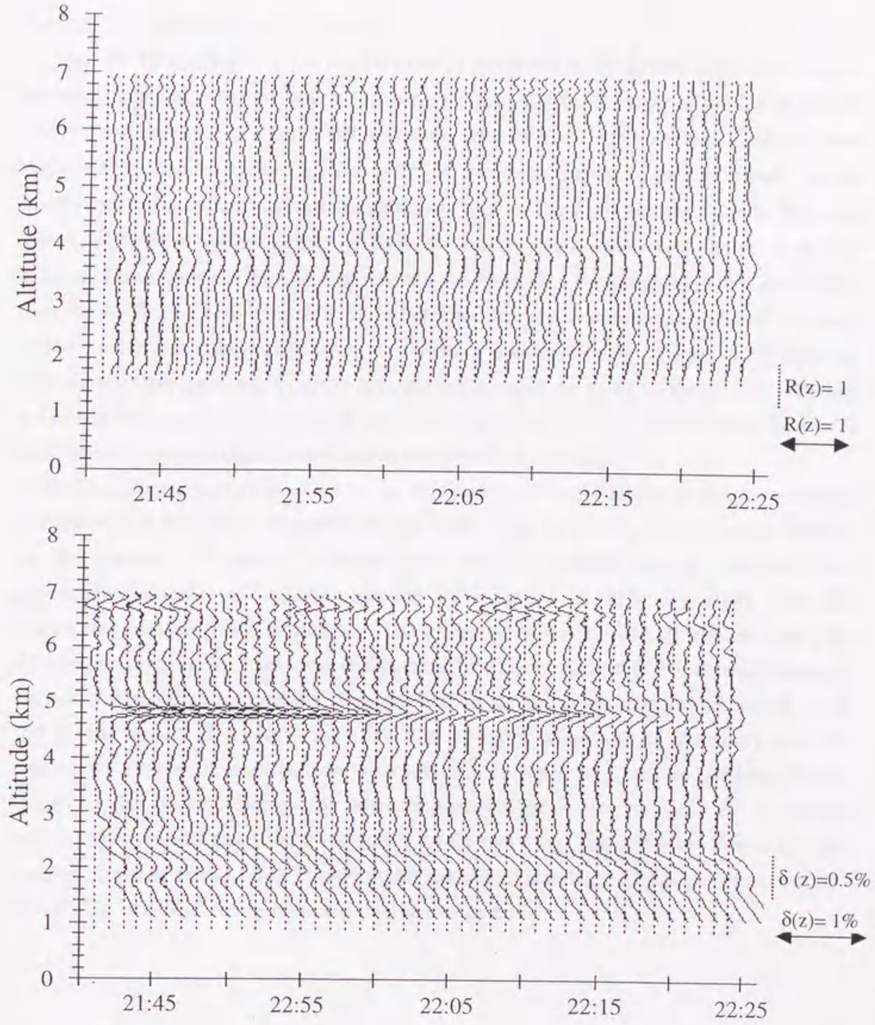

Figure 4.22 (Upper) Time variation of vertical profiles of the scattering ratio of aerosol layers observed from 21:45 to 22:25 UT on February 10. Each dashed line (left side of each file) is a standard line showing 'R(z)=1' for the adjacent profile. (Lower) Time variation of vertical profiles of the depolarization ratio of clouds observed from 21:45 to 22:25 UT on February 10. Each dashed line (left side of each file) is a standard line showing 'δ(z)=0.5%' for the adjacent profile.

Period 3: 16 February to 18 February

The 700 hPa synoptic chart on 16 February (Figure 4.23) shows two high-pressure systems center of over the Yukon territory, Canada and center west of the Great Britain Islands, and five low-pressure systems center west of Eureka , center south west of over the northern Pacific Ocean, center west of the coast of the western Canada, center northwest of the Scandinavian Peninsula, and east of the Spits Bergen Islands, Norway. The low-pressure system center of over the northern Pacific Ocean shown in Figure 4.23 appeared over the east of the Kamchatka Peninsula on 7 February and developed over the northern Pacific Ocean. Another low-pressure system center west of the coast of the western Canada appeared on 15 February and developed. Figure 4.23 suggests that the two low-pressure systems brought an oceanic air mass to the Arctic. Figure 4.23 also suggests that the oceanic air mass was transported by anticyclonic flow of a high-pressure system center over Northwest Territory, Canada.

Eureka experienced clear skies by 14 February. After 15 February clouds as shown in Figure 4.19 were often observed by our lidar. The fallen ice crystals were observed on the ground. Figure 4.24 shows the vertical profiles of the scattering and depolarization ratios of clouds observed by lidar on 17 February along with the trajectories and the track altitudes. The trajectories for the clouds shown in Figure 4.24 suggest that an air mass was transported from over Alaska or Northwest Territory, Canada. The fallen ice crystals suggests that an air mass was transported from a much and humid area. Therefore, the 700 hPa synoptic chart on 16 February and the trajectories suggest that an oceanic air mass was transported from the northern Pacific Ocean to the Arctic through the low-pressure activity. The oceanic air mass was cooled down in the Arctic and the ice crystals including sea salt were formed. The oceanic air mass would bring moisture and sea salt to Eureka. The high concentrations of Na^+, Cl^-, and Mg^{2+} were obtained during this period.

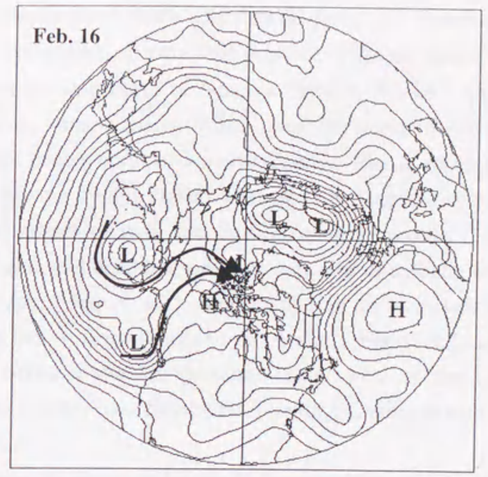

Figure 4.23 Same as Figure 4.17 but for 16 February.

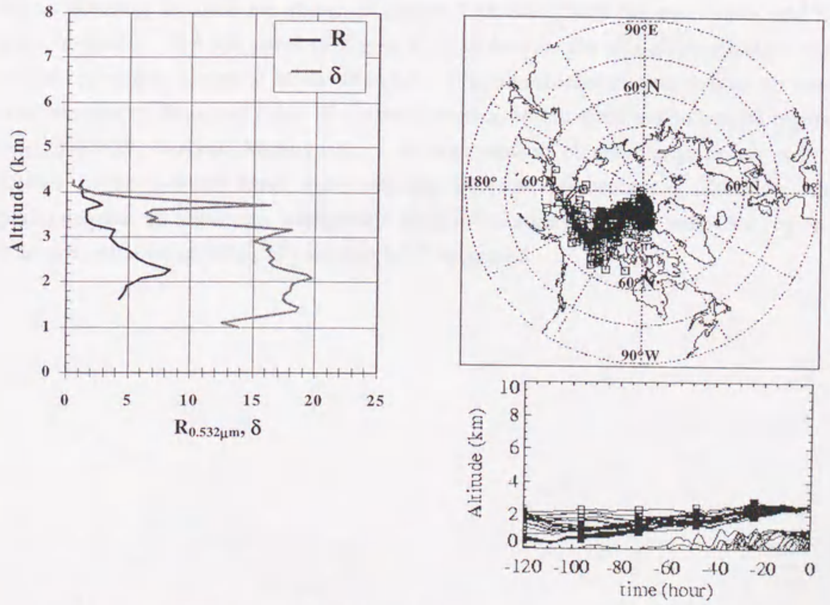

Figure 4.24 Same as Figure 4.18 but for clouds observed by lidar on 17 February.

Period 4: 19 February

The 700 hPa synoptic chart on 16 February (Figure 4.23) shows a deep low-pressure area where was composed of two low-pressure systems center northwest of the Scandinavian Peninsula and north of Novaya Zemlya, Russia. Figure 4.25 suggests that an air mass was transported eastward along the coast of northern Russia. The low-pressure system center north of Novaya Zemlya, Russia moved to near the North Pole. This low-pressure system linked with two low-pressure systems center west of the Greenland and center of over the Scandinavian Peninsula. The three pressure systems formed a wide and deep low-pressure area over the Arctic Ocean and persisted during 16-18 February. Figure 4.25 suggests that an air mass was transported by the cyclonic flow from the northern Russia to the Arctic. Figure 4.25 also suggests that a pressure gradient between the low-pressure center west of the Greenland and the high-pressure system center over Northwest Territory, Canada bough the air mass from the Arctic to Eureka.

Stable aerosol layer as shown in Figure 4.22 were observed by our lidar in the lower troposphere from about 23:00 UT on February 18 to about 8:30 UT on 19 February. The vertical profiles of the scattering and depolarization ratios of the arctic aerosol layers observed by lidar are shown in Figure 4.26 along with the trajectories and the track altitudes. The left panel of Figure 4.26 shows that the total depolarization ratio of the layers was higher at lower altitudes. The trajectories suggest that an air mass was transported from the coast of northern Russia, where there are industrial regions (e.g., Noril'sk, Vorkuta, Murumansk). A large amount of anthropogenic aerosols is known to be emitted from those regions into the atmosphere. Therefore, the anthropogenic air mass was transported from the northern Russian industrial regions. The concentration of NH_4^+, H^+, and nss-SO_4^{2-} increased.

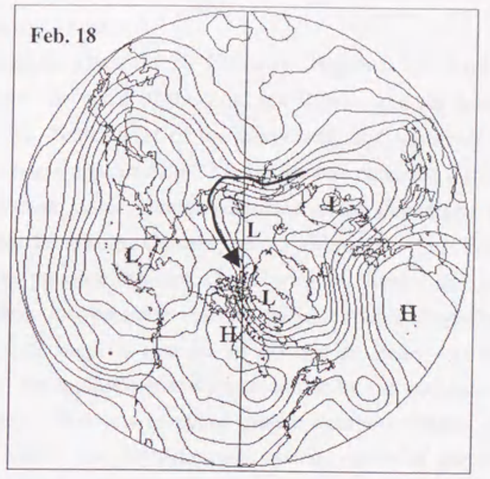

Figure 4.25 Same as Figure 4.17 but for 18 February.

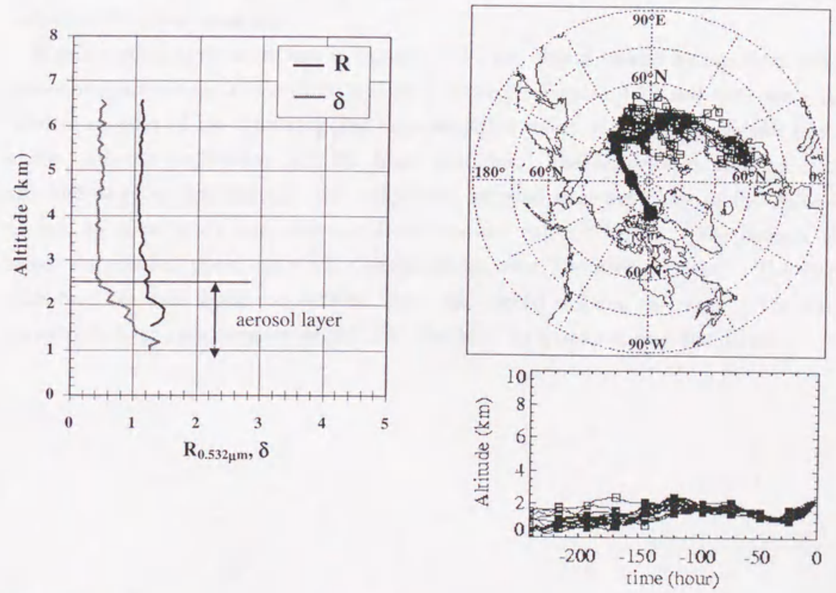

Figure 4.26 Same as Figure 4.18 but for the aerosol layer observed by lidar on 19 February.

Period 5: 27 February to 1 March

The 700 hPa synoptic chart on 28 February (Figure 4.27) shows a high-pressure system center of over the coast of the northern Russia, and six low-pressure systems center west of Eureka, center west of the Greenland, and southeast of the Greenland. The high-pressure system appeared on 27 February and persisted during 27 February - 3 March. A low-pressure system center southeast of the Greenland appeared over the east of the Labrador Peninsula, Canada, on 25 February. The low-pressure system linked with two low-pressure systems center west of Eureka and center west of the Greenland. The three low-pressure systems persisted with intensifying during 25-28 February. Figure 4.27 suggests that an air oceanic air mass was transported by the anticyclonic flow of the high-pressure system and/or by the cyclonic flow of the three low-pressure systems. The low-pressure system center southeast of the Greenland moved toward the east. The high-pressure system center of the eastern Greenland appeared on 1 March and the poleward flow weakened. The high-pressure system center of over the coast of the northern Russia moved toward the southeast. This poleward flow also weakened.

Stable aerosol layer as shown in Figure 4.22 were also observed by our lidar in the lower troposphere on 27 February and on 1 March. Figures 4.28 and 4.29 show the vertical profiles of the scattering and depolarization ratios of the arctic aerosol layers along with the trajectories and the track altitudes. The trajectories and the track altitudes suggest that although the trajectories stopped near the coast of the Atlantic Ocean, an oceanic air mass was supplied from the Atlantic Ocean. The oceanic air mass was cooled down onto the Greenland or over the Arctic Ocean. The haze including sea salt would be derived from the cooled oceanic air mass. The haze brought the high concentration of Na^+, Cl^-, and Mg^{2+} to Eureka during this period.

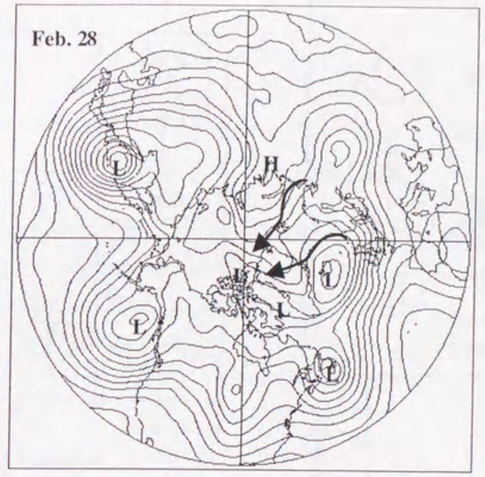

Figure. 4.27 Same as Figure 4.17 but for 27 February.

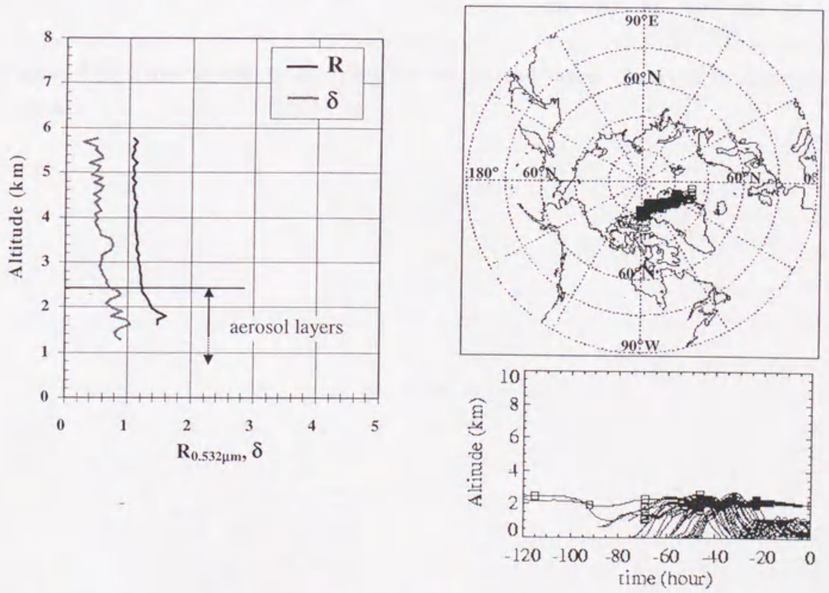

Figure 4.28 Same as Figure 4.18 but for the aerosol layers observed by lidar on 27 February.

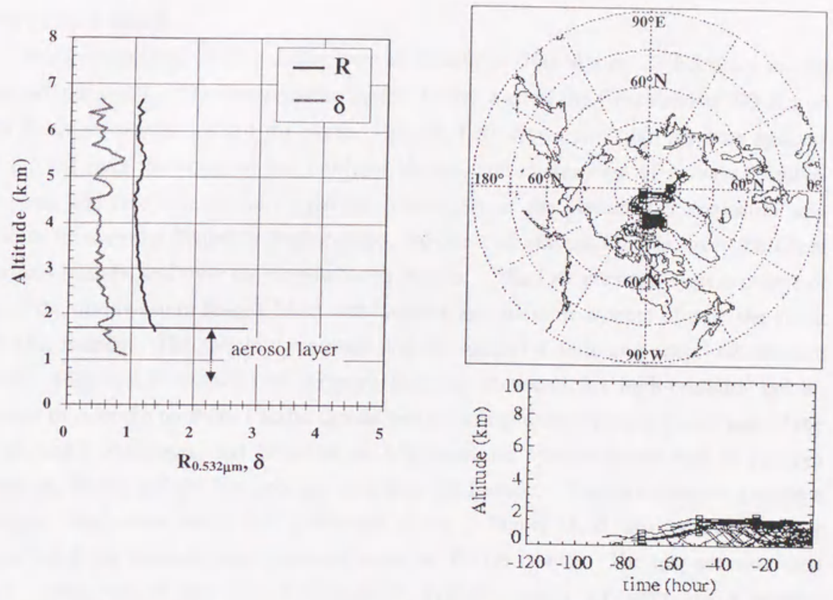

Figure 4.29 Same as Figure 4.18 but for the aerosol layers observed by lidar on 1 March.

Period 6: 4 March

The low-pressure system center west of Eureka at 700 hPa on 28 February moved toward the south. The low-pressure system center west of the Greenland at 700 hPa on 28 February moved toward the north. Figure 4.30 shows two high-pressure systems center of over the coast of the northern Russia, and center east of Novaya Zemlya, Russia, and five low-pressure systems center east of the Kamchatka Peninsula, and center of over the Canadian Archipelago, the coast of eastern Canada, over the Great Britain Islands, and over the northwestern Russia. The low-pressure system center of over the northwestern Russia liked with another low-pressure system of over the Great Britain Islands. The two low-pressure systems formed a wide and deep low-pressure area. Figure 4.30 shows two pressure gradients between the high-pressure system center of over the northern Pacific Ocean and the low-pressure system center east of the Kamchatka Peninsula, and between the high-pressure system center east of Novaya Zemlya, Russia and the low-pressure area over the Europe. The two pressure gradients suggest that there were two poleward flows. Figure 4.30 also shows another developed low-pressure area center of over the Baffin Island. The low-pressure area was composed of the two low-pressure systems center of over the Canadian Archipelago and the coast of eastern Canada. Another poleward flow was also formed by the two low-pressure systems.

Figure 4.31 shows the vertical profiles of the scattering and depolarization ratios of the arctic aerosol layers observed on 4 March along with the trajectories and the track altitudes. The total depolarization ratio of the layer was higher lower altitudes. The trajectories show that an air mass was transported from over the Arctic Ocean. Since the coast of and over the Arctic Ocean is a possible source of sea salt, one possible is that an air mass was transported from the Arctic Ocean. The other possible is the confliction of a dry and cold arctic air masse transported from the Arctic with the humid and warm oceanic air mass from the Atlantic Ocean. An oceanic air mass was transported from the Atlantic Ocean through the Davis Straits. The oceanic air mass supplied moisture and sea salt for the form of fog or haze. The dry and cold arctic air mass was transported by cyclonic flow of the developed low-pressure system center of over the Baffin Island. The oceanic air mass conflicted with the arctic air mass in the Arctic. The oceanic air mass was cooled down in the Arctic and formed the haze layer including sea salt. The haze layer would be transported to Eureka in the lower troposphere. The concentrations of Na^+, Cl^-, and Mg^{2+} increased on 4 March.

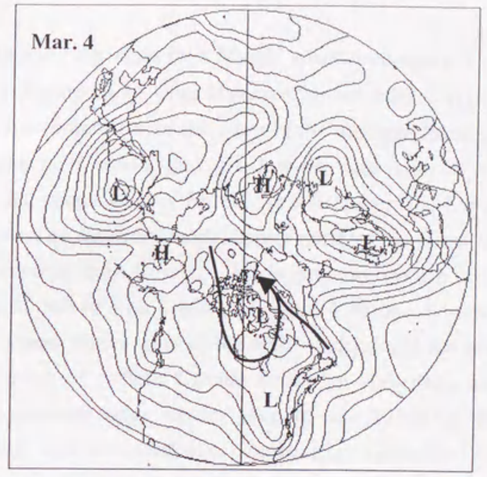

Figure 4.30 Same as Figure 4.17 but for 4 March.

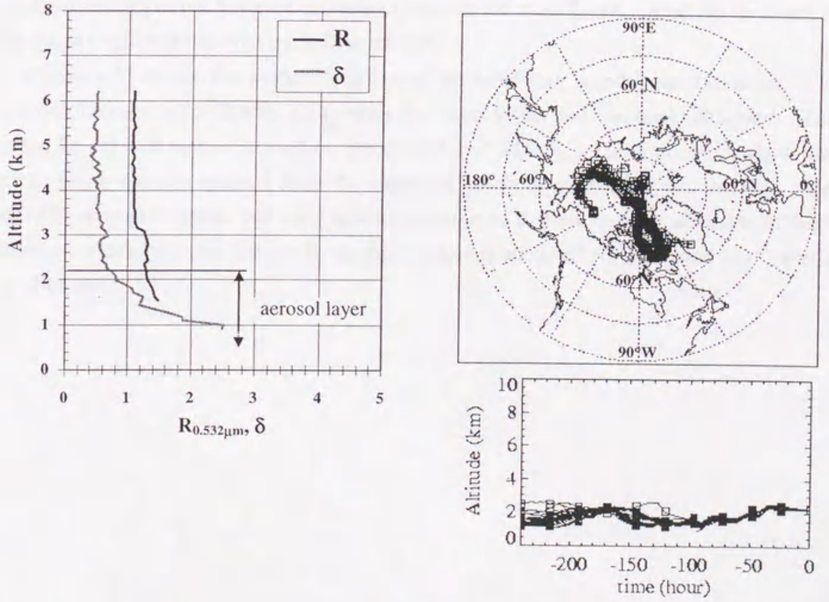

Figure 4.31 Same as Figure 4.18 but for the aerosol layers observed by lidar on 4 March.

Period 7: 9 March

Although Eureka had clear skies by 6 March, weather condition changed on 7 March. Clouds as shown in Figures 4.19 were observed by our lidar. Figure 4.32 shows two high-pressure systems center of over the coast of the northern Russia, and center east of the Labrador Peninsula, Canada, and six low-pressure systems center east of the Kamchatka Peninsula, center west of Eureka, center of over the Canadian Archipelago, center east of the coast of eastern Canada, center north of the Great Britain Islands, and center of over the northwestern Russia. A low-pressure system center of the coast of the eastern Canada at 700 hPa on 4 March (Figure 4.30) moved toward the northeast. The low-pressure system center west of the Baffin Island and the low-pressure system center east of the coast of eastern Canada formed a very deep trough over eastern Canada. A high-pressure ridge center east of the Labrador Peninsula, Canada appeared on 5 March and extended over southeastern Greenland during 5-8 March. Figure 4.32 indicates that a strong pressure gradient between the low-pressure systems and the high-pressure ridge was formed. Figure 4.32 suggests that this pressure gradient bought a much humid and warm oceanic air mass to the Arctic for the form of the ice crystals and the rime including sea salt.

Figure 4.33 shows the vertical profiles of the scattering and depolarization ratios of clouds observed on 9 March along with the trajectories and the track altitudes. The fallen ice crystals were observed on the ground on 9 March. The trajectories show that an air mass was transported from the eastern Canada through the Davis Straits. The 700 hPa synoptic charts and the trajectories suggest that an oceanic air mass through stormy conditions. As the result, the high concentrations of Na^+, Cl^-, and Mg^{2+}.would be obtained.

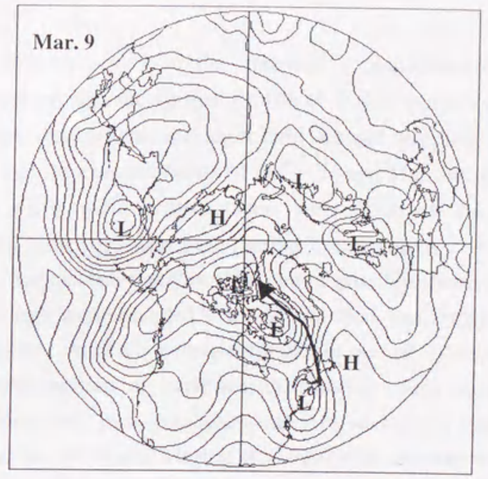

Figure 4.32 Same as Figure 4.17 but for 9 March.

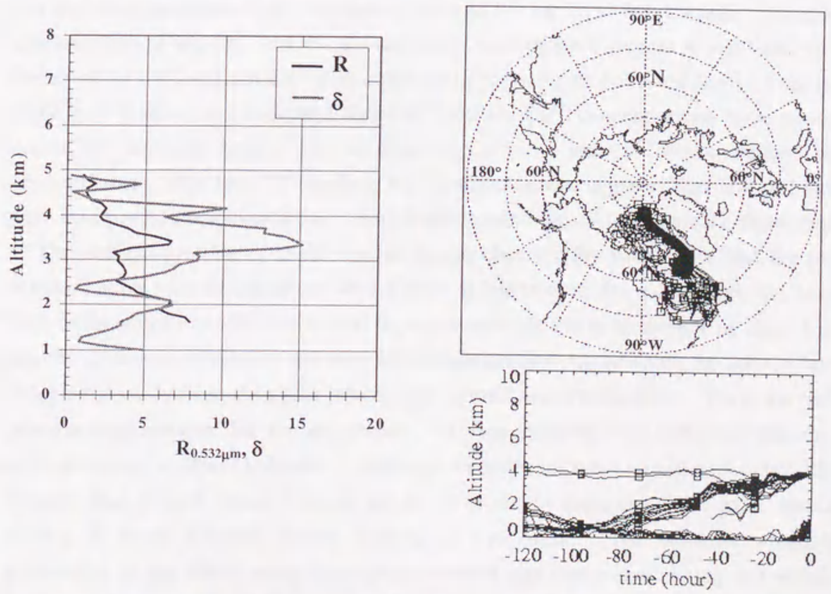

Figure 4.33 Same as Figure 4.18 but for clouds observed by lidar on 9 March.

4.4.3 Discussion

We compared the variations in the chemical composition of aerosol particles collected at observatory with the vertical profile of aerosol particles observed by lidar. The results of lidar observations and short-term aerosol sampling suggest that when clouds were observed the concentrations of Na^+, Cl^-, and Mg^{2+} were high (period 1, 3, and 7), and that when arctic aerosol layers were observed the concentrations of nss-SO_4^{2-} or Na^+, Cl^-, and Mg^{2+} were high (period 2, 4, 5, and 6).

In Section 4.3.2 we discussed soil dust as one of possible chemical compositions of the aerosol. Although we concluded that few soil dust was transported from the far desert areas, we did not draw a conclusion for Xie et al. (1999)'s suggestion that local areas could be source regions of arctic soil dust during storm conditions. Soil dust contains silicon, aluminum, iron, potassium, calcium, and so on (Seinfeld and Pandis, 1997). Minoura et al. (1999) and Mori et al. (1999) indicated that the concentration of Ca^{2+} or non-sea-salt Ca^{2+} (nss-Ca^{2+}) was high when soil dust as Kosa particles was transported. Barrie et al. (1989) reported that the concentration of Ca increased when soil dust was transported by a blizzard at Alert (82.5° N, 62.3° W), Canada. Thus, the concentration of nss-Ca^{2+} or Ca^{2+} is a useful measure of the transport of soil dust. The variations of Ca^{2+} and nss-Ca^{2+} concentration in the samples collected from 1 February 1999 to 9 March 1999 indicated that Ca^{2+} and nss-Ca^{2+} concentrations were near or below the detection limit. The increase of Ca^{2+} and nss-Ca^{2+} concentrations was unidentifiable. The low Ca^{2+} and nss-Ca^{2+} concentrations suggests that few soil dusts were transported from local areas. Soil dust is a minor possible chemical composition

The vertical profiles of arctic aerosol layers observed by lidar show that the total depolarization ratio of the layers was higher at lower altitudes. Although the lower limit of the vertical profile of the total depolarization ratio is at an altitude of about 1 km asl, those vertical profiles of the total depolarization ratio suggest that the aerosol layer was continuously from the upper atmosphere to the lower atmosphere. There are three possible explanations for the suggestion. A first possible explanation is the local vertical mixing at lower latitudes. Although an arctic air mass would experience little vertical and limited lateral mixing, an air mass might experience the local vertical mixing at lower latitudes before arriving in the Arctic. The aerosols would be transported in the stable arctic atmosphere without significant scavenging and vertical mixing. A second possibility is the sudden lowering of the top of the arctic inversion layer at AStrO that could lead to the higher concentration of aerosol at higher altitudes being mixed downward (Worthy et al., 1994). Although Figure 4.34 shows that the sudden lowering of the inversion layer did not occurred at AStrO, an air mass would

experience the sudden lowering of the inversion layer in the Arctic. Then, the air mass would be transported without significant scavenging and vertical mixing. A third possible explanation is the scavenging by the low-elevation fog. Bergin et al. (1989) reported that the base of the aerosol layer was coincident with the top of the inversion layer. Bergin et al. (1994) indicated that the frequent low-elevation fog could scavenge aerosols efficiently. Their result and suggestion indicate the possibility that the fog or haze can lead to the higher concentration of aerosol at higher altitudes being mixed downward. The aerosols would be transported from the base of the arctic aerosol layer to the lower atmosphere.

Figure 4.34 shows the altitude range of aerosol layers (black bars) and clouds (gray bars) observed by lidar and the variation of the top of the arctic inversion layer from 1 February to 9 March. The variation of the top of the arctic inversion layer shows that the aerosol layers observed during this period were either near or within the inversion layer. The above arguments and the results of lidar observations and short-term aerosol sampling during period 2, 4, 6, and 7 suggest the possibilities that the chemical composition of aerosols at AStrO (600m asl) was the same as that of aerosols observed by lidar. They suggest that the aerosol layer observed over Eureka were composed mainly of sulfate aerosols and sea salt. This suggestion supports the possible compositions of the arctic aerosols discussed in Section 4.3.2.

The 700 hPa synoptic charts and the trajectories of the clouds observed by lidar suggest that oceanic air masses were transported from over the northern Pacific or Atlantic Oceans. Latham and Smith (1990) suggest that sea salts with a diameter of roughly 1 - 2 μm could be effective to be the CCN. O'Dowd et al. (1997) reported that the sea salts play an important role in the CCN in an oceanic air mass and clouds would be formed. Their results suggest that clouds can bring moisture and sea salt. The results of lidar observations and short-term aerosol sampling during period 1, 3, and 5 support their suggestions. Our results and their suggestions suggests that the clouds play an important role not only in the transport of aerosols but also in the spatial source of aerosols.

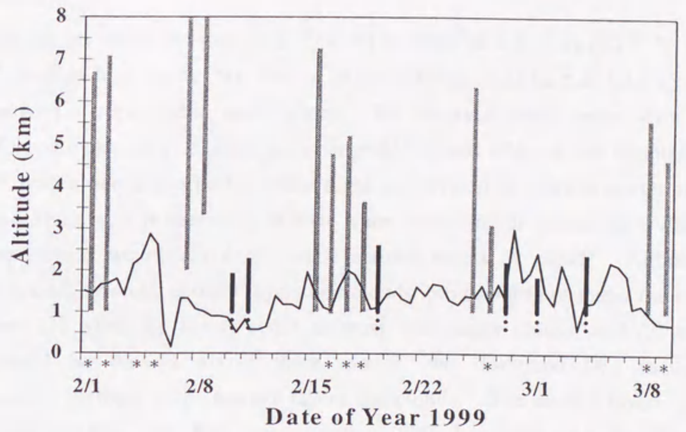

Figure 4.34 The altitude range of arctic aerosol layers (black bars) and clouds (gray bars) observed from 1 February 1999 to 9 March 1999 and the variation of the top of the temperature inversion layer (solid thin line). Dashed black bars show the range of the aerosol layers inferred from the vertical profiles of the total depolarization ratio. Asterisks (*) indicate falling-ice-crystal events.

5. Conclusions

During the six winter seasons from 1993-94 to 1998-99 at Eureka (80.0° N, 86.4° W) in the Canadian high arctic, we used a Mie-scattering polarization lidar system and made long-term tropospheric observations. We observed stable arctic aerosol layers lasting for more than several hours and changeable clouds within a few minutes. Since, however, lidar observations performed at night are difficult to confirm scattering objects with the naked eye, it is necessary to have some other way of determining whether the scattering objects we observed are arctic aerosol layers or clouds. Although it is difficult to classify arctic aerosol layers and clouds into two groups under the following conditions: (1) when the layers could co-exist with many clouds, and (2) when the layers could be present above thick clouds, we discussed two methods for discriminating between arctic aerosol layers and clouds. The aerosol layers existed in the atmosphere with less than approximately 60% humidity over ice (five-winter average: 43 ± 19%), while clouds existed in the atmosphere with greater than approximately 80% humidity over ice (five-winter average: 90 ± 15%). Then, the time dependency of the correlation coefficient between the different vertical profiles of the scattering objects was investigated. The correlation between different vertical profiles of the aerosol layers was close: the correlation coefficients ranged from 0.8 to 1.0. The correlation between different vertical profiles of the clouds was extremely changeable over time: the correlation coefficients ranged from 0.0 to1.0.

We investigated the vertical distribution of and optical information about the arctic aerosol layers discriminated by using two methods. The five-winter average backscattering coefficient and aerosol depolarization ratios of the aerosol layers observed by our lidar were 5.3×10^{-7} m^{-1} sr^{-1} and 5.2%. We calculated the optical depth τ_{AL} of the layer under the assumption that the Mie backscattering coefficient $\beta_{M,\,0.532\mu m}$ and the ratio of the extinction coefficient $\sigma_{M,\,0.532\mu m}$ to the Mie backscattering coefficient $\beta_{M,\,0.532\mu m}$ are constant in the arctic aerosol layer. The value of τ_{AL} is in the range of ~0.05-0.15. The value of the Ångström exponent of the aerosol layers calculated from two-wavelength lidar observations ranged from 0.8 to 1.2. The aerosol layers was observed at altitudes less than 3 km frequently and was observed occasionally at altitudes of 3 to 5 km, while clouds occurred uniformly across the range from low altitudes to high altitudes throughout the entire winter season.

We calculated the ten-day isentropic backward trajectories to investigate the long-range transport and source regions of arctic aerosol layers. The aerosol layers observed in the lower troposphere were transported from areas in Eurasia and near the coast of or over the Arctic Ocean with latitudes higher than 60°N. The aerosol layers

observed in the higher troposphere were transported from the Atlantic and Pacific Oceans or areas in Eurasia or northwestern Canada with latitudes lower than 60°N. To estimate the size of arctic aerosols we observed, we also calculated the lidar parameters (the backscattering coefficient, the aerosol depolarization ratio, and the Ångström exponent) by using the Mie theory, the calculated refractive indexes and the modeled particle size distribution. Those values calculated using the Mie theory and the modeled particle size distribution suggested that the geometric mean diameter of accumulation mode particles we observed was 0.2 to 0.3 μm. The calculated lidar parameters indicate that although the Mie backscattering coefficient of the aerosol layers depended mainly on the number concentration and the geometric mean diameter of the accumulation mode particles the aerosol depolarization ratio and Ångström exponent of the aerosol layers were markedly influenced by the number concentration and the geometric mean diameter of the coarse mode particles in the aerosol layers. We assumed that the possible chemical composition of the arctic aerosol layers assumed from the results of the isentropic backward trajectory calculations and the estimated size of the arctic aerosols was sulfate aerosol or sea salt.

We carried out daily sampling of aerosol particles to discuss the possible chemical compositions of the aerosols we inferred. We compared the variations in the chemical composition of aerosol particles collected at observatory with the vertical profile of aerosol particles observed by lidar. When many clouds were observed by lidar and fallen ice crystals and rime were also found on the ground, the concentrations of Na^+ and Cl^- increased. When the stable aerosol layer was observed by lidar, the concentrations of non-sea-salt SO_4^{2-}, NH_4^+, and H^+, or Na^+ and Cl^- increased. The results of lidar observations and short-term aerosol sampling suggested that the aerosol layers observed over Eureka were composed mainly of sulfate aerosol and sea salt. The suggestion indicated that the chemical compositions of the arctic aerosols assumed from the results of the isentropic backward trajectory calculations and the size of the estimated arctic aerosols is applicable.

Finally, in the arctic winter, many gaseous and particulate aerosols are transported poleward over several thousands km in the troposphere. The abundance of photochemically-reactive compounds and aerosols is loaded in the arctic atmosphere. The arctic plays an important role as a sink of many substances. The arctic would be an important region as the reactive field of aerosols. Aerosols serve as CCN and form clouds, fog, or haze with water vapor. They bring aerosols over several thousands km. Fallen snow and ice crystals, fog and haze bring them from the upper atmosphere to the lower atmosphere. Aerosols are released into the atmosphere by the evaporation and

sublimation of snow or ice crystal. Some of them are redistributed in the Arctic. Other might be transported from the Arctic to the lower latitudes. The arctic might play an important role not only as a sink and reactive filed of aerosol but also as a second source of substances (Figure 5.1). To further understand the atmospheric cycles of substances in the arctic, the couplings between the arctic region and the lower-latitude region, and the arctic ecosystem, we need to further explore the various natures and roles of the arctic aerosols.

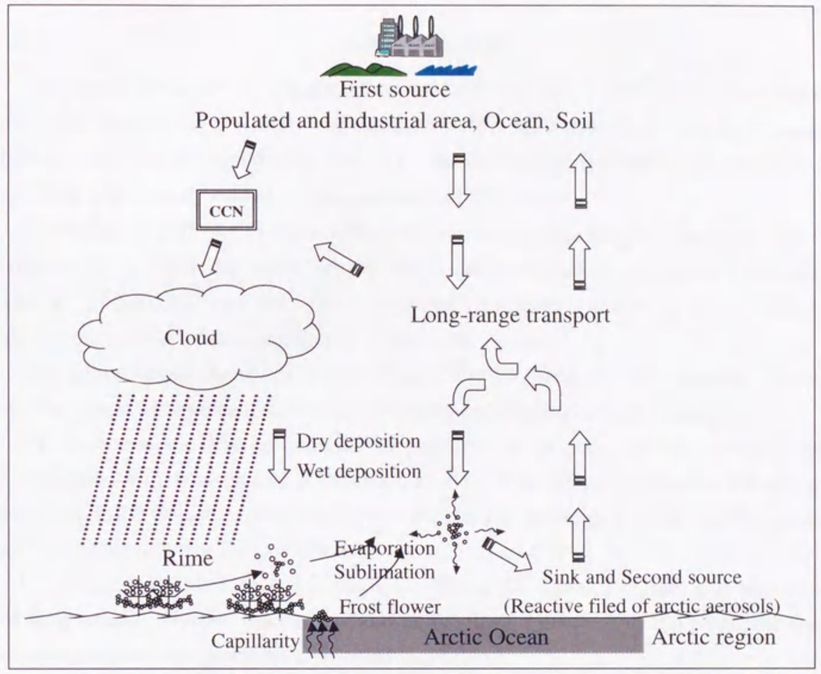

Figure 5.1 Conceptual illustration of the atmospheric cycles of substances in the Arctic

Acknowledgments

The author would like to acknowledge Associate Professor Shibata for providing me with the opportunity to study the arctic aerosols at Solar-Terrestrial Environment Laboratory, Nagoya University, and for his continuing guidance, encouragement, valuable discussions, and helpful suggestions for this work.

The author would like to acknowledge Professor Iwasaka for providing me with the opportunity to study the arctic aerosols at Solar-Terrestrial Environment Laboratory, Nagoya University and for his continuing guidance, encouragement, valuable discussions, and helpful suggestions for this work.

The author would like to express his gratitude to Dr. Itabe, Dr. Mizutani, Dr. Uchino, Mr. Nagai and Mr. Fujimoto for their continuing encouragement and assistance.

The author would like to express his gratitude to Dr. Fast and Dr. Wardle, AES Canada and for their assistance at Eureka, Canada. The author also wishes to thank the members of the Canadian Weather Station Eureka meteorological office for supporting our lidar observation at Eureka, Canada.

The author is deeply indebted to thank Dr. Osada, Dr. Sakai, Dr. Hara and Mrs. Kido for their helpful advices, discussions and help. It is a pleasure to the hospitality and encouragement of the members of Iwasaka Laboratory.

Finally, the author is pleased to express his appreciation to my father and mother, my brothers, and my wife for their help and understanding.

References

ABLE 3A, 1992. Special issue, Journal of Geophysical Research **97D**, 16383-16746.

AGASP-I, 1984. Special issue, Geophysical Research Letters **11**, 359-472.

AGASP-II, 1989. Special issue, Journal of Atmospheric Chemistry **9**, 1-383.

ARCTOC, 1997. Special issue, Tellus **49B**, 449-591.

DGASP, 1993. Special issue, Atmospheric Environment **27A**, 2695-3037.

IAOE-91, 1996. Special issue, Tellus **48B**, 135-328.

PSE 1992, 1994. Special issue, Journal of Geophysical Research **99D**, 25313-25517.

Adachi H., 1996. The external mixing state of polar stratospheric clouds observed by a lidar: Methodology for analysis (in Japanese), Master's thesis for Nagoya University.

Ångström A., 1964. The parameters of atmospheric turbidity, Tellus **16**, 64-75.

Barrie L. A. and Hoff R. M., 1985. Five years of air chemistry observations in the Canadian Arctic, Atmospheric Environment **19**, 1995-2010.

Barrie L. A., Den Hartog G. and Bottenheim J. W., 1989. Anthropogenic aerosols and gases in the lower troposphere at Alert Cnada in April 1986, Journal of Atmospheric Chemistry **9**, 101-127.

Barrie L. A. and Barrie M. L., 1990. Chemical components of lower tropospheric aerosols in the high Arctic: Six years of obsrvations, Journal of Atmospheric Chemistry **11**, 211-226.

Bergin M. H., Jaffrezo J. L., Davidson C. I., Caldow R. and Dibb J., 1994. Fluxes of chemical species to the Greenland ice sheet at Summit by fog and dry deposition, Geochimica et Cosmochimica Acta **58**, 3207-3215.

Bohren C. F. and Huffman D. R., 1983. Absorption and scattering of light by small particles, Wiley-Intersicence publication, New York.

Bowling S. A. and Shaw G. E., 1992. The thermodynamics of pollutant removal as an indicator of possible source areas for arctic haze, Atmospheric Environment **26A**, 2953-2961.

Bradley R. S., Keimig F. T., and Diaz H. F., 1992. Climatology of surface-based inversions in the North American Arctic, Journal of Geophysical Research **98D**, 8851-8858.

Bridgman H.A., Schnell R. Kahl J. D., Herbert G. A. and Joranger E., 1989. A major haze event near point Barrow, Alaska: analysis of probable source regions and tranport pathways, Atmospheric Environment **23**, 2537-2549.

Brock C. A., Radke L. F., and Hobbs P. V., 1990. Sulfur in particles arctic haze derived from airborne in situ and lidar measurements, Journal of Geophysical Research **95D**, 22369-22387.

Cheng M. -D., Hopke P. K., Barrie L. A., Rippe A., Olson M. and Landsberger S., 1993. Qualitative determination of source regions of aerosol in Canadian high arctic, Environment Science Technology **27**, 2063-2071.

Danielsen E. F., 1961. Trajectories isobaric, isentropic and actual, Journal of Mteorology **18**, 479-486.

Del Guasta M., Morandi M., Stefanutti L., Balestri S., Kyro E., Rummukainen M., Kivi R., Stein B., Wedekind C., Mielke B., Matthey R., Mitev V. and Douard M., 1998. Lidar observation of spherical particles in a -65° clod cirrus obseved above Sodankyla (Finland) during S.E.S.A.M.E., Journal of Aerosol Science **29**, 357-374.

Elterman L., 1951. The measurement of stratospheric density distribution with the searchlight technique, Journal of Geophysical Research **56**, 509-520.

Erickson D. J., Merrill T. T. and Duce R. A., 1986. Seasonal estimates of global atmospheric sea-salt distributions, Journal of Geophysical Research **91D**, 1067-1072.

Fernald F. G., 1984. Analysis of atmospheric lidar observations: some comments, Applied Optics **23,** 652-653.

Fitzgerald J. W., 1991. Marine aerosols: a review, Atmospheric Environment **25A**, 533-545.

Goff J. A. and Gratch S., 1946. Low-pressure properties of water from –160 to 212 F, Transactions of the American Society Heating and Ventilating Engineering **52**, 95-122.

Gong S. L., Barrie L. A., and Blanchet J. –P., 1997a. Modeling sea-salt aerosols in the atmosphere 1. Model development, Journal of Geophysical Research **102D**, 3805-3818.

Gong S. L., Barrie L. A., and Blanchet J. –P., 1997b. Modeling sea-salt aerosols in the atmosphere 2. Model development, Journal of Geophysical Research **102D**, 3820-3828.

Hara K., Osada K., Hayashi M., Matsunaga K., Shibata T. and Iwasaka Y., 1999. Fractionation of inorganic nitrates in winter arctic troposphere: Coarse aerosol particles containing inorganic nitrates, Journal of Geophysical Research **104D**, 23671-23679

Hoff R. M., 1987. Vertical structure of arctic haze observed by lidar, Journal of Applied Meteorology **27**, 125-139.

Holmgren B., Shaw G. E. and Weller G., 1974. Turbidity in the Arctic atmosphere, AIDJEX Bulletin **27**, 135-148.

Hopke P. K., Barrie L. A., Li S. -M., Chen M. -D., Li C. and Xie Y., 1995. Possible sources and preferred pathways for biogenic and non-sea-salt sulphur for the high arctic, Journal of Geophysical Research **100D**, 16595-16603.

Hopper J. F. and Hart W., 1994. Meteorological aspects of the 1992 Polar Sunrise Experiment, Journal of Geophysical Research **99D**, 25315-25328.

Horvath H., 1993. Atmospheric light absorption – a review, Atmospheric Environment **27A**, 292-317.

Iwasaka Y. and Hayashida S., 1981. The effects of the volcanic eruption of St. Helens on the polarization properties of stratospheric aerosols; lidar measurement at Nagoya, Journal of the Meteorological Society of Japan **59**, 611-614.

Iwasaka Y., 1986a. Large depolarization ratio of the winter Antarctic stratospheric aerosol layer: lidar measurement at Syowa station (69°00'S, 39°53'E), Antarctic, Journal of the Meteorological Society of Japan **64**, 303-309.

Iwasaka Y., 1986b. Measurement of depolarization of stratospheric particles by lidar – A case study on the disturbed stratospheric aerosol layer by volcanic eruption of Mt. El. Chichon, Journal of Geomagnetism and Geoelectricity **38**, 729-740.

Jäger H., Deshler T., and Hofman D. J., 1995. Midlatitude lidar backscatter conversions based on balloonborne aerosol measurements, Geophysical Research Letters **22**, 1729-1732.

Kahl J. D., 1993. A cautionary note on the use of air trajectories in interpreting atmospheric chemistry measurements, Atmospheric Environment **27A**, 3037-3038.

Khatttaov V. U., Tyabotov A. E., Alekseev A. P., Postnov A. A., and Stulov E. A., 1997. Aircraft lidar studies of the arctic haze and their meteorological interpretation, Atmospheric Research **44**, 99-111.

Klett J. D., 1981. Stable analytical inversion solution for processing lidar returns, Applied Optics **20**, 211-220.

Kley D., 1997. Tropospheric chemistry and transport, Science **276**, 7210-7254.

Kobayashi A., Hayashida S., Okada K., and Iwasaka Y., 1985. Measurements of the polarization properties of Kosa (Asian dust-storm) particles by a laser rader in spring 1983, Journal of the Meteorological Society of Japan **63**, 144-149.

Kobayashi A., Hayashida S., Iwasaka Y., Yamato M., and Ono A., 1987. Consideration of depolarization ratio measurements by lidar – in relation to chemical composition of aerosol particles, Journal of the Meteorological Society of Japan **65**, 303-307.

Latham J. and Smith M. H., 1990. Effect on global warming of wind-dependent aerosol generation at the ocean surface, Nature **347**, 372-373.

Leaitch W. R. and Hoff R. M., 1989. Airborne and lidar measurements of aerosol and cloud particles in the troposphere over Alert Canada in April 1986, Journal of Atmospheric Chemistry **9**, 187-211.

Logan J. A., Prather M. J., Wosfy S. C., and McElroy M. B., 1981. Tropospheric chemistry: a global perspective, Journal of Geophysical Research **86D**, 7210-7254.

Maiman T., 1962. Stimulated optical in fluorescent solids. I. theoretical considerations, Physical Review **123**, 1145-1150.

McClung F. J. and Hellwarth R. W., 1962. Giant optical pulsations from Ruby, Journal of Applied Physics **33**, 828-829.

Measures R. M., 1992. Laser remote sensing, 237-246, Krieger publishing company, Malabar.

Mitchell J. M. Jr., 1956 Visual range in the polar regions with particular reference to the Alaskan arctic, Journal of Atmospheric and Terrestrial Physics (Special. Supplement). **1**, 195-211

Mischenko M.I. and Sassen K., 1998. Depolarization of lidar returns by small ice crystals: an application to contrails, Geophysical Research Letters **25**, 309-312.

Minoura H., Mizawa S. and Iwasaka Y., 1998. Seasonal changes in the concentrations of major cations and anions in precipitations in urban Nagoya, Japan: Asian dust storms (Kosa) and typhoons, Journal of the Meteorological Society of Japan, **76**, 13-17.

Mori, I., Iwasaka Y., Matsunaga K., Hayashi M. and Nishikawa M., 1999: Chemical characteristics of free tropospheric aerosols over the Japan Sea coast: aircraft-borne measurements, Atmospheric Environment, **33**, 601-609.

Murayama T., Okamoto H., Kaneyasu N., Kamataki H. and Miura K., 1999.Application of lidar depolarization measurement in the atmospheric boundary layer: effects of dust and sea-salt particles, Journal of Geophysical Research **104D**, 31781-31792.

Nagai T., Uchino O., Itabe T., Shibata T., Mizutani K., and Fujimoto T., 1997. Polar stratospheric clouds observed at Eureka (80°N, 86°W) in the Canadian Arctic during the 1994/1995 winter, Geophysical Research Letters **24**, 2243-2246.

Nagel G., Herber A., Thomason L. W. and Leiterer U, 1998. Vertical distribution of the spectral aerosol optical depth in the Arctic from 1993 to 1996, Journal of Geophysical Research **103D**, 1857-1870.

O'Dowd C. D., Smith M. H., Consterdine I. E. and Lowe J. A., 1997. Marine aerosol, sea-salt, and the marine sulphur cycle: a short review, Atmospheric Environment **31**, 73-80.

Okada K., Nagai T., Fujimoto T., and Uchino O., 1994. Sea salt collected at Eureka in the Canadian high arctic (in Japanese), spring conference abstracts of Meteorological Society of Japan, 21.

Osada K., Nishio F., and Higuchi K., 1988. Sea salt in deposited snow on sea ice and snow drift (in Japanese), Antarctic Record **32**, 17-24.

Ott W. T., 1995. Environmental Statistics and Data Analysis, 280-283. Lewis Publishers, Boca Raton.

Pacnya J. M. and Ottar B., 1989. Origin of natural constituents in the arctic aerosol, Atmospheric Environment **23**, 809-815

Pal S. R. and Carswell A. I., 1973. Polarization properties of lidar backscattering from clouds, Applied Optics **12**, 1530-1535.

Parkinson C. L., 1991. International variability of the spatial distribution of sea ice in the north polar region, Journal of Geophysical Research **96C**, 4791-4801.

Parungo F. P., Nagamoto C. T., Sheridan P. J., and Schnell R. C., 1990. Aerosol characteristics of arctic haze during AGASP-II, Atmospheric Environment **24A**, 937-949.

Parungo F., Nagamoto C., Herbert G, Harris J., Schnell R, Sheridan P., and Zhang N., 1993. Individual particle analyses of arctic aerosol samples collected during AGASP-III, Atmospheric Environment **27A**, 2825-2837.

Polissar A. V., Hopke P. K., Paatero P., Kaufmann Y. J., Hall D. K., Bodhaine B. A., Dutton E. G. and Harris J. M., 1999. The aerosol at Barrow, Alaska: long-term trends and source locations, Atmospheric Environment **33**, 2441-2458.

Prospero J. M., Charlson R. J., Mohen V., Jaenicke R., Delany A. C., Moyers J., Zoller W., and Rahn K., 1983. The atmospheric aerosol system: an overview, Reviews of Geophysics and Space Physics **21**, 1607-1629.

Raatz W. E., 1991. Pollution of the Arctic Atmosphere, 13-42, Elsevier, London.

Radke L. F., Lyons J. H., Hegg D. A., Hobbs P. V. and Bailey I. H., 1984. Airborne observations of arctic aerosols, I: characteristics of arctic haze, Geophysical Research Letters **11**, 393-396.

Radke L. F., Brock C. A., Lyons J. H., and Hobbs P. V., 1989a. Aerosol and lidar measurements of hazes in mid-latitude and polar airmasses, Atmospheric Environment **23**, 2417-2430.

Rahn K. A., Boyrs R. and Shaw G. E., 1977. The Asian source of Arctic haze bands, Nature **268**, 713-715.

Rahn K. A. and McCaffy R. J., 1980. On the origin and transport of the winter Arctic aerosol, Annual New York Academic Science **338**, 486-503.

Rosen J. M. and Kjome N. K., 1997. Tropospheric aerosol backscatter at a midlatitude site in the northern and southern hemispheres, Journal of Geophysical Research **102D**, 21329-21339.

Russell P. B., Swissler T. J. and McCormick M. P., 1979. Methodology for error analysis and simulation of lidar aerosol measurements, Applied Optics **18**, 3783-3797.

Sassen K., Grund C. J., Spinhirne J. D., Hardesty M. M. and Alvarez J. M., 1990. The 27-28 October 1986 FIRE IFO cirrus case study: A five lidar overview of cloud structure and evolution, Monthly Weather Review **118**, 2288-2311.

Sassen K., 1991. The polarization lidar technique for cloud research: a review and current assessment, Bulletin of the American Meteorological Society **72**, 1848-1868.

Sassen K., 1997. Contrail-cirrus and their potential for regional climate change, Bulletin of the American Meteorological Society **78**, 1885-1903.

Sakai T., Shibata T., Kwon S. -A., Kim Y. -S., Tamura K., Iwasaka Y., 2000. Free tropospheric aerosol backscatter, depolarization ratio, and relative humidity measured with the Raman lidar at Nagoya in 1994-1997: contribution of aerosols from the Asian continent and the Pacific Ocean, Atmospheric Environment **34**, 431-442.

Seinfeld, J. H. and Pandis S. N., 1997. Atmospheric Chemistry and Physics, Wiley-Interscience Publication, 438-440.

Shaw G. E. and Wendler G., 1972. Atmospheric turbidity measurements at McCall Glacier in northeast Alaska, Conference Proceedings on Atmospheric Radiation, 227-235.

Sheridan P. J., 1989. Characterization of size segregated particles collected over Alaska and the Canadian high arctic, AGASP-II flight 204-206, Atmospheric Environment **23**, 2371-2386.

Sherreze M. C., Kahl J. D. and Schnell R. C., 1992. Low-level temperature inversions of the Eurasian arctic and comparisons with Soviet drifting station data, Journal of Climate **5**, 615-629.

Shibata T., Fujiwara M., and Hirono M., 1980. Observation of stratospheric aerosols by Nd:YAG with a new type of near-infrared-sensitive photomultiplier tube, Japanese Journal of Applied Physics **19**, 2205-2209.

Shibata T., Sakai T., Hayashi M., Ojio T., Kwon S. –A., and Iwasakao Y., 1996a. Raman lidar observations: Simultaneous measurements of water vapor, temperature and aerosol vertical profiles II, Journal of Geomagnetism and Geoelectricity **48**, 1169-1177, 1996.

Shibata T., Itabe T., Mizutani K., Uchino O., Nagai T. and Fujimoto T., 1996b Arctic tropospheric aerosols and clouds in the polar night season observed by a lidar at Eureka, Canada, Journal of Geomagnetism and Geoelectricity **48**, 1169-1177.

Shibata T., Iwasaka Y., Fujiwara M., Hayashi M., Nagatani M., Shiraishi K., Adachi H., Sakai T., Susumu K., and Nakura Y., 1997. Polar stratospheric clouds observed by lidar over Spitsbergen in the winter of 1994/1995: Liquid particles and vertical "sandwich" structure, Journal of Geophysical Research **102**, 10829-10840.

Shiobara M., Fujii Y., Morimoto S., Asuma Y., Yamagata S., Sugawara S., Inomata Y., Watanabe M. and Machida T., 1999. An overview and preliminary results from the arctic airborne measurement program 1998 campaign, Polar Meteorology and Glaciology **13**, 99-110.

Sirois A. and Barrie L. A., 1999. Arctic lower tropospheric aerosol trends and composition at Alert, Canada: 1980-1995, Journal of Geophysical Research **104D**, 11599-11618.

Tang I. N., 1996. Chemical and size effects of hygroscopic aerosols on light scattering coefficients, Journal of Geophysical Research **101D**, 19245-19250.

Welch H. E., Muir D. C. G., Billeck B. N., Lockhart W. L., Brunskill G. J., Kling H. J., Olson M. P. and Lemoine R. M., 1991. Brown snow: a long range transport event in the Canadian Arctic, Environment Science Technology **25**, 280-286

Wendling P., Wendling R., Renger W., Covert D. S., Heintzenberg J., and Moerl P., 1985. Calculated radiative effects of arctic haze during a pollution episode in spring in1983 based on ground-based and airborne measurements, Atmospheric Environment **19**, 2181-2193.

Worty D. E. J., Trivett N. B. A., Hopper J. F. and Bottenheim J. W., 1994. Analysis of long-range transport events at Alert, Northwest Territories, during the Polar Sunrise Experiment, Journal of Geophysical Research **99D**, 25329-25344.

Xie Y. -L., Hopke P. K., Paatero P., Barrie L. and Li S. -M., 1999. Locations and preferred pathways of possible sources of arctic aerosol, Atmospheric Environment **33**, 2229-2239.

Yamagata S., Shoji K., Murao N., Ohta S., Shiobara M. and Fujii Y., 1999. Haze phenomena observed during Arctic Airborne Measurement Program (AAMP) 98 (in Japanese), Polar Meteorology and Glaciology Symposium **22**, 27-28.

Young A. T., 1980. Revised depolarization correction for atmospheric extinction, Applied Optics **19**, 3427-3428.